UNIVERSITY OF CALIFORNIA

Los Angeles

Design, Modeling, and Control of an Electrostatic Suspension Platform for Thin Disks

A dissertation submitted in partial satisfaction

of the requirements for the degree

Doctor of Philosophy in Mechanical Engineering

by

Kenneth Ernest Pyle

2023

ABSTRACT OF THE DISSERTATION

Design, Modeling, and Control of an Electrostatic Suspension Platform for Thin Disks

by

Kenneth Ernest Pyle
Doctor of Philosophy in Mechanical Engineering
University of California, Los Angeles, 2023
Professor Robert T. M'Closkey, Chair

This dissertation describes the design, modeling, and testing of a system to electrostatically suspend and manipulate a silicon disk between two sets of stator electrodes. Dual variants of the system are investigated for two disk sizes to yield four total electrode-disk configurations that differ in transduction schemes and the number of disk degrees of freedom that must be actively regulated. Transformers couple the electrodes into pairs that measure disk-electrode differential capacitances and exert electrostatic forces on the disk. There is no physical contact with the disk when it is suspended. Both disks are six-degree-of-freedom systems, however, yaw motion is not measurable using either electrode arrangement and in-plane translations of the smaller disk are passively stabilized by the fringe electrical field. Contributions of the dissertation include the development of a modeling paradigm that is easily adapted to additional electrode-disk geometry, the design and fabrication of a new levitation platform that eliminates actuator-sensor feedthrough, the development of a novel parametric fitting technique for open-loop unstable systems from closed-loop data, and the synthesis of a family of robust multivariable controllers.

The first electrode arrangement uses common electrodes for both control and sensing, however, redundant use of the electrodes produces significant feedthrough from the control inputs to the electronic pick-offs. Feedback controllers are designed for the smaller

disk to maximize robustness to perturbations of the plant's normalized coprime factors and multivariable loop-shaping techniques are used to improve closed-loop performance. The disk is suspended and comparisons between the analytical model and empirical data are made. Estimates of the RMS uncertainties of the disk position reveal nanometer- and sub-microradian-level precision for the vertical and rotational degrees of freedom, respectively. A new levitation platform aimed to eradicate actuator-sensor feedthrough is designed and fabricated. The updated system utilizes similar transduction methodology, however, the electrodes used for sensing and actuation are segregated. Analytical models are generated and multivariable controllers robust to various forms of uncertainty are synthesized. This system is under development for non-contact testing of micro-scale devices.

The dissertation of Kenneth Ernest Pyle is approved.

Tetsuya Iwasaki

Jason L. Speyer

Tsu-Chin Tsao

Robert T. M'Closkey, Committee Chair

University of California, Los Angeles

2023

TABLE OF CONTENTS

LIST OF FIGURES

LIST OF TABLES

NOMENCLATURE

$\mathbb{R}$	set of real numbers
$\mathbb{N}$	set of natural numbers (0 excluded)
$\mathbb{Z}$	set of integers
Δ	set of complex perturbations
$[\cdot]^T$	transpose
$[\cdot]^*$	conjugate transpose
$\|\cdot\|_F$	Frobenius norm
$\|\cdot\|_\infty$	$\mathcal{H}_\infty$ norm
$\jmath$	imaginary unit, $\sqrt{-1}$
s	transfer function independent variable
$\overset{r}{=}$	equals the real part of
λ	eigenvalue
$\rho(\cdot)$	spectral radius
σ	singular value
μ_Δ	structured singular value

ACKNOWLEDGMENTS

I am immensely grateful for the countless people who have made this dissertation possible. First and foremost, I want to thank my parents. I would not be the man that I am today without your endless patience, love, and support. The traits that I embody are reflections of you and my achievements are effectively yours. To my brother, Kevin, you have always been my best friend and I look up to you in many ways. Your willingness to assist and encourage is second to none and you have positively impacted my life more than anyone else. Thank you to Grandpa, Grandma, GrandDad, and GrandMom for being such amazing role models. GrandDad, I am an engineer because of you. I am indebted to my closest friends for backing me throughout this process and providing an abundance of entertainment along the way: Kory Fox, Jacob Cope, Matthew Sauer, Nicholas Peterson, Alec Spencer, Broderick Prows, Christos Voutsaras, Daniel Cope, Jack Haley, John Joseph Onorato, Matthew Jensen, Daniel McElaney, Jonathan Acosta, Charlie Reiter, and John Beutter. To my research colleagues at UCLA –Dr. Michael Andonian, Dr. Stephen Schein, David Hill, and Alessandro Bullitta –you aided greatly in helping me achieve my research goals. Thank you to the staff in the MAE Department and Nanoelectronics Research Facility: Ben Tan, Miguel Lozano, Marla Cooper, Amanda Gordillo, Abel Lebon, Collin Llewellyn, Joe Zendejas, and Hoc Ngo. I would like to thank my doctoral committee: Drs. Tetsuya Iwasaki, Jason Speyer, and Tsu-Chin Tsao. Your guidance and teaching aided in the construction of this dissertation and in many ways influenced me to pursue graduate studies in control theory. I would also like to thank the many professors who challenged me along the way, especially Drs. Elisa Franco, James Steve Gibson, Dennis Kim, and Robert Kinsey. Finally, thank you to Dr. Robert M'Closkey. You were the best mentor I could have asked for, both as an engineer and as a person.

To all of you,

Thank you.

VITA

2023-Pres.	Project Engineer, ATA Engineering, Inc., San Diego, CA.
2018-2023	Graduate Student Researcher, Dynamic Systems and Control Design Lab, University of California, Los Angeles, CA.
2017-2023	Teaching Fellow, Mechanical and Aerospace Engineering Department, University of California, Los Angeles, CA.
2018	M.S., Mechanical Engineering, University of California, Los Angeles, CA.
2017	B.S., Mechanical Engineering, University of California, Los Angeles, CA.

PUBLICATIONS

Kenneth E. Pyle and Robert T. M'Closkey. "Contactless Suspension of a Silicon Disk." *2023 American Control Conference*, pp. 704–709, May 2023.

Kenneth E. Pyle, Yen-Hung Wu, and Robert T. M'Closkey. "A High-Precision Continuous Scan and Step Scan System for Compact Spectrometer Applications." *IEEE/ASME Transactions on Mechatronics*, pp. 1–10, Apr. 2023.

Kenneth E. Pyle and Robert T. M'Closkey. "Dual–stage nanopositioner augmented with feedforward control." *9th IFAC Symposium on Mechatronic Systems*, pp. 265–270, Sep. 2022.

Michael Andonian, Kenneth Pyle, and Robert M'Closkey. "Modeling and control of electrostatically levitated MEMS." *2021 IEEE Conference on Control Technology and Applications (CCTA)*, pp. 880–886, Sep. 2021.

CHAPTER 1

Introduction

This dissertation develops a modeling paradigm and investigates various robustly stabilizing controllers for the electrostatic suspension of a silicon disk between two sets of stator electrodes. Four electrode-disk configurations are examined –two separate disks will each be analyzed for two electrode arrangements. The first electrode arrangement utilizes a common set of electrodes for both differential capacitance sensing and electrostatic actuation, however, this configuration creates feedthrough from the control signals to the electrical measurements. Successful suspension of each disk requires that the feedthrough be effectively mitigated in the measurements. The second electrode arrangement splits the system into separate control and sense electrodes to eliminate actuator-to-pick-off feedthrough. The disks vary in size such that the smaller disk is stabilized laterally by electrostatic forces from the fringe electrical field; meanwhile, weak fringe field forces act on the larger disk requiring active regulation of in-plane translational motion. All four electrode-disk configurations are capable of measuring and controlling the vertical position, roll, and pitch degrees of freedom of the disks. Disk yaw is unobservable in all cases due to the uniformity of the disks and the lateral translational degrees of freedom are essentially unobservable for the smaller disk. Yaw moments cannot be applied with either electrode arrangement.

The levitation platform establishes a prototype "testbed" that will be scaled down to study the dynamics of micro-electromechanical systems (MEMS). Of particular interest are the characterization of low-loss resonators used in high-sensitivity vibratory gyroscopes [CWY14, SAA15, DSC17, WLG21]. Etched from silicon wafers and often doped, these devices are known for their high level of precision due to exceptional signal-to-noise ratios. When excited, they generate vibratory responses that appear as degenerate pairs

of resonant modes. The performance of the gyroscope is dependent on the time constants associated with specific modes, where longer time constants indicate superior performance. Resonator testing has traditionally required mounting the stem to a solid substrate –typically another silicon wafer via a gold adhesion layer –however, the coupling between a vibrating mode of the resonator and supporting substrate is a path for energy loss in the mode. It is challenging in micro-scale devices to measure the coupling, however, any motion of the suspended stem in response to the vibrating mode provides direct evidence of resonator-substrate coupling and can be used to guide modifications of the resonator to reduce its severity. The electrostatic "bearing" is proposed to meet this need.

Electrostatic suspension is established when a conductive object comes into contact with an electric field of sufficient magnitude. Such an electric field is typically generated using stator electrodes to provide the necessary charge required for counteracting the gravitational force. In the simplest case, an electrostatically levitated body can be modeled as a parallel plate capacitor –the electrode and body each constitute one plate. The electrostatic force that can be exerted on the body is capped by the dielectric strength, defined as the minimum electric field at which an insulator becomes electrically conductive. Electrical breakdown is typically characterized by the breakdown voltage, which, for any gaseous medium like air, is a function of the ambient pressure, gap distance, and dielectric [HN82]. The relationship between the electrostatic force, F, and plate gap, z,

$$F = \frac{1}{2z} C v^2 = \frac{\epsilon A}{2z^2} v^2, \tag{1.1}$$

limits the levitation gaps to the MEMS-scale. Magnetic fields provide an alternative mode of suspension, however, the necessity of large coils to produce the magnetic field and inability to suspend non-ferromagnetic materials motivate the selection of electrostatics for this dissertation.

Electrostatic bearings were originally developed for high-precision inertial instruments based on spinning spherical rotors which are suspended in an electrostatic field [Atk67, Atk75]. More recent research has produced micro-scale rotors [TTM02, HGL05]. Spherical rotors require stabilization of the three translational degrees of freedom –the rota-

tional degrees of freedom are sensed and regulated with a separate mechanism. The absence of physical support for the rotor eliminates most frictional torques, which improves the accuracy, sensitivity, and life of the sensor. For non-spherical geometry, electrostatic levitation of silicon and aluminum disks, thin rings, and square glass plates are reported in [JHK95, JYH98, WYT10, MEF03, JH98]. The applications cited in these references focus on the contactless manipulation of semiconductor wafers and disk drive media. Suspension requires stabilization of the out-of-plane translational, roll, and pitch degrees of freedom. These references employ transduction schemes that separate actuation and measurement functions. The in-plane translational degrees of freedom are passively stable due to the centering forces created by the fringe electrical field acting on the platform sidewalls, or in the case of the ring, actively stabilized by radial electrodes. Active stabilization of the disk's five degrees of freedom has been reported in [AM21], though wide bandwidth rejection of feedthrough coupling is required. Poor feedthrough rejection at high frequencies, as well as the implementation of an unstable feedback controller, are possible causes of unreliable suspension.

The first contribution of this dissertation is the development of a modeling framework that is applied to the system in [AM21]. A smaller disk is then fabricated to simplify suspension through passive stabilization of the lateral degrees of freedom. Due to uncertainty in the transformer-based transduction system, the uniformity and coplanarity of the disk-electrode gaps, fringe field and squeeze film damping forces, and incomplete cancellation of the feedthrough, an initial controller is synthesized for the smaller disk to robustly stabilize the disk with respect to perturbations of a coprime factorization of the analytical model. The initial controller successfully suspends the disk and enables the identification of a parametric plant model from closed-loop data. Analysis of the parametric model yields information on the input and output directions associated with the unstable plant modes and guides the selection of well-conditioned input and output transformations that decouple the vertical, pitch, and roll measurements. The noise spectra associated with these kinematic variables show they are measured with high precision. A new electrode arrangement is constructed and analytical models are generated for both disk sizes from the detailed modeling paradigm

outlined. Stable controllers are synthesized and closed-loop stability margins to coprime factor perturbations and multiplicative input and output uncertainty are predicted.

This dissertation is divided into two parts that correspond to the two different electrode arrangements. Empirical data is only presented in Part I since testing of the second electrode arrangement has not commenced. The dissertation is organized as follows: Chapter 2 describes the layout of the first electrode set and its transduction scheme and derives a detailed model for the larger disk; Chapter 3 reviews several challenges presented by the work in [AM21] that will be solved herein; Chapter 4 develops two multivariable controllers for the smaller disk and presents experimental results; Chapter 5 describes the revised electrode arrangement and makes comparisons to the previous electrodes; Chapter 6 computes a model of the smaller disk with the second generation electrodes and designs a stabilizing controller; Chapter 7 follows the blueprint of Chapter 6, but for the larger disk; Chapter 8 summarizes the contributions and presents opportunities for future work on the topic; the appendices provide additional modeling computations.

Part I

The Feedthrough Dilemma

CHAPTER 2

System Description and Modeling

This chapter provides a detailed description of the electrodes and transduction electronics for the first electrode arrangement, as well as the analytical modeling technique and assumptions made in generating the model. Only the larger disk is considered for now: the smaller disk is the focus of Chapter 4.

2.1 System Description

A 41 mm radius disk is etched from a double side polished, 400 μm thick silicon wafer. The disk is sputtered with conductive films of 5 nm titanium and 1 μm aluminum to create an equipotential surface. Pertinent parameters related to the disk geometry are highlighted in Table 2.1. Two identical sets of electrodes –a top set and a bottom set –are used to suspend the disk by exerting forces normal to the disk. The electrostatic forces are capable of applying a net vertical force and two independent in-plane moments on the disk, as well as lateral forces when the disk is not parallel to the electrodes. The electrodes, shown in Figure 2.1, are patterned on glass plates as two concentric annuli, where each annulus is partitioned into four identical sectors to produce eight electrodes per glass plate. The glass plates are oriented

Table 2.1: Larger Disk Parameters

Symbol	Description	Value
r_{d}	disk radius	41 mm
h_{d}	disk thickness	400 μm
m	disk mass	4.92×10^{-3} kg
J_{t}	transverse-axis moment of inertia	2.07×10^{-6} kg·m^2
J_{s}	spin-axis moment of inertia	4.14×10^{-6} kg·m^2

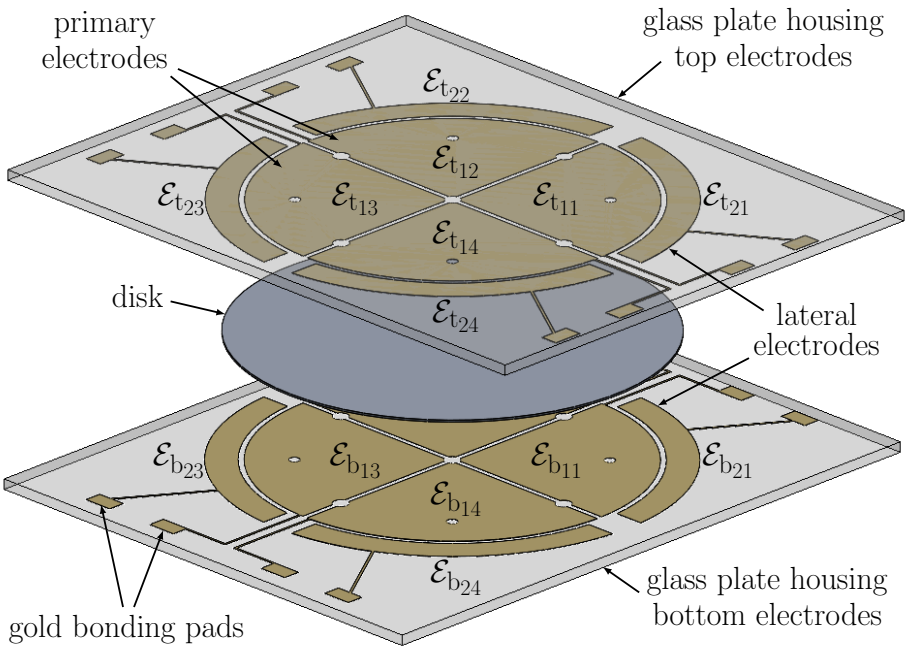

Figure 2.1: Exploded view of the initial electrode configuration.

normal to gravity and parallel to one another such that the top and bottom electrodes are mirror images of each other. The top and bottom electrodes –$\mathcal{E}_{t_{ij}}$ and $\mathcal{E}_{b_{ij}}$, respectively, where $\{i, j \in \mathbb{N} \mid i \leq 2,\ j \leq 4\}$ –are labeled according to "annular index", i, and electrode number, j. The inner ring of larger electrodes, corresponding to $i = 1$, are referred to as the *primary* electrodes and the outer ring of electrodes, that is, $i = 2$, are the *lateral* electrodes. The primary electrodes are grouped into four pairs of facing electrodes, i.e., electrodes $\mathcal{E}_{t_{11}}$ and $\mathcal{E}_{b_{11}}$ form a pair. These electrodes are used to exert electrostatic control forces on the disk and measure differential electrode-disk capacitances in order to regulate and sense the disk's vertical position, pitch, and roll. The lateral electrodes, meanwhile, are used strictly for sensing in-plane motion of the disk and are grouped in antipodal pairs where the top and bottom electrodes are shorted. The lateral degrees of freedom are coupled to angular rotations of the disk so that in-plane motion is stabilized by using the primary electrodes to tilt the disk. Disk yaw cannot be measured nor can yaw moments be applied to the disk.

The electrodes are patterned on the glass plates using a titanium adhesion layer followed by a conductive stack of silver and gold, where the gold cap prevents oxidation. The 100 ×

125 mm glass plates are 2 mm thick and the metal deposition thicknesses are 10 nm, 2 μm, and 200 nm for Ti, Au, and Ag, respectively. Each primary electrode has an area of 10.3 cm^2, meanwhile the lateral electrode areas are 3.44 cm^2. To avoid electrical breakdown, a 20μm layer of photoresist is baked onto each of the electrode sets, which also has the effect of increasing the disk-electrode capacitances due to the additional dielectric. The layer of photoresist is extended to a majority of the glass plates, leaving only the gold bonding pads on the exterior of the plates exposed. Precision shims are used to set the gaps between the disk and electrodes. Four sets of 229 μm shims and 400 μm silicon spacers etched from the same wafer as the disk are stacked on the bottom plate's photoresist, beyond the outer radii of the lateral electrodes, as shown in Figure 2.2. The top plate rests on the spacers to constrain the disk to a 229 μm range of vertical motion. When the disk is horizontally suspended such that its center of mass lies at the geometric center of the assembled system, 134 μm separate the disk surface vertically from each electrode set and the edge of the disk is perfectly centered between the inner and outer radii of the lateral electrodes. When viewed from above in this configuration, the disk overlaps 1.65 cm^2 of each lateral electrode. Additional parameters related to the electrode geometry are provided in Appendix A.

The transduction scheme for the primary electrodes will now be discussed. These electrodes are paired using the primary leads of center-tapped transformers that are supplied with fixed amplitude, 25 kHz sinusoidal currents. A separate transformer is used for each electrode pair and the transformer-electrode connection is displayed in Figure 2.3 for two adjacent electrode pairs. The center taps bisect the primary windings such that the primary winding inductances are identical on either side of the center tap and the carrier frequency is selected so that variations in the electrode-disk capacitances do not discernibly change

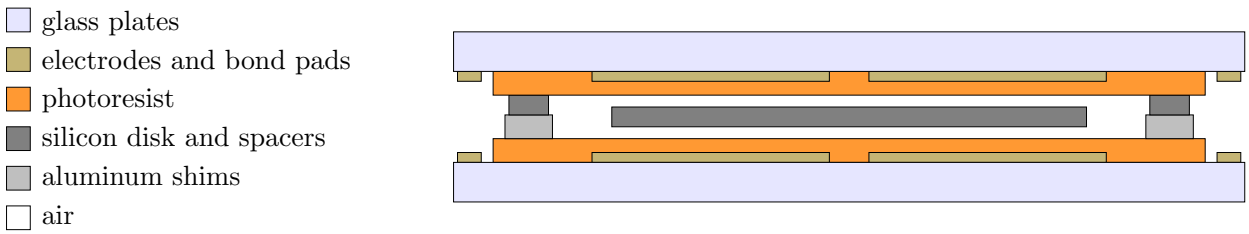

Figure 2.2: Electrode-disk gaps (not to scale).

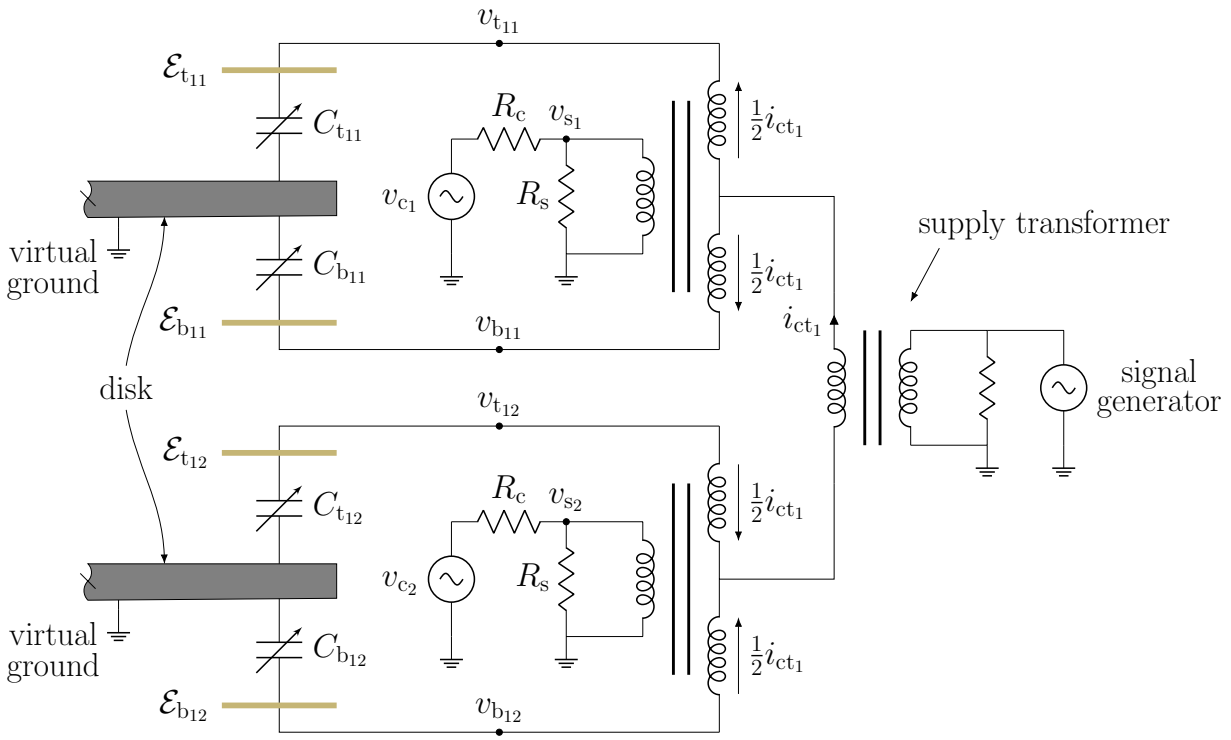

Figure 2.3: Schematic of the transformers that couple the top and bottom primary electrodes. The supply transformer that produces the center tap currents for two adjacent electrode pairs is shown to the right. The two remaining primary electrode pairs are configured identically.

the impedance looking into the center tap. This guarantees that the center tap current is, to first-order, evenly split between the top and bottom electrodes irrespective of the disk position. Within any electrode pair, the center tap produces AC electric potentials on the top and bottom electrodes that have the same phase.

In order to maintain the disk at ground potential, the current flow onto the disk by one electrode pair must be balanced by an equivalent current flow from the disk onto a different electrode pair. This is achieved using additional "supply" transformers to provide the center tap currents to two adjacent electrode pairs. By connecting one of the primary leads of a supply transformer to one center tap and the other primary lead to the companion center tap, the current entering the two center taps are equal in magnitude and opposite in sign. Since any positive charge deposited on the disk by one electrode pair is removed by the adjacent electrode pair, the disk remains at ground potential. The supply transformer for two adjacent electrode pairs is shown to the right in Figure 2.3, where the anti-phase

currents, i_{ct_1} and $-i_{\mathrm{ct}_1}$, supply the two center taps. The 25 kHz carrier is sourced by a signal generator. An additional supply transformer is required for grouping the $\{\mathcal{E}_{\mathrm{t}_{13}}, \mathcal{E}_{\mathrm{b}_{13}}\}$ and $\{\mathcal{E}_{\mathrm{t}_{14}}, \mathcal{E}_{\mathrm{b}_{14}}\}$ electrode pairs. The simplicity of preserving the disk at ground potential using transformer-supplied center taps motivates the use of an even number of primary electrode pairs to measure and control the disk's vertical position, tilt, and roll. Only three electrode pairs are required for regulating these degrees of freedom, however, maintaining the disk at ground potential by implementing center tap currents 120° out of phase with one another is difficult in practice. Thus, the proposed system utilizes four primary electrode pairs: two groups of electrode pairs with each pair coupled by a supply transformer.

Pairing the primary electrodes using transformers provides a convenient way of measuring the position of the disk via differential capacitances. Any mismatch in the gap between the disk surface and each electrode within a given pair creates a nonzero potential across the transformer primary winding. The resulting flux in the transformer core produces an AC voltage drop across the transformer secondary winding, v_{s_j}, whose amplitude is indicative of the capacitive imbalance and provides a measure of the disk's vertical position local to the primary electrode pair. Each "sense voltage", v_{s_j}, is demodulated with the 25 kHz carrier signal to yield a baseband signal proportional to the disk's position within the gap. A convenient null position of the disk is established since equivalent top and bottom electrode-disk gaps results in zero voltage drop across the transformer secondary winding. When the disk is suspended in this central position, the primary electrode-disk capacitances are estimated as 77 pF.

Each primary electrode pair is also used to exert electrostatic control forces on the disk by adding a control voltage, v_{c_j}, in series with the transformer secondary load via resistor R_{c}. The control signal is modulated to operate at the same 25 kHz frequency as the center tap and produces anti-phase sinusoidal potentials on the top and bottom electrodes. The net electric potential on each electrode is a superposed 25 kHz signal containing both the center tap and control components. Attractive electrostatic forces are exerted on the disk proportional to the square of the electrode potentials, however, the disk's inertia acts as a low-pass filter that

effectively attenuates the 50 kHz components such that the disk reacts to the mean-square value of the electrode voltages. Redundant use of the electrodes for both actuation and sensing intrinsically couples the control signals to the measurements, i.e., "feedthrough" from v_{c_j} to v_{s_j} obscures the disk measurements if left uncompensated. High fidelity identification and cancellation of this feedthrough coupling is required to suspend the disk.

The transduction scheme employed in the lateral channels is now discussed. The lateral electrodes are also paired using center-tapped transformers (see Figure 2.4), however, the primary leads are connected to antipodal electrodes. These transformers are identical to those used for the primary electrodes and the center taps are supplied with constant, albeit lower, amplitude 25 kHz currents that are generated using a supply transformer. Only one group of lateral electrodes –two electrode pairs coupled by a supply transformer –are necessary for measuring in-plane motion of the disk. Consider for now only the top electrodes and assume that the disk is constrained to lie horizontally, i.e., angular rotations are not possible. Any lateral translation of the disk in a single degree of freedom increases the capacitive area between the disk and one electrode and decreases the capacitive area between the disk and opposite electrode. The resulting capacitive imbalance generates a voltage drop across the transformer secondary load whose amplitude is indicative of the disk's lateral position. When angular rotations of the disk are considered, the voltage across the transformer secondary load is no longer strictly related to the electrode-disk overlap areas since the capacitances are also dependent on the gaps between the disk surface and the electrodes. For example, if an increase in electrode-disk overlap area is accompanied by an equal increase in distance between the disk and electrode, then no change in capacitance occurs. By shorting the top electrodes to the bottom electrodes to act as a single electrode, nonzero angles are accounted for since any increase in the gap between the disk and top electrode results in a decrease in the gap between the disk and bottom electrode by the same amount, and vice versa. The parallel capacitance between the disk-top electrode "capacitor" and the disk bottom-electrode "capacitor" remains constant as long as the overlap area is unchanged. Thus, when the top and bottom lateral electrodes are shorted together, the voltage drop across the transformer secondary load is dependent only on the lateral position of the disk. Convenient null posi-

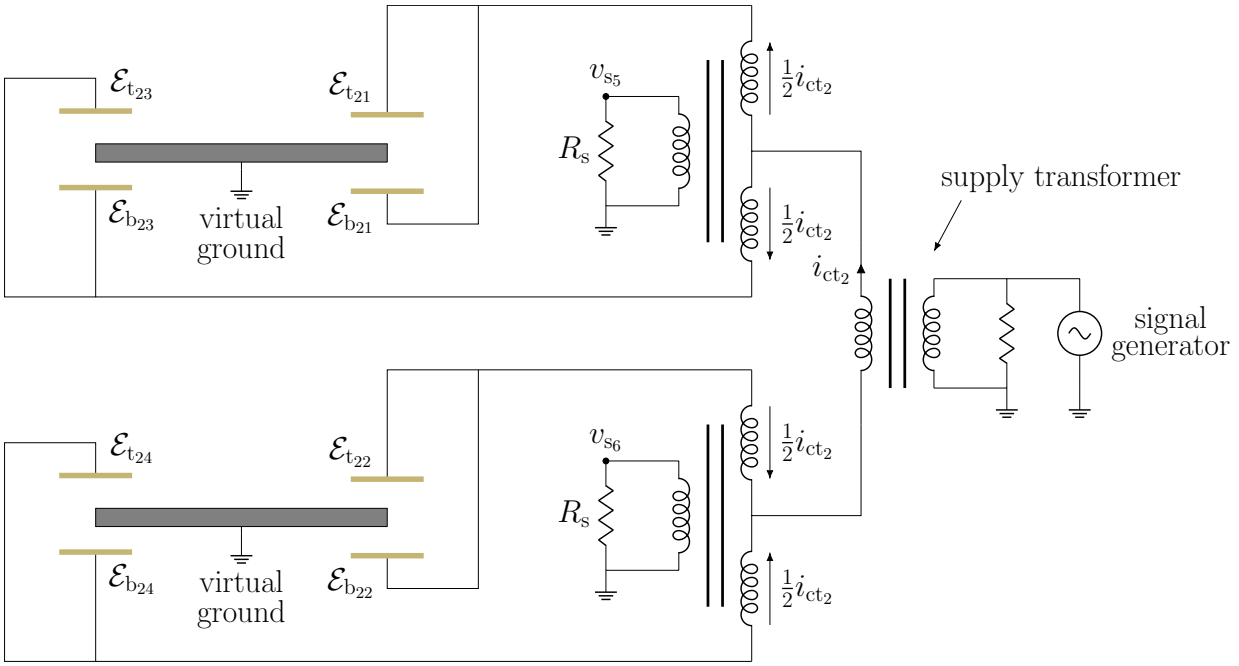

Figure 2.4: Schematic of the transformers that couple antipodal pairs of lateral electrodes to sense in-plane translational motion of the disk.

tions are also established for the lateral electrodes since zero amplitude voltage drops across the transformer secondary loads indicate that the disk is centered between the antipodal pairs. The sense voltages for the lateral channels, v_{s_5} and v_{s_6}, are also demodulated by the 25 kHz carrier signal.

A dSpace DS1104 digital signal processor (DSP) interfaces between the transformer electronics and digital filters discussed in detail in the following chapters. The DSP generates the system's inputs, u_j, and samples the electronic pick-offs to produce the discrete-time signals, g_k, $k = 1, ..., 6$, at a 5 kHz rate. Analog electronics are used to perform all modulation of the control signals and demodulation of the sense signals, as well as signal amplification. The control modulation phases, ψ_{c_j}, are selected to maximize the voltage differentials between the top and bottom electrodes, meanwhile the demodulation phases, ψ_{s_k}, are set to maximize the DC component of the demodulated sense signal with respect to changes in the electrode-disk gaps. Low-pass analog Butterworth filters are used to smooth the DSP outputs and avoid aliasing. A schematic of a single input/output channel of the analog subsystem of the plant is shown in Figure 2.5. The lateral electrodes are removed from the figure for

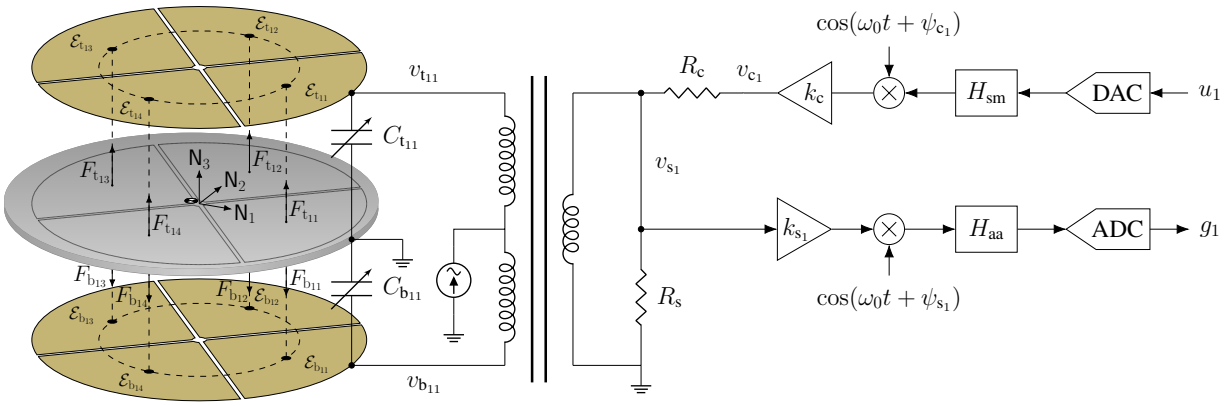

Figure 2.5: Diagram of the disk, primary electrodes, transformers, and analog conditioning (lateral electrodes are not shown). The disk is offset from the geometric center of the electrodes and the primary electrode footprints are traced on the disk top surface. The discrete-time signals u_1 and g_1 are specified and measured, respectively, by the DSP. This schematic depicts one input/output channel representative of the primary electrodes. The lateral channels exhibit similar output signal conditioning.

clarity and these electrodes exhibit similar analog-to-digital interfacing, however, no input signal is present in these channels. A digital feedforward filter, F, is used to compensate the feedthrough coupling in the primary channels and is considered internal to the plant. This filter operates in parallel to the subsystem, G, whose input is $u = [u_1\ u_2\ u_3\ u_4]^T$ and output is $g = [g_1\ g_2\ g_3\ g_4\ g_5\ g_6]^T$ (see Figure 2.10). The plant outputs, denoted ζ_k, are equal to the subtraction of the feedforward filter outputs from the sampled anti-aliased signals. No feedthrough is present in the lateral channels so ζ_5 and ζ_6 are equivalent to g_5 and g_6, respectively.

2.2 System Model

2.2.1 Disk Dynamics

Two coordinate frames are defined to describe the position of the disk relative to the electrodes. The inertial N-frame is designated with an origin, O_N, at the geometric center of the electrode sets. The N_1- and N_2-axes lie in a plane parallel to the glass plates with the

axes bisecting the electrode footprints[1] when viewed from above and the N_3-axis pierces the geometric center of each glass plate. The origin of the disk-fixed B-frame, O_B, is located at the disk's center of mass, with the B_1- and B_2-axes within the plane of the disk and the B_3-axis oriented normal to the disk. The disk dynamics are parameterized by the generalized coordinates $q = [x\ y\ z\ \theta\ \varphi]^T$, where $\{x, y, z\}$ characterize translations of the disk's center of mass relative to the N-frame and $\{\theta, \varphi\}$ describe an Euler-angle sequence about the N_1- and B_2-axes, respectively. Since the electrodes are incapable of both measuring yaw rotation and applying yaw moments to the disk, this degree of freedom is ignored. The relationship between the two coordinate frames is displayed in Figure 2.6, where the rotation matrix from the inertial frame to the body-fixed frame is given by

$$\mathcal{R}_{\mathsf{BN}} = \begin{bmatrix} \cos\varphi & \sin\theta\sin\varphi & -\cos\theta\sin\varphi \\ 0 & \cos\theta & \sin\theta \\ \sin\varphi & -\sin\theta\cos\varphi & \cos\theta\cos\varphi \end{bmatrix}. \tag{2.1}$$

The angular velocity of the B-frame, and hence disk, in the N-frame is represented by

$$\underline{\omega}_{\mathsf{BN}} = \dot{\theta}\underline{\mathsf{n}}_1 + \dot{\varphi}\underline{\mathsf{b}}_2. \tag{2.2}$$

Underbar notation will be used throughout this section to specify a directional vector in three-dimensional space. The $\{\underline{\mathsf{n}}_1, \underline{\mathsf{n}}_2, \underline{\mathsf{n}}_3\}$ vectors represent unit vectors along the $\{\mathsf{N}_1, \mathsf{N}_2, \mathsf{N}_3\}$-directions, respectively, and $\{\underline{\mathsf{b}}_1, \underline{\mathsf{b}}_2, \underline{\mathsf{b}}_3\}$ are unit vectors that point along the disk's principal axes, i.e., $\{\mathsf{B}_1, \mathsf{B}_2, \mathsf{B}_3\}$. An additional A-frame is defined as an intermediate frame in the Euler angle sequence shown in Figure 2.6, however, all vector computations in this section are performed in the N- and B-frames. When the disk is suspended centrally between the electrodes ($q = 0$), the N- and B-frames are coincident.

The disk's governing equations of motion are developed using Kane's method, a vector-based approach to computing the generalized forces acting on a system using partial velocities. These forces are classified into two categories –generalized active forces, $\mathcal{F}$, consisting of

[1]The electrode footprints are the projections of each electrode's perimeter onto the disk plane along the N_3-direction.

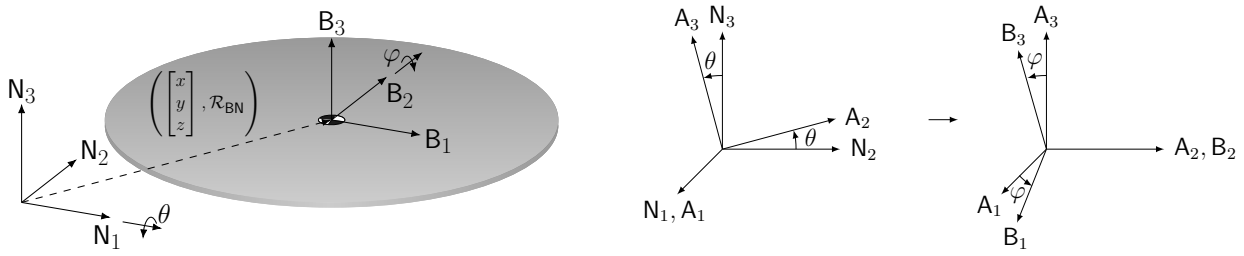

Figure 2.6: Left: Relationship of the inertial, N, and disk-fixed, B, coordinate frames. Right: 1-2 ($\theta - \varphi$) Euler angle sequence. An intermediate A frame is depicted, though all computations are performed in the N- and B-frames.

all contact and body forces acting on the disk, and generalized inertia forces, $\mathcal{F}^\star$, considered the "ma" side of Newton's second law of motion,

$$\mathcal{F} = \mathcal{F}^\star. \tag{2.3}$$

Both conservative and non-conservative forces are present in the system, however, constraint forces are not modeled. Calculating the generalized active forces requires knowledge of the resultant forces and moments acting on the disk, as well as the partial velocities of all points where forces are exerted and partial angular velocity of the disk. A free body diagram of all forces acting on the disk (gyroscopic terms are neglected) is shown in Figure 2.7. Included in the model are the gravitational force, viscous damping effects, and the electrostatic forces exerted by the electrodes. The disk and electrodes are assumed to act as parallel plate capacitors and the distributed electrostatic force exerted on the disk by each electrode is consolidated into a point force located where the disk center plane intersects an imaginary vertical line interpolating the projections of the electrode-disk overlap centroid onto each of the glass plates. This line is represented by $\{\mathsf{N}_1 = \bar{x}_{ij}, \mathsf{N}_2 = \bar{y}_{ij}\}$, where $(\bar{x}_{ij}, \bar{y}_{ij})$ characterizes the electrode-disk overlap centroid (viewed from above) for the $\{\mathcal{E}_{\mathrm{t}_{ij}}, \mathcal{E}_{\mathrm{t}_{ij}}\}$ electrode pair. All centroids are computed in Appendix A and are assumed to be dependent only on the lateral position of the disk. Since the disk is assumed to be an equipotential body, the electrostatic point forces are oriented normal to the disk. The vertical and two torsional squeeze film damping coefficients, c_z and $\{c_\theta, c_\varphi\}$, respectively, are estimated in Appendix C and the corresponding forces and moments are proportional to the vertical and angular rates. Disk shearing relative to the glass plates is modeled by Couette flow and the analogous viscous

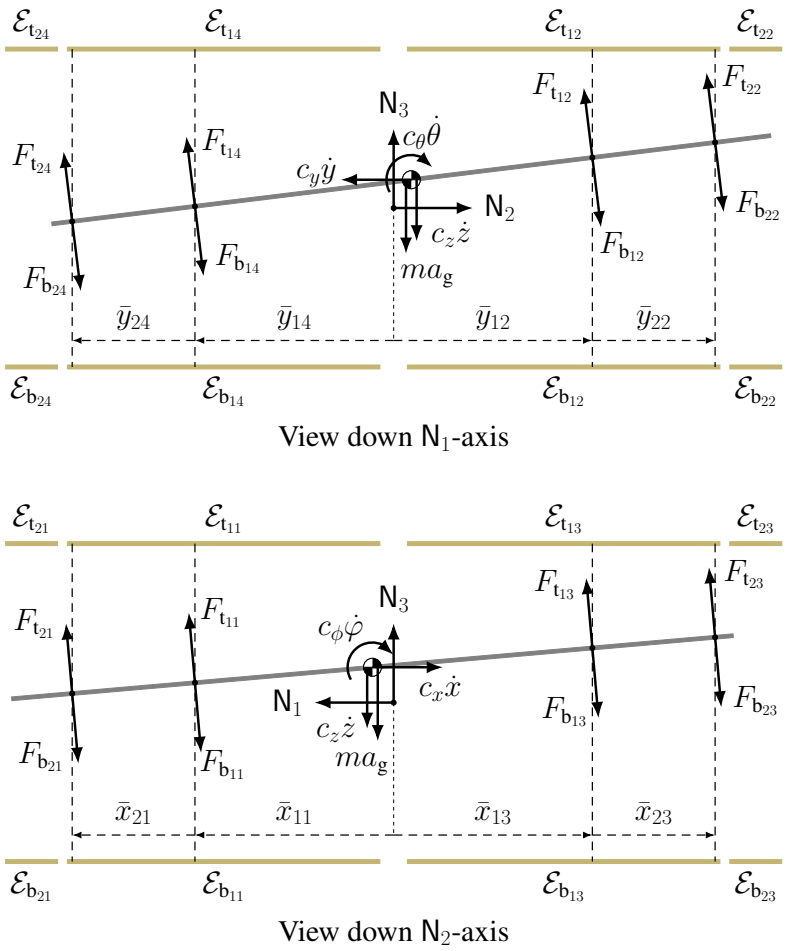

Figure 2.7: Free body diagram of the disk (not to scale). The electrostatic forces exerted by the electrodes are $\{F_{t_{ij}}, F_{b_{ij}}\}$, the viscous damping coefficients are $\{c_x, c_y, c_z, c_\theta, c_\varphi\}$, and gravitational acceleration is denoted a_g.

damping coefficients, $\{c_x, c_y\}$, are also predicted in Appendix C. All viscous damping effects are assumed to act on or about the disk's center of mass. Acceleration due to gravity is denoted a_g.

All forces and moments exerted on the disk are located at or about the disk's center of mass or where the disk center plane intersects the vertical centroid lines. The positions of these points in the N-frame are given by

$$\begin{aligned} \underline{r}_{\mathsf{O_B}} &= x\underline{\mathfrak{n}}_1 + y\underline{\mathfrak{n}}_2 + z\underline{\mathfrak{n}}_3 \\ \underline{r}_{\mathsf{P}_{ij}} &= \bar{x}_{ij}\underline{\mathfrak{n}}_1 + \bar{y}_{ij}\underline{\mathfrak{n}}_2 + z_{ij}\underline{\mathfrak{n}}_3, \end{aligned} \tag{2.4}$$

where $\underline{r}_{\mathsf{O_B}}$ is the position of the disk center of mass, $\underline{r}_{\mathsf{P}_{ij}}$ is the position of point P_{ij}, the

point where the disk center plane intersects with the vertical centroid line corresponding to electrode pair $\{\mathcal{E}_{\mathrm{t}_{ij}}, \mathcal{E}_{\mathrm{t}_{ij}}\}$, and z_{ij} represents the vertical deflection of the disk at point P_{ij}. The vertical deflections of the disk can be evaluated in terms of the generalized coordinates by rewriting the position vectors with regard to their translation relative to O_B. The conversion between reference points is given by

$$\underline{r}_{\mathsf{P}_{ij}} = \underline{r}_{\mathsf{O}_\mathsf{B}} + \underline{r}_{\mathsf{P}_{ij}/\mathsf{O}_\mathsf{B}}, \tag{2.5}$$

where $\underline{\mathsf{r}}_{\mathsf{P}_{ij}/\mathsf{O}_\mathsf{B}}$ is the position of P_{ij} relative to O_B:

$$\underline{r}_{\mathsf{P}_{ij}/\mathsf{O}_\mathsf{B}} = (\bar{x}_{ij} - x)\underline{\mathsf{n}}_1 + (\bar{y}_{ij} - y)\underline{\mathsf{n}}_2 + (z_{ij} - z)\underline{\mathsf{n}}_3. \tag{2.6}$$

Based on the coordinate frame definitions, $\underline{r}_{\mathsf{P}_{ij}/\mathsf{O}_\mathsf{B}} \cdot \underline{\mathsf{b}}_3 = 0$, yielding the vertical deflections

$$z_{ij} = z + (x - \bar{x}_{ij}) \sec\theta \tan\varphi + (\bar{y}_{ij} - y) \tan\theta. \tag{2.7}$$

The velocities of all points where forces are exerted on the disk are computed by vector differentiation of the position vectors in (2.4). All differentiation is performed in the N-frame, denoted by the N subscript in the velocity vectors, $\underline{v}_{\mathsf{PN}}$, where P is a placeholder for the point at which the velocity is computed. The velocity of the disk center of mass in the inertial frame is given by

$$\underline{v}_{\mathsf{O}_\mathsf{B}\mathsf{N}} = \dot{x}\underline{\mathsf{n}}_1 + \dot{y}\underline{\mathsf{n}}_2 + \dot{z}\underline{\mathsf{n}}_3 \tag{2.8}$$

and the velocity of point P_{ij} is represented by

$$\begin{aligned}
\underline{v}_{\mathsf{P}_{ij}\mathsf{N}} = {} & \dot{x}\left[\frac{\partial\bar{x}_{ij}}{\partial x}\underline{\mathsf{n}}_1 + \frac{\partial\bar{y}_{ij}}{\partial x}\underline{\mathsf{n}}_2 + \left(\left(1 - \frac{\partial\bar{x}_{ij}}{\partial x}\right)\sec\theta\tan\varphi + \frac{\partial\bar{y}_{ij}}{\partial x}\tan\theta\right)\underline{\mathsf{n}}_3\right] \\
& + \dot{y}\left[\frac{\partial\bar{x}_{ij}}{\partial y}\underline{\mathsf{n}}_1 + \frac{\partial\bar{y}_{ij}}{\partial y}\underline{\mathsf{n}}_2 + \left(-\frac{\partial\bar{x}_{ij}}{\partial y}\sec\theta\tan\varphi + \left(\frac{\partial\bar{y}_{ij}}{\partial y} - 1\right)\tan\theta\right)\underline{\mathsf{n}}_3\right] + \dot{z}\underline{\mathsf{n}}_3 \\
& + \dot{\theta}\left[(x - \bar{x}_{ij})\sec\theta\tan\theta\tan\varphi + (\bar{y}_{ij} - y)\sec^2\theta\right]\underline{\mathsf{n}}_3 + \dot{\varphi}\,(x - \bar{x}_{ij})\sec\theta\sec^2\varphi\underline{\mathsf{n}}_3,
\end{aligned} \tag{2.9}$$

where the expression for the vertical deflections in (2.7) is used.

Kane's method provides flexibility in selecting the generalized speeds, υ, which are chosen for mathematical convenience and/or physical relevance. In the general case, the generalized speeds are parameterized by

$$\upsilon = Y(q,t)\dot{q} + Z(q,t) \tag{2.10}$$

such that the motion of the system is entirely determined at any given time if the generalized coordinates and generalized speeds are known. For the disk system, the generalized speeds are defined as $\upsilon = \dot{q}$, where $Y = I$ and $Z = 0$ and the generalized speeds are identical to the generalized velocities of a traditional Lagrangian formulation. The velocities in (2.8) and (2.9) can be written in terms of the generalized speeds according to

$$\underline{v}_{\mathsf{PN}} = (\hat{\underline{v}}_{\mathsf{P}})^T \upsilon + \tilde{\underline{v}}_{\mathsf{P}}(q,t), \tag{2.11}$$

where $\hat{\underline{v}}_{\mathsf{P}}$ is called the partial velocity of point, P, in the N-frame and $\tilde{\underline{v}}_{\mathsf{P}}$ represents all terms independent of υ. The partial velocity vector for each point describes the directions associated with each of the generalized speeds. The partial velocities in the N-frame at each of the points where forces are exerted on the disk are evaluated as

$$\hat{\underline{v}}_{\mathsf{O_B}} = \begin{bmatrix} \underline{\mathsf{n}}_1 \\ \underline{\mathsf{n}}_2 \\ \underline{\mathsf{n}}_3 \\ 0 \\ 0 \end{bmatrix}, \quad \hat{\underline{v}}_{\mathsf{P}_{ij}} = \begin{bmatrix} \frac{\partial \bar{x}_{ij}}{\partial x}\underline{\mathsf{n}}_1 + \frac{\partial \bar{y}_{ij}}{\partial x}\underline{\mathsf{n}}_2 + \left(\left(1 - \frac{\partial \bar{x}_{ij}}{\partial x}\right)\sec\theta\tan\varphi + \frac{\partial \bar{y}_{ij}}{\partial x}\tan\theta\right)\underline{\mathsf{n}}_3 \\ \frac{\partial \bar{x}_{ij}}{\partial y}\underline{\mathsf{n}}_1 + \frac{\partial \bar{y}_{ij}}{\partial y}\underline{\mathsf{n}}_2 + \left(-\frac{\partial \bar{x}_{ij}}{\partial y}\sec\theta\tan\varphi + \left(\frac{\partial \bar{y}_{ij}}{\partial y} - 1\right)\tan\theta\right)\underline{\mathsf{n}}_3 \\ \underline{\mathsf{n}}_3 \\ \left((x - \bar{x}_{ij})\sec\theta\tan\theta\tan\varphi + (\bar{y}_{ij} - y)\sec^2\theta\right)\underline{\mathsf{n}}_3 \\ (x - \bar{x}_{ij})\sec\theta\sec^2\varphi\underline{\mathsf{n}}_3 \end{bmatrix} \tag{2.12}$$

and are stacked in the vectrix, $\hat{\underline{V}}$, according to

$$\hat{\underline{V}} = \begin{bmatrix} \hat{\underline{v}}_{\mathsf{O_B}} & \hat{\underline{v}}_{\mathsf{P}_{11}} & \hat{\underline{v}}_{\mathsf{P}_{12}} & \cdots & \hat{\underline{v}}_{\mathsf{P}_{24}} \end{bmatrix}. \tag{2.13}$$

The angular velocity of the disk in the N-frame can be similarly expressed as

$$\underline{\omega}_{\mathsf{BN}} = (\hat{\underline{\omega}}_{\mathsf{B}})^T \upsilon + \tilde{\underline{\omega}}_{\mathsf{B}}(q,t), \tag{2.14}$$

where $\hat{\underline{\omega}}_{\mathsf{B}} = [0\ 0\ 0\ \underline{\mathsf{n}}_1\ \underline{\mathsf{b}}_2]^T$ is the partial angular velocity of the disk.

The unconstrained generalized active forces are computed according to

$$\mathcal{F} = \hat{\underline{V}} \cdot \underline{R} + \hat{\underline{\omega}}_B \cdot \underline{M}_{\mathsf{O_B}}, \tag{2.15}$$

where $\underline{R} = [\underline{R}_{\mathsf{O_B}}\ \underline{R}_{\mathsf{P}_{11}}\ \underline{R}_{\mathsf{P}_{12}}\ \cdots\ \underline{R}_{\mathsf{P}_{24}}]^T$ is the column vectrix of resultant forces acting on each of the points and $\underline{M}_{\mathsf{O_B}}$ is the sum of the moments acting on the disk about its center of mass.

The resultant forces are given by

$$\begin{aligned}\underline{R}_{\mathsf{O}_\mathsf{B}} &= -c_x \upsilon_1 \underline{\mathfrak{n}}_1 - c_y \upsilon_2 \underline{\mathfrak{n}}_2 - (m a_\mathrm{g} + c_z \upsilon_3)\, \underline{\mathfrak{n}}_3 \\ \underline{R}_{\mathsf{P}_{ij}} &= F_{\mathrm{n}_{ij}} \underline{\mathfrak{b}}_3,\end{aligned} \tag{2.16}$$

where $F_{\mathrm{n}_{ij}} = F_{\mathrm{t}_{ij}} - F_{\mathrm{b}_{ij}}$ is the net force acting on the disk at point P_{ij}. The only moments modeled are the torsional squeeze film damping terms,

$$\underline{M}_{\mathsf{O}_\mathsf{B}} = -c_\theta \upsilon_4 \underline{\mathfrak{n}}_1 - c_\varphi \upsilon_5 \underline{\mathfrak{b}}_2. \tag{2.17}$$

Plugging the pertinent partial velocities, angular velocities, resultant forces, and moments into (2.15) yields

$$\mathcal{F} = \begin{bmatrix} -c_x \upsilon_1 + \sin\varphi \sum_{i,j} F_{\mathrm{n}_{ij}} \\ -c_y \upsilon_2 - \sin\theta \cos\varphi \sum_{i,j} F_{\mathrm{n}_{ij}} \\ -c_z \upsilon_3 - m a_\mathrm{g} + \cos\theta \cos\varphi \sum_{i,j} F_{\mathrm{n}_{ij}} \\ -c_\theta \upsilon_4 + \sum_{i,j} \beta_{ij} F_{\mathrm{n}_{ij}} \\ -c_\varphi \upsilon_5 + \sec\varphi \sum_{i,j} (x - \bar{x}_{ij})\, F_{\mathrm{n}_{ij}} \end{bmatrix}, \tag{2.18}$$

where $\beta_{ij} = (x - \bar{x}_{ij}) \tan\theta \sin\varphi + (\bar{y}_{ij} - y) \sec\theta \cos\varphi$. The generalized active forces constitute the left-hand side of the disk equations of motion described by Newton's second law. The motion of the disk is characterized once the generalized inertia forces that constitute the right-hand side of (2.3) are also computed. The generalized inertia forces are calculated according to

$$\mathcal{F}^\star = \hat{\underline{v}}_{\mathsf{O}_\mathsf{B}} \cdot \underline{R}^\star + \hat{\underline{\omega}}_\mathsf{B} \cdot \underline{M}^\star_{\mathsf{O}_\mathsf{B}}, \tag{2.19}$$

where the inertia resultant is given by

$$\underline{R}^\star = m \underline{a}_{\mathsf{O}_\mathsf{B}\mathsf{N}} = m \dot{\upsilon}_1 \underline{\mathfrak{n}}_1 + m \dot{\upsilon}_2 \underline{\mathfrak{n}}_2 + m \dot{\upsilon}_3 \underline{\mathfrak{n}}_3. \tag{2.20}$$

The inertial moment acting about the disk center of mass, $\underline{M}^\star_{\mathsf{O}_\mathsf{B}}$, is equal to the time derivative of the disk's inertial momentum in the N-frame:

$$\underline{M}^\star_{\mathsf{O}_\mathsf{B}} = \overset{\mathsf{N}}{\underline{H}}_{\mathsf{O}_\mathsf{B}\mathsf{N}}, \tag{2.21}$$

where $\underline{H}_{\mathsf{O}_\mathsf{B}\mathsf{N}}$ is the disk's inertial momentum about its center of mass in the N-frame and the N stacked above $\underline{H}_{\mathsf{O}_\mathsf{B}\mathsf{N}}$ indicates that the time derivative is taken with respect to the inertial

frame. The inertial momentum is a function of both the angular rotation of the disk and the disk's inertia,

$$\underline{H}_{\mathsf{O_B N}} = \underline{\omega}_{\mathsf{BN}} \cdot \underline{\underline{I}}_{\mathsf{O_B}}, \tag{2.22}$$

where $\underline{\underline{I}}_{\mathsf{O_B}} = J_{\mathrm{t}}\underline{\mathsf{b}}_1\underline{\mathsf{b}}_1 + J_{\mathrm{t}}\underline{\mathsf{b}}_2\underline{\mathsf{b}}_2 + J_{\mathrm{s}}\underline{\mathsf{b}}_3\underline{\mathsf{b}}_3$ is the inertia dyadic (tensor) of the disk about its center of mass. The inertia dyadic is written in the B-frame since the $\{\mathsf{B}_1, \mathsf{B}_2, \mathsf{B}_3\}$-axes are the principal axes of the disk, i.e., the inertia matrix is diagonal in the B-frame. The transverse- and spin-axis moments of inertia of the disk are denoted J_{t} and J_{s}, respectively, and their values are provided in Table 2.1. Plugging the inertia dyadic and angular momentum of the disk into (2.22) yields

$$\underline{H}_{\mathsf{O_B N}} = J_{\mathrm{t}}\upsilon_4 \cos\varphi \underline{\mathsf{b}}_1 + J_{\mathrm{t}}\upsilon_5 \underline{\mathsf{b}}_2 + J_{\mathrm{s}}\upsilon_4 \sin\varphi \underline{\mathsf{b}}_3. \tag{2.23}$$

Although the inertial momentum is written in the B-frame, its time derivative in the N-frame can be computed according to

$$\overset{\mathsf{N}}{\underline{H}}_{\mathsf{O_B N}} = \overset{\mathsf{B}}{\underline{H}}_{\mathsf{O_B N}} + \underline{\omega}_{\mathsf{BN}} \times \underline{H}_{\mathsf{O_B N}} \tag{2.24}$$

to yield

$$\begin{aligned} \overset{\mathsf{N}}{\underline{H}}_{\mathsf{O_B N}} = {} & \left((J_{\mathrm{s}} - 2J_{\mathrm{t}})\upsilon_4\upsilon_5 \sin\varphi + J_{\mathrm{t}}\dot{\upsilon}_4 \cos\varphi\right) \underline{\mathsf{b}}_1 + \left((J_{\mathrm{t}} - J_{\mathrm{s}})\upsilon_4^2 \sin\varphi\cos\varphi + J_{\mathrm{t}}\dot{\upsilon}_5\right) \underline{\mathsf{b}}_2 \\ & + \left(J_{\mathrm{s}}\upsilon_4\upsilon_5 \cos\varphi + J_{\mathrm{s}}\dot{\upsilon}_4 \sin\varphi\right) \underline{\mathsf{b}}_3. \end{aligned} \tag{2.25}$$

With each of the terms in (2.19) evaluated, the generalized inertia forces are given by

$$\mathcal{F}^\star = \begin{bmatrix} m\dot{\upsilon}_1 \\ m\dot{\upsilon}_2 \\ m\dot{\upsilon}_3 \\ 2(J_{\mathrm{s}} - J_{\mathrm{t}})\upsilon_4\upsilon_5 \sin\varphi\cos\varphi + (J_{\mathrm{s}}\sin^2\varphi + J_{\mathrm{t}}\cos^2\varphi)\dot{\upsilon}_4 \\ (J_{\mathrm{t}} - J_{\mathrm{s}})\upsilon_4^2 \sin\varphi\cos\varphi + J_t\dot{\upsilon}_5 \end{bmatrix}. \tag{2.26}$$

Computing (2.3) and substituting the time derivatives of the generalized coordinates for the

generalized speeds produces the ensuing set of nonlinear equations governing disk motion:

$$
\begin{aligned}
m\ddot{x} &= -c_x\dot{x} + \sin\varphi \sum_{i,j} F_{\mathrm{n}_{ij}} \\
m\ddot{y} &= -c_y\dot{y} - \sin\theta\cos\varphi \sum_{i,j} F_{\mathrm{n}_{ij}} \\
m\ddot{z} &= -c_z\dot{z} - ma_{\mathrm{g}} + \cos\theta\cos\varphi \sum_{i,j} F_{\mathrm{n}_{ij}} \\
\left(J_{\mathrm{s}}\sin^2\varphi + J_{\mathrm{t}}\cos^2\varphi\right)\ddot{\theta} &= -c_\theta\dot{\theta} + 2(J_{\mathrm{t}} - J_{\mathrm{s}})\dot{\theta}\dot{\varphi}\sin\varphi\cos\varphi + \sum_{i,j}\beta_{ij}F_{\mathrm{n}_{ij}} \\
J_{\mathrm{t}}\ddot{\varphi} &= -c_\varphi\dot{\varphi} + (J_{\mathrm{s}} - J_{\mathrm{t}})\dot{\theta}^2\sin\varphi\cos\varphi + \sec\varphi \sum_{i,j}(x - \bar{x}_{ij})\,F_{\mathrm{n}_{ij}}.
\end{aligned}
\tag{2.27}
$$

The governing equations of motion can also be obtained using energy formulations that rely on a generalization of Lagrange's formulation based on Kane's Method. The generalized Lagrangian, $\mathcal{L}$, is defined as

$$
\mathcal{L}(q, \upsilon, t) = \mathcal{K}(q, \upsilon, t) - V(q, t), \tag{2.28}
$$

where $\mathcal{K}$ is the generalized kinetic energy and V is the potential energy present in the disk. The generalized Lagrangian and generalized kinetic energy are identical to the standard definitions of the Lagrangian and kinetic energy, respectively, however, the generalized velocities, $\dot{q}$, are replaced with the generalized speeds. In the presence of non-conservative forces, Kane's equations for disk motion are given by

$$
\frac{d}{dt}\left(\frac{\partial\mathcal{L}}{\partial\upsilon}\frac{\partial\dot{q}}{\partial\upsilon}^{-1}\right) - \frac{\partial\mathcal{L}}{\partial q} + \frac{\partial\mathcal{L}}{\partial\upsilon}\frac{\partial\dot{q}}{\partial\upsilon}^{-1}\frac{\partial\dot{q}}{\partial q} = \mathcal{F}_{\mathrm{nc}}{}^{T}\frac{\partial\dot{q}}{\partial\upsilon}^{-1}, \tag{2.29}
$$

where $\mathcal{F}_{\mathrm{nc}}$ are the non-conservative forces acting on the disk. Only the viscous damping forces are non-conservative. All remaining generalized active forces are conservative forces, denoted $\mathcal{F}_{\mathrm{c}}$, that are related to the disk's potential energy according to

$$
Y^T\mathcal{F}_{\mathrm{c}} = -\frac{\partial V}{\partial q}^{T}. \tag{2.30}
$$

Computing the disk's potential energy from (2.30) is tedious due to the presence of electrostatic forces acting on the disk, nevertheless, plugging (2.28) and (2.30) into (2.29) and

recognizing that the generalized speeds are equal to the generalized velocities simplifies the disk's equations of motion to

$$\frac{d}{dt}\left(\frac{\partial \mathcal{K}}{\partial \upsilon}\right) - \frac{\partial \mathcal{K}}{\partial q} = \mathcal{F}_{\mathrm{c}}{}^{T} + \mathcal{F}_{\mathrm{nc}}{}^{T}. \tag{2.31}$$

The generalized kinetic energy is evaluated by computing the kinetic energy,

$$K(q, \dot{q}, t) = \frac{1}{2} m \underline{v}_{\mathsf{O_B N}} \cdot \underline{v}_{\mathsf{O_B N}} + \frac{1}{2} \underline{\omega}_{\mathsf{BN}} \cdot \underline{H}_{\mathsf{O_B N}}, \tag{2.32}$$

and replacing $\dot{q}$ with the generalized speeds according to (2.10):

$$\mathcal{K} = \frac{1}{2}\left[m\upsilon_1^2 + m\upsilon_2^2 + m\upsilon_3^2 + \left(\sin^2\varphi J_{\mathrm{s}} + \cos^2\varphi J_{\mathrm{t}}\right)\upsilon_4^2 + J_{\mathrm{t}}\upsilon_5^2\right]. \tag{2.33}$$

Taking the partial derivatives of $\mathcal{K}$ with respect to υ and q,

$$\begin{aligned} \frac{\partial \mathcal{K}}{\partial \upsilon} &= \begin{bmatrix} m\upsilon_1 & m\upsilon_2 & m\upsilon_3 & \left(J_{\mathrm{s}}\sin^2\varphi + J_{\mathrm{t}}\cos^2\varphi\right)\upsilon_4 & J_{\mathrm{t}}\upsilon_5 \end{bmatrix} \\ \frac{\partial \mathcal{K}}{\partial q} &= \begin{bmatrix} 0 & 0 & 0 & 0 & \left(J_{\mathrm{s}} - J_{\mathrm{t}}\right)\sin\varphi\cos\varphi\upsilon_4^2 \end{bmatrix}, \end{aligned} \tag{2.34}$$

the left-hand side of (2.31) is given by

$$\frac{d}{dt}\left(\frac{\partial \mathcal{K}}{\partial \upsilon}\right) - \frac{\partial \mathcal{K}}{\partial q} = \begin{bmatrix} m\dot{\upsilon}_1 \\ m\dot{\upsilon}_2 \\ m\dot{\upsilon}_3 \\ 2\left(J_{\mathrm{s}} - J_{\mathrm{t}}\right)\upsilon_4\upsilon_5\sin\varphi\cos\varphi + \left(J_{\mathrm{s}}\sin^2\varphi + J_{\mathrm{t}}\cos^2\varphi\right)\dot{\upsilon}_4 \\ J_{\mathrm{t}}\dot{\upsilon}_5 + \left(J_{\mathrm{t}} - J_{\mathrm{s}}\right)\upsilon_4^2\sin\varphi\cos\varphi \end{bmatrix}^T, \tag{2.35}$$

which is equal to $(\mathcal{F}^\star)^T$. Since the right-hand side of (2.31) is equal to $\mathcal{F}^T$, the equations of motion generated via energy formulations confirm the disk's governing equations presented in (2.27).

The glass plates constrain angular deflections of the disk to less than 3 mrad, so invoking

the small angle approximation simplifies the disk equations of motion to

$$\begin{aligned}
m\ddot{x} &= -c_x\dot{x} + \varphi \sum_{i,j} F_{\mathrm{n}_{ij}} \\
m\ddot{y} &= -c_y\dot{y} - \theta \sum_{i,j} F_{\mathrm{n}_{ij}} \\
m\ddot{z} &= -c_z\dot{z} - ma_{\mathrm{g}} + \sum_{i,j} F_{\mathrm{n}_{ij}} \\
J_{\mathrm{t}}\ddot{\theta} &= -c_\theta\dot{\theta} + 2\left(J_{\mathrm{t}} - J_{\mathrm{s}}\right)\varphi\dot{\theta}\dot{\varphi} + \sum_{i,j}\left(\bar{y}_{ij} - y\right) F_{\mathrm{n}_{ij}} \\
J_{\mathrm{t}}\ddot{\varphi} &= -c_\varphi\dot{\varphi} + \left(J_{\mathrm{s}} - J_{\mathrm{t}}\right)\varphi\dot{\theta}^2 + \sum_{i,j}\left(x - \bar{x}_{ij}\right) F_{\mathrm{n}_{ij}}.
\end{aligned} \tag{2.36}$$

Nevertheless, the equations remain nonlinear. A linearization about a nominal operating setpoint is pursued in Section 2.2.5. The electrostatic forcing terms in (2.36) confirm basic Newtonian mechanics principles: the vertical force is comprised of the net force exerted by all electrodes and the net electrostatic moments are simply the sum of each electrostatic force multiplied by its corresponding moment arm. A distinguishing feature of the system is the intrinsic coupling present between the lateral and tilt degrees of freedom. Lateral forces are produced by tilting the disk, so using the primary electrodes to control angular rotations of the disk provides a means of regulating in-plane motion of the disk.

2.2.2 Electrostatic Forces

Charge differentials between the (grounded) disk and each of electrodes result in net electrostatic forces on the disk. Since the system geometry constrains the roll and pitch angles to less than 3 mrad, the disk and electrodes are modeled as parallel plate capacitors in which the disk is assumed to be a thin rigid body so that the capacitive gaps are characterized by deflections of the disk center plane and measured at the centroids of the electrode-disk overlap areas. The vertical positions of the points on the disk where the lines given by $\{\mathsf{N}_1 = \bar{x}_{ij}, \mathsf{N}_2 = \bar{y}_{ij}\}$ intersect the disk center plane in the N-frame are given in (2.7), however, the small angle approximation simplifies this expression to

$$z_{ij} = z + (x - \bar{x}_{ij})\varphi + (\bar{y}_{ij} - y)\theta. \tag{2.37}$$

The gaps between the top electrodes and the disk are quantified by subtracting z_{ij} from the nominal gap when the disk is suspended in its nominal equilibrium position ($q = 0$). Similarly, the gaps between the disk and bottom electrodes are assessed by adding z_{ij} to the nominal gap.

The capacitances between the disk and electrodes are estimated by modeling each parallel plate capacitor as two series capacitors –one for each dielectric medium, air and photoresist. The top and bottom capacitances assocated with the air gaps are given by

$$C_{\mathrm{air,t}_{ij}} = \frac{\varepsilon_{\mathrm{air}}\varepsilon_0 A_{\mathcal{E}_{ij}}}{\frac{z_{\mathrm{sh}}}{2} - z_{ij}} \qquad C_{\mathrm{air,b}_{ij}} = \frac{\varepsilon_{\mathrm{air}}\varepsilon_0 A_{\mathcal{E}_{ij}}}{\frac{z_{\mathrm{sh}}}{2} + z_{ij}}, \tag{2.38}$$

respectively, where $\varepsilon_{\mathrm{air}}$ is the relative permittivity of air, ε_0 is the vacuum permittivity, and z_{sh} is the shim thickness, and

$$C_{\mathrm{pr}} = \frac{\varepsilon_{\mathrm{pr}}\varepsilon_0 A_{\mathcal{E}_{ij}}}{z_{\mathrm{pr}}} \tag{2.39}$$

is the capacitance across the layer of photoresist, where $\varepsilon_{\mathrm{pr}}$ is the relative permittivity of the photoresist and z_{pr} is the photoresist thickness. The thicknesses of the mediums that establish the capacitive gaps are listed in Table 2.2. The net top and bottom capacitances for the dual-dielectric gaps, $C_{\mathrm{t}_{ij}}$ and $C_{\mathrm{b}_{ij}}$, respectively, abide by the series capacitance relationship

$$\frac{1}{C_{\mathrm{t}_{ij}}} = \frac{1}{C_{\mathrm{air,t}_{ij}}} + \frac{1}{C_{\mathrm{pr}}} \qquad \frac{1}{C_{\mathrm{b}_{ij}}} = \frac{1}{C_{\mathrm{air,b}_{ij}}} + \frac{1}{C_{\mathrm{pr}}}. \tag{2.40}$$

Solving for $C_{\mathrm{t}_{ij}}$ and $C_{\mathrm{b}_{ij}}$ yields

$$C_{\mathrm{t}_{ij}} = \frac{\varepsilon_{\mathrm{air}}\varepsilon_0 A_{\mathcal{E}_{ij}}}{\frac{z_{\mathrm{sh}}}{2} + \frac{\varepsilon_{\mathrm{air}}}{\varepsilon_{\mathrm{pr}}} z_{\mathrm{pr}} - z_{ij}} \qquad C_{\mathrm{b}_{ij}} = \frac{\varepsilon_{\mathrm{air}}\varepsilon_0 A_{\mathcal{E}_{ij}}}{\frac{z_{\mathrm{sh}}}{2} + \frac{\varepsilon_{\mathrm{air}}}{\varepsilon_{\mathrm{pr}}} z_{\mathrm{pr}} + z_{ij}}. \tag{2.41}$$

Let $\varepsilon = \varepsilon_{\mathrm{air}}\varepsilon_0$ and define an "effective" nominal gap,

$$z_0 = \frac{z_{\mathrm{sh}}}{2} + \frac{\varepsilon_{\mathrm{air}}}{\varepsilon_{\mathrm{pr}}} z_{\mathrm{pr}}, \tag{2.42}$$

that is not dependent on the disk position. Using the expression in (2.42), the net top and bottom capacitances are given by

$$C_{\mathrm{t}_{ij}} = \frac{\varepsilon A_{\mathcal{E}_{ij}}}{z_0 - z_{ij}} \qquad C_{\mathrm{b}_{ij}} = \frac{\varepsilon A_{\mathcal{E}_{ij}}}{z_0 + z_{ij}}, \tag{2.43}$$

respectively.

The electrostatic energy stored in the top and bottom electrodes, $W_{\mathrm{t}_{ij}}$ and $W_{\mathrm{b}_{ij}}$, respectively, are given by

$$W_{\mathrm{t}_{ij}} = \frac{1}{2}\frac{Q_{\mathrm{t}_{ij}}^2}{C_{\mathrm{t}_{ij}}} \qquad W_{\mathrm{b}_{ij}} = \frac{1}{2}\frac{Q_{\mathrm{b}_{ij}}^2}{C_{\mathrm{b}_{ij}}}, \tag{2.44}$$

where $Q_{\mathrm{t}_{ij}}$ is the electrical charge stored on electrode $\mathcal{E}_{\mathrm{t}_{ij}}$ and $Q_{\mathrm{b}_{ij}}$ is the charge stored on electrode $\mathcal{E}_{\mathrm{b}_{ij}}$. The pull-in forces acting on the disk, assuming no charge losses, are computed as

$$\begin{aligned}
\underline{F}_{\mathrm{t}_{ij}} &= -\frac{\partial W_{\mathrm{t}_{ij}}}{\partial z}\underline{\mathsf{b}}_3 = \frac{1}{2}\frac{Q_{\mathrm{t}_{ij}}^2}{C_{\mathrm{t}_{ij}}^2}\frac{\partial C_{\mathrm{t}_{ij}}}{\partial z}\underline{\mathsf{b}}_3 = \frac{1}{2}\frac{\varepsilon A_{\mathcal{E}_{ij}}}{\left(z_0 - z_{ij}\right)^2}v_{\mathrm{t}_{ij}}^2\underline{\mathsf{b}}_3 \\
\underline{F}_{\mathrm{b}_{ij}} &= -\frac{\partial W_{\mathrm{b}_{ij}}}{\partial z}\underline{\mathsf{b}}_3 = \frac{1}{2}\frac{Q_{\mathrm{b}_{ij}}^2}{C_{\mathrm{b}_{ij}}^2}\frac{\partial C_{\mathrm{b}_{ij}}}{\partial z}\underline{\mathsf{b}}_3 = -\frac{1}{2}\frac{\varepsilon A_{\mathcal{E}_{ij}}}{\left(z_0 + z_{ij}\right)^2}v_{\mathrm{b}_{ij}}^2\underline{\mathsf{b}}_3,
\end{aligned} \tag{2.45}$$

where the current-voltage relationship for a capacitor is used to introduce the electrode voltages, $v_{\mathrm{t}_{ij}}$ and $v_{\mathrm{b}_{ij}}$, for electrodes $\mathcal{E}_{\mathrm{t}_{ij}}$ and $\mathcal{E}_{\mathrm{b}_{ij}}$, respectively. The magnitudes of $\underline{F}_{\mathrm{t}_{ij}}$ and $\underline{F}_{\mathrm{b}_{ij}}$ comprise the electrostatic force terms of the previous section, denoted $F_{\mathrm{t}_{ij}}$ and $F_{\mathrm{b}_{ij}}$, respectively. The magnitude of the net electrostatic force acting on the disk due to an electrode pair, $F_{\mathrm{n}_{ij}}$, is

$$F_{\mathrm{n}_{ij}} = \frac{\varepsilon A_{\mathcal{E}_{ij}}}{2}\left(\frac{v_{\mathrm{t}_{ij}}^2}{\left(z_0 - z_{ij}\right)^2} - \frac{v_{\mathrm{b}_{ij}}^2}{\left(z_0 + z_{ij}\right)^2}\right). \tag{2.46}$$

The potentials are part of the electrical subsystem states and their presence shows how the disk response is dependent on the transformer voltages:

$$\begin{aligned}
m\ddot{x} &= -c_x\dot{x} + \frac{\varepsilon\varphi}{2}\sum_{i,j} A_{\mathcal{E}_{ij}}\left(\frac{v_{\mathrm{t}_{ij}}^2}{\left(z_0 - z_{ij}\right)^2} - \frac{v_{\mathrm{b}_{ij}}^2}{\left(z_0 + z_{ij}\right)^2}\right) \\
m\ddot{y} &= -c_y\dot{y} - \frac{\varepsilon\theta}{2}\sum_{i,j} A_{\mathcal{E}_{ij}}\left(\frac{v_{\mathrm{t}_{ij}}^2}{\left(z_0 - z_{ij}\right)^2} - \frac{v_{\mathrm{b}_{ij}}^2}{\left(z_0 + z_{ij}\right)^2}\right) \\
m\ddot{z} &= -c_z\dot{z} - ma_{\mathrm{g}} + \frac{\varepsilon}{2}\sum_{i,j} A_{\mathcal{E}_{ij}}\left(\frac{v_{\mathrm{t}_{ij}}^2}{\left(z_0 - z_{ij}\right)^2} - \frac{v_{\mathrm{b}_{ij}}^2}{\left(z_0 + z_{ij}\right)^2}\right) \\
J_{\mathrm{t}}\ddot{\theta} &= -c_\theta\dot{\theta} + 2\left(J_{\mathrm{t}} - J_{\mathrm{s}}\right)\varphi\dot{\theta}\dot{\varphi} + \frac{\varepsilon}{2}\sum_{i,j}\left(\bar{y}_{ij} - y\right)A_{\mathcal{E}_{ij}}\left(\frac{v_{\mathrm{t}_{ij}}^2}{\left(z_0 - z_{ij}\right)^2} - \frac{v_{\mathrm{b}_{ij}}^2}{\left(z_0 + z_{ij}\right)^2}\right) \\
J_{\mathrm{t}}\ddot{\varphi} &= -c_\varphi\dot{\varphi} + \left(J_{\mathrm{s}} - J_{\mathrm{t}}\right)\varphi\dot{\theta}^2 + \frac{\varepsilon}{2}\sum_{i,j}\left(x - \bar{x}_{ij}\right)A_{\mathcal{E}_{ij}}\left(\frac{v_{\mathrm{t}_{ij}}^2}{\left(z_0 - z_{ij}\right)^2} - \frac{v_{\mathrm{b}_{ij}}^2}{\left(z_0 + z_{ij}\right)^2}\right).
\end{aligned} \tag{2.47}$$

Table 2.2: Gap Parameters for Electrode Configuration I

Symbol	Description	Value
z_{sh}	shim thickness	229μm
z_{pr}	photoresist thickness	20μm
z_0	"effective" nominal electrode-disk gap	119μm

These nonlinear equations of motion can be compactly expressed by the set of coupled first-order differential equations

$$\frac{d}{dt}\begin{bmatrix} q \\ \dot{q} \end{bmatrix} = \begin{bmatrix} \dot{q} \\ f(q, \dot{q}, w_{\text{tf}}) \end{bmatrix}, \tag{2.48}$$

where w_{tf} characterizes the transformer states.

2.2.3 Transformer Dynamics

The transformers are modeled to include non-idealities such as leakage inductances, winding resistances, and stray capacitance. Each of the transformers are assumed to be identical, though only the primary electrode transformers are connected to the control inputs and the connections to the electrodes vary for the primary and lateral cases. A schematic of the non-idealized primary electrode transformer is displayed in Figure 2.8, which shows the transformer connections to the electrodes and control signal, v_{c_j}. The supply transformers are not modeled, however, they produce a nearly constant amplitude current,

$$i_{\text{ct}_1} = a_{\text{ct}_1} \cos(\omega_0 t) \tag{2.49}$$

for the primary electrodes, that serves as a second input to the transformer subsystem in Figure 2.8. Note that ω_0 is the 25 kHz carrier frequency. All resistances, inductances, and capacitances (excluding the variable electrode-disk capacitances) were evaluated using an impedance analyzer in [AM21] and are listed in Table 2.3 for reference. An overdetermined set of equations is developed for the primary electrode transformers using first-order current-

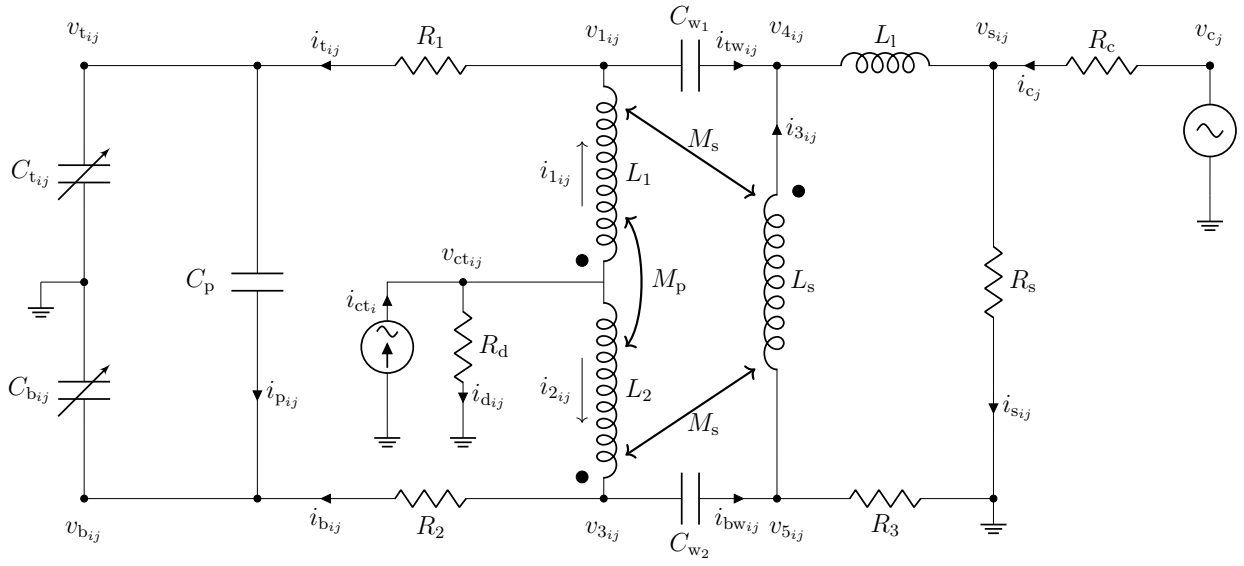

Figure 2.8: Non-idealized primary electrode transformer model. Mutual and leakage inductances, winding resistances, and parasitic and interwinding capacitances are modeled.

voltage relations:

$$
\begin{aligned}
C_{\mathrm{t}_{ij}}\dot{v}_{\mathrm{t}_{ij}} &= i_{\mathrm{t}_{ij}} - i_{\mathrm{p}_{ij}} & v_{3_{ij}} - v_{\mathrm{b}_{ij}} &= R_2 i_{\mathrm{b}_{ij}} \\
C_{\mathrm{b}_{ij}}\dot{v}_{\mathrm{b}_{ij}} &= i_{\mathrm{b}_{ij}} + i_{\mathrm{p}_{ij}} & v_{\mathrm{ct}_{ij}} &= i_{\mathrm{d}_{ij}} R_{\mathrm{d}} \\
C_{\mathrm{p}}\left(\dot{v}_{\mathrm{t}_{ij}} - \dot{v}_{\mathrm{b}_{ij}}\right) &= i_{\mathrm{p}_{ij}} & v_{5_{ij}} &= R_3\left(i_{\mathrm{bw}_{ij}} - i_{3_{ij}}\right) \\
C_{\mathrm{w}_1}\left(\dot{v}_{1_{ij}} - \dot{v}_{4_{ij}}\right) &= i_{\mathrm{tw}_{ij}} & v_{\mathrm{s}_{ij}} &= R_{\mathrm{s}} i_{\mathrm{s}_{ij}} \\
C_{\mathrm{w}_2}\left(\dot{v}_{3_{ij}} - \dot{v}_{5_{ij}}\right) &= i_{\mathrm{bw}_{ij}} & v_{\mathrm{c}_j} - v_{\mathrm{s}_{ij}} &= R_{\mathrm{c}} i_{\mathrm{c}_j} \\
L_1\dot{i}_{1_{ij}} - M_{\mathrm{p}}\dot{i}_{2_{ij}} - M_{\mathrm{s}}\dot{i}_{3_{ij}} &= v_{\mathrm{ct}_{ij}} - v_{1_{ij}} & i_{\mathrm{ct}_i} &= i_{\mathrm{d}_{ij}} + i_{1_{ij}} + i_{2_{ij}} \\
-M_{\mathrm{p}}\dot{i}_{1_{ij}} + L_2\dot{i}_{2_{ij}} + M_{\mathrm{s}}\dot{i}_{3_{ij}} &= v_{\mathrm{ct}_{ij}} - v_{3_{ij}} & i_{1_{ij}} &= i_{\mathrm{t}_{ij}} + i_{\mathrm{tw}_{ij}} \\
-M_{\mathrm{s}}\dot{i}_{1_{ij}} + M_{\mathrm{s}}\dot{i}_{2_{ij}} + L_{\mathrm{s}}\dot{i}_{3_{ij}} &= v_{5_{ij}} - v_{4_{ij}} & i_{2_{ij}} &= i_{\mathrm{b}_{ij}} + i_{\mathrm{bw}_{ij}} \\
L_{\mathrm{l}}\left(\dot{i}_{\mathrm{tw}_{ij}} + \dot{i}_{3_{ij}}\right) &= v_{4_{ij}} - v_{s_{ij}} & i_{\mathrm{tw}_{ij}} + i_{3_{ij}} + i_{\mathrm{c}_j} &= i_{\mathrm{s}_{ij}}. \\
v_{1_{ij}} - v_{\mathrm{t}_{ij}} &= R_1 i_{\mathrm{t}_{ij}}
\end{aligned}
\tag{2.50}
$$

This system of equations is compactly written in the state-space form

$$
\begin{aligned}
M_{\mathrm{tf}_{1j}}(q)\dot{w}_{\mathrm{tf}_{1j}} &= A_{\mathrm{tf}_1} w_{\mathrm{tf}_{1j}} + (-1)^{j-1} B_{\mathrm{ct}_1} i_{\mathrm{ct}_1} + B_v v_{\mathrm{c}_j} \\
v_{\mathrm{s}_{1j}} &= C_{\mathrm{tf}_1} w_{\mathrm{tf}_{1j}}
\end{aligned}
\qquad j = 1, 2, 3, 4 \tag{2.51}
$$

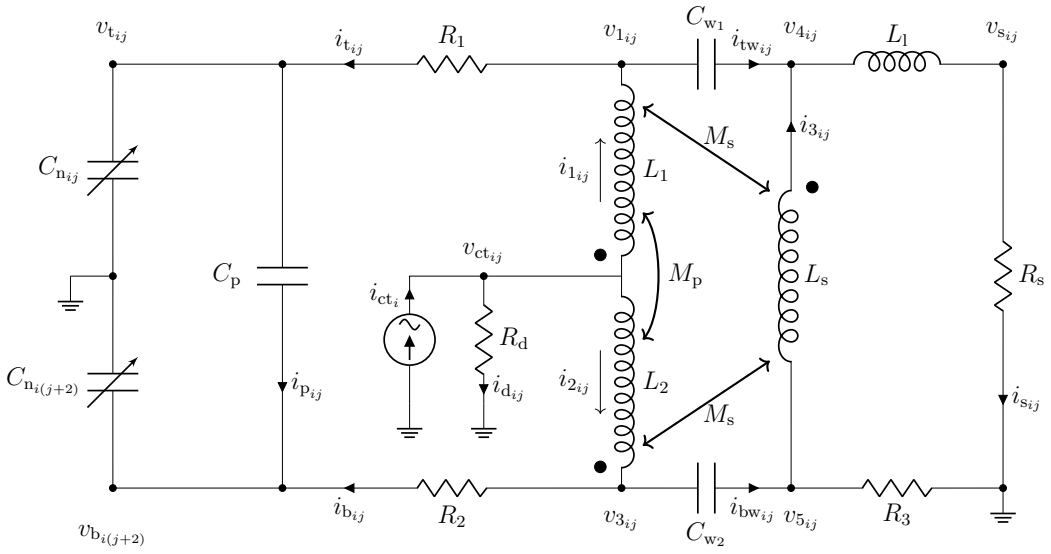

Figure 2.9: Non-idealized lateral electrode transformer model. The inductances, capacitances, and resistances internal to the transformer are modeled identically to the primary electrode transformers. Only the electrode connections and lack of a voltage source differ from the primary electrode transformers.

for each primary electrode transformer, where all currents and voltages, excluding the center tap current and control voltage input, comprise the 19-state vector, $\mathrm{w}_{\mathrm{tf}_{1j}}$. The subscript "$1j$" indicates that the transformer is connected to the $\{\mathcal{E}_{\mathrm{t}_{1j}}, \mathcal{E}_{\mathrm{b}_{1j}}\}$ electrode pair. The $(-1)^{j-1}$ term in front of the center tap current input signal accounts for the alternating sign of the signal between adjacent channels created by the supply transformers. While the phase of each control voltage input must be adjusted accordingly, the $(-1)^{j-1}$ term is omitted from the B_v input matrix since it is accounted for upstream in the modulation phases, ψ_{c_j}.

An electrical schematic of the transformer connection to the lateral electrodes is also provided (see Figure 2.9) since the electrode-transformer configuration differs for the primary and lateral electrodes. No control signal is presented to the lateral transformers and the center tap current,

$$i_{\mathrm{ct}_2} = a_{\mathrm{ct}_2} \cos\left(\omega_0 t\right), \tag{2.52}$$

is operated at a lower amplitude than i_{ct_1}. The equations of motion for each lateral electrode transformer are nearly identical to those in (2.50), however, the i_{c_j} state and v_{c_j} input are removed and the top and bottom electrode-disk capacitances are replaced with the electrode-

Table 2.3: Transformer Circuit Parameters

Symbol	Description	Value
L_1, L_2	primary inductances	2.1 H
L_s	secondary inductance	1.53 mH
L_l	leakage inductance	2.47 μH
M_p	primary-primary mutual inductance	2.1 H
M_s	primary-secondary mutual inductance	56.7 mH
C_p	parasitic capacitance	17 pF
C_{w_1}, C_{w_2}	interwinding capacitances	70 pF
R_1, R_2	primary winding resistances	504 Ω
R_3	secondary winding resistance	0.54 Ω
R_c	control resistor	150 Ω
R_s	shunt resistor	150 Ω
R_d	current sink resistor	1 MΩ

disk capacitances of antipodal electrodes. Because the top and bottom lateral electrodes are shorted, the electrode-disk capacitors for $\mathcal{E}_{\mathrm{t}_{2j}}$ and $\mathcal{E}_{\mathrm{b}_{2j}}$ act in parallel and the net capacitance between these electrodes and the disk is given by

$$C_{\mathrm{n}_{2j}} = \varepsilon A_{\mathcal{E}_{2j}} \left(\frac{1}{z_0 - z_{2j}} + \frac{1}{z_0 + z_{2j}} \right). \tag{2.53}$$

The overdetermined set of coupled first-order equations for each lateral electrode transformer is succinctly written as

$$\begin{aligned} M_{\mathrm{tf}_{2j}}(q)\dot{w}_{\mathrm{tf}_{2j}} &= A_{\mathrm{tf}_2} w_{\mathrm{tf}_{2j}} + (-1)^{j-1} B_{\mathrm{ct}_2} i_{\mathrm{ct}_2} \\ v_{\mathrm{s}_{2j}} &= C_{\mathrm{tf}_2} w_{\mathrm{tf}_{2j}}, \end{aligned} \qquad j = 1, 2 \tag{2.54}$$

where the state dimension is 18. The $j = 1$ set of equations is written with respect to the $\mathcal{E}_{21}$-$\mathcal{E}_{23}$ electrode pair (the top/bottom electrode subscript is omitted here since the top and bottom electrodes are shorted and act in parallel as a single electrode). Similarly, the transformer connected to the $\mathcal{E}_{\mathrm{t}_{22}}$, $\mathcal{E}_{\mathrm{b}_{22}}$, $\mathcal{E}_{\mathrm{t}_{24}}$, and $\mathcal{E}_{\mathrm{b}_{24}}$ electrodes is represented by the $j = 2$ set of equations in (2.54).

The six transformer subsystems collectively act as the six-input/six-output system

$$\begin{aligned} M_\mathrm{tf}(q)\dot{w}_\mathrm{tf} &= A_\mathrm{tf} w_\mathrm{tf} + B_\mathrm{ct} i_\mathrm{ct} + B_\mathrm{c} v_\mathrm{c} \\ v_\mathrm{s} &= C_\mathrm{tf} w_\mathrm{tf}, \end{aligned} \tag{2.55}$$

whose inputs, i_{ct} and v_{c}, and output, v_{s}, are

$$i_{\mathrm{ct}} = \begin{bmatrix} i_{\mathrm{ct}_1} \\ i_{\mathrm{ct}_2} \end{bmatrix}, \quad v_{\mathrm{c}} = \begin{bmatrix} v_{\mathrm{c}_1} \\ \vdots \\ v_{\mathrm{c}_4} \end{bmatrix}, \quad v_{\mathrm{s}} = \begin{bmatrix} v_{\mathrm{s}_1} \\ \vdots \\ v_{\mathrm{s}_6} \end{bmatrix},$$

where each of sense voltages, $v_{\mathrm{s}_{ij}}$, has been relabeled so that the subscript "ij" is replaced with the subscript "k" according to the relationship

$$k = 4(i-1) + j \begin{cases} i = 1, & j = 1,2,3,4 \\ i = 2, & j = 1,2. \end{cases}$$

For example, $v_{\mathrm{s}_{12}}$ becomes v_{s_2} and $v_{\mathrm{s}_{21}}$ becomes v_{s_5}. Using this notation, the subscript indices are representative of the measurement number, i.e., v_{s_1} is the first measurement and v_{s_6} is the sixth and final measurement. This notation was adopted in Section 2.1 and the sampled signal g_k is electrically connected to the transformer signal v_{s_k}. The state vector in (2.55) is given by

$$w_{\mathrm{tf}} = \begin{bmatrix} w_{\mathrm{tf}_{11}} & w_{\mathrm{tf}_{12}} & w_{\mathrm{tf}_{13}} & w_{\mathrm{tf}_{14}} & w_{\mathrm{tf}_{21}} & w_{\mathrm{tf}_{22}} \end{bmatrix}^T$$

and the aggregate state-space matrices are

$$\begin{aligned} M_{\mathrm{tf}}(q) &= \mathrm{diag}\left(M_{\mathrm{tf}_{11}}, M_{\mathrm{tf}_{12}}, M_{\mathrm{tf}_{13}}, M_{\mathrm{tf}_{14}}, M_{\mathrm{tf}_{21}}, M_{\mathrm{tf}_{22}}\right) \in \mathbb{R}^{112\times 112} \\ A_{\mathrm{tf}} &= \mathrm{diag}\left(A_{\mathrm{tf}_1}, A_{\mathrm{tf}_1}, A_{\mathrm{tf}_1}, A_{\mathrm{tf}_1}, A_{\mathrm{tf}_2}, A_{\mathrm{tf}_2}\right) \in \mathbb{R}^{112\times 112} \\ C_{\mathrm{tf}} &= \mathrm{diag}\left(C_{\mathrm{tf}_1}, C_{\mathrm{tf}_1}, C_{\mathrm{tf}_1}, C_{\mathrm{tf}_1}, C_{\mathrm{tf}_2}, C_{\mathrm{tf}_2}\right) \in \mathbb{R}^{6\times 112}, \end{aligned}$$

$$B_{\mathrm{ct}} = \begin{bmatrix} B_{\mathrm{ct}_1} & 0 \\ -B_{\mathrm{ct}_1} & 0 \\ B_{\mathrm{ct}_1} & 0 \\ -B_{\mathrm{ct}_1} & 0 \\ 0 & B_{\mathrm{ct}_2} \\ 0 & -B_{\mathrm{ct}_2} \end{bmatrix} \in \mathbb{R}^{112\times 2}, \quad B_{\mathrm{c}} = \begin{bmatrix} B_v & 0 & 0 & 0 \\ 0 & B_v & 0 & 0 \\ 0 & 0 & B_v & 0 \\ 0 & 0 & 0 & B_v \\ 0 & 0 & 0 & 0 \\ 0 & 0 & 0 & 0 \end{bmatrix} \in \mathbb{R}^{112\times 4},$$

where $\mathrm{diag}(\cdot)$ represents the block diagonal concatenation of the matrix arguments. The transformer states are coupled to the disk's kinematic variables, q, by the matrix M_{tf}, which contains the electrode-disk capacitances. Model reduction using a singular value decomposition is performed in Section 2.2.5 so that the redundant constraints in (2.55) are omitted.

Table 2.4: Analog Filter Parameters

Symbol	Type	Poles	Corner Frequency
H_{sm}	low-pass Butterworth	2	5 kHz
H_{aa}	low-pass Butterworth	4	1 kHz

2.2.4 Analog Filtering Dynamics

The analog filtering electronics are also modeled and are based on the filter parameters provided in Table 2.4. The input electronics are governed by

$$\begin{aligned} \dot{w}_{\text{sm}} &= A_{\text{sm}} w_{\text{sm}} + B_{\text{sm}} u \\ v_{\text{c}} &= \mathcal{C}_{\text{c}} C_{\text{sm}} w_{\text{sm}}, \end{aligned} \tag{2.56}$$

where $\mathcal{C}_{\text{c}} = k_{\text{c}} \operatorname{diag}(\cos(\omega_0 t + \psi_{\text{c}_1}), \ldots, \cos(\omega_0 t + \psi_{\text{c}_4}))$ is the diagonal matrix of sinusoids describing the analog multiplier and amplification, and $(A_{\text{sm}}, B_{\text{sm}}, C_{\text{sm}})$ characterizes the Butterworth smoothing filters with state variable w_{sm}. The analog gain on the input electronics, k_{c}, is equal to 9.3. The modulation phases of adjacent channels are 180° out of phase with one another to account for the alternating sign of the current in adjacent channels created by the center tap supply transformers, i.e., $\psi_{\text{c}_2} = \psi_{\text{c}_1} + \pi$. Furthermore, these phases are chosen so that a positive u_j results in a net lifting force acting on the disk relative to the $\{\mathcal{E}_{\text{t}_{1j}}, \mathcal{E}_{\text{t}_{1j}}\}$ electrode pair. The dynamics of the output electronics are represented by

$$\begin{aligned} \dot{w}_{\text{aa}} &= A_{\text{aa}} w_{\text{aa}} + B_{\text{aa}} \mathcal{C}_{\text{s}} v_{\text{s}} \\ g &= C_{\text{aa}} w_{\text{aa}}, \end{aligned} \tag{2.57}$$

where $\mathcal{C}_{\text{s}} = \operatorname{diag}(k_{\text{s}_1} \cos(\omega_0 t + \psi_{\text{s}_1}), \ldots, k_{\text{s}_6} \cos(\omega_0 t + \psi_{\text{s}_6}))$ characterizes the analog demodulator and sensing amplification, and $(A_{\text{aa}}, B_{\text{aa}}, C_{\text{aa}})$ describes the Butterworth anti-alias filters with state vector w_{aa}. The analog transduction gains for the sense electronics vary by channel. The gains corresponding to the primary electrode measurements, i.e., $\{k_{\text{s}_1}, \ldots, k_{\text{s}_4}\}$, are each equal to 1.9, meanwhile the lateral channel gains, k_{s_5} and k_{s_6}, take on the value 6.3. Differences in the phase of each transformer subsystem created by the alternating signs of the center tap supply currents are accounted for in the demodulation phases, ψ_{s_j}, so that an increase in the vertical position of the disk local to each primary electrode pair results in a

positive change in g_j. Similarly, positive motion along the N_1- and N_2-axes is measured as net positive changes in g_5 and g_6, respectively. The coupled, time-varying dynamics of the analog subsystem of the plant are collectively governed by

$$\begin{aligned}
\dot{w}_{\mathrm{sm}} &= A_{\mathrm{sm}} w_{\mathrm{sm}} + B_{\mathrm{sm}} u \\
M_{\mathrm{tf}}(q)\dot{w}_{\mathrm{tf}} &= B_{\mathrm{c}} \mathcal{C}_{\mathrm{c}} C_{\mathrm{sm}} w_{\mathrm{sm}} + A_{\mathrm{tf}} w_{\mathrm{tf}} + B_{\mathrm{ct}} i_{\mathrm{ct}} \\
\frac{d}{dt}\begin{bmatrix} q \\ \dot{q} \end{bmatrix} &= \begin{bmatrix} \dot{q} \\ f(q, \dot{q}, w_{\mathrm{tf}}) \end{bmatrix} \\
\dot{w}_{\mathrm{aa}} &= B_{\mathrm{aa}} \mathcal{C}_{\mathrm{s}} C_{\mathrm{tf}} w_{\mathrm{tf}} + A_{\mathrm{aa}} w_{\mathrm{aa}} \\
g &= C_{\mathrm{aa}} w_{\mathrm{aa}}.
\end{aligned} \tag{2.58}$$

2.2.5 Linearization About Operating Point

The governing equations of motion are nonlinear and overdetermined, however, small signal linearization about a nominal operating point is used to evaluate a linear time-periodic approximation of the plant. Futhermore, careful selection of the DSP sampling period to be an integer multiple of the carrier signal period yields a time-invariant discrete-time estimate of the system. The desired nominal setpoint is $\bar{q} = 0$, $\dot{\bar{q}} = 0$ since the disk is designed to be suspended at the center plane between the glass plates. A periodic solution of (2.58) exists at this setpoint because the mean value of all forces and moments acting on the disk sum to zero when a constant nonzero control input, denoted $\bar{u}$, is applied to counteract gravity. Due to the rectification of transformer primary voltages vis-à-vis (2.45), the $2\omega_0$ components of the forces and moments are neglected since the disk's inertia effectively attenuates these signals. When the disk is suspended in its nominal position, the periodic solution of the transformer states is given by

$$\bar{w}_{\mathrm{tf}}(t) \stackrel{r}{=} (\jmath\omega_0 M_{\mathrm{tf}}(\bar{q}) - A_{\mathrm{tf}})^{-1} \begin{bmatrix} B_{\mathrm{ct}} & B_{\mathrm{c}} \end{bmatrix} \begin{bmatrix} a_{\mathrm{ct}} \\ -k_{\mathrm{c}} E_{\mathrm{c}} C_{\mathrm{sm}} A_{\mathrm{sm}}^{-1} B_{\mathrm{sm}} \bar{u} \end{bmatrix} e^{\jmath\omega_0 t}, \tag{2.59}$$

where $a_{\mathrm{ct}} = [a_{\mathrm{ct}_1}\ a_{\mathrm{ct}_2}]^T$, $E_{\mathrm{c}} = \mathrm{diag}(e^{\jmath\psi_{\mathrm{c}_1}}, \ldots, e^{\jmath\psi_{\mathrm{c}_4}})$, and $\jmath$ is the imaginary unit, not to be confused with the subscript, j, that indicates the electrode number. Linear variational

equations are computed by introducing perturbation variables to each of the plant inputs, outputs, and states:

$$\begin{aligned} u &= \bar{u} + \delta_u & w_{\mathrm{sm}} &= \bar{w}_{\mathrm{sm}} + \delta_{\mathrm{sm}} & w_{\mathrm{tf}} &= \bar{w}_{\mathrm{tf}} + \delta_{\mathrm{tf}} \\ q &= 0 + \delta_q & \dot{q} &= 0 + \delta_{\dot{q}} & w_{\mathrm{aa}} &= \bar{w}_{\mathrm{aa}} + \delta_{\mathrm{aa}} \\ & & g &= \bar{g} + \delta_g. & & \end{aligned}$$

The bar notation represents the signals that are a solution of (2.58) at the setpoint and $\{\delta_u, \delta_{\mathrm{sm}}, \ldots\}$ represent the deviations. The matrix $M_{\mathrm{tf}}(q)$ is continuously differentiable for all physically realizable disk configurations and is approximated in a neighborhood of $\bar{q} = 0$ by

$$M_{\mathrm{tf}}(q) \approx M_{\mathrm{tf}}(\bar{q}) + \underbrace{\frac{\partial M_{\mathrm{tf}}}{\partial x}(\bar{q})}_{M_x}\delta_x + \underbrace{\frac{\partial M_{\mathrm{tf}}}{\partial y}(\bar{q})}_{M_y}\delta_y + \underbrace{\frac{\partial M_{\mathrm{tf}}}{\partial z}(\bar{q})}_{M_z}\delta_z + \underbrace{\frac{\partial M_{\mathrm{tf}}}{\partial \theta}(\bar{q})}_{M_\theta}\delta_\theta + \underbrace{\frac{\partial M_{\mathrm{tf}}}{\partial \varphi}(\bar{q})}_{M_\varphi}\delta_\varphi. \quad (2.60)$$

Substituting the perturbed variables and (2.60) into (2.58) and retaining only the linear terms produced by approximating $M(q)$ yields the set of first-order differential equations

$$\begin{aligned} \dot{\delta}_{\mathrm{sm}} &= A_{\mathrm{sm}}\delta_{\mathrm{sm}} + B_{\mathrm{sm}}\delta_u \\ M(\bar{q})\dot{\delta}_{\mathrm{tf}} &= B_{\mathrm{c}}\mathcal{C}_{\mathrm{c}}C_{\mathrm{sm}}\delta_{\mathrm{sm}} + A_{\mathrm{tf}}\delta_{\mathrm{tf}} - \left(M_x\delta_x + M_y\delta_y + M_z\delta_z + M_\theta\delta_\theta + M_\varphi\delta_\varphi\right)\dot{\bar{w}}_{\mathrm{tf}} \\ \dot{\delta}_q &= \delta_{\dot{q}} \\ \dot{\delta}_{\dot{q}} &= \nabla_{w_{\mathrm{tf}}} f(\bar{q}, \dot{\bar{q}}, \bar{w}_{\mathrm{tf}})\delta_{\mathrm{tf}} + \nabla_q f(\bar{q}, \dot{\bar{q}}, \bar{w}_{\mathrm{tf}})\delta_q + \nabla_{\dot{q}} f(\bar{q}, \dot{\bar{q}}, \bar{w}_{\mathrm{tf}})\delta_{\dot{q}} \\ \dot{\delta}_{\mathrm{aa}} &= A_{\mathrm{aa}}\delta_{\mathrm{aa}} + B_{\mathrm{aa}}\mathcal{C}_{\mathrm{s}}C_{\mathrm{tf}}\delta_{\mathrm{tf}} \\ \delta_g &= C_{\mathrm{aa}}\delta_{\mathrm{aa}}, \end{aligned} \quad (2.61)$$

where $\nabla_{w_{\mathrm{tf}}} f$, $\nabla_q f$, and $\nabla_{\dot{q}} f$ are the gradients of the generalized forces and torques with respect to w_{tf}, q, and $\dot{q}$, respectively.

The transformer subsystem, however, is overdetermined: w_{tf} contains 112 states yet the rank of $M(\bar{q})$ is 36. A model reduction via a singular value decomposition-based coordinate transformation resolves the overdetermined constraints. A singular value decomposition of

$M(\bar{q})$ is expressed as

$$M(\bar{q}) = \underbrace{\begin{bmatrix} U_1 & U_2 \end{bmatrix}}_{U} \begin{bmatrix} \Sigma_1 & 0 \\ 0 & 0 \end{bmatrix} \underbrace{\begin{bmatrix} V_1^T \\ V_2^T \end{bmatrix}}_{V^T}, \tag{2.62}$$

where the unitary U and V matrices are partitioned such that $U_1 \in \mathbb{R}^{112\times 36}$, $\Sigma_1 \in \mathbb{R}^{36\times 36}$, and $V_1 \in \mathbb{R}^{112\times 36}$. A new set of transformer perturbation coordinates are defined according to

$$\delta_{\text{tf}} = \begin{bmatrix} V_1 & V_2 \end{bmatrix} \begin{bmatrix} \delta_1 \\ \delta_2 \end{bmatrix} \tag{2.63}$$

so that δ_1 comprises the states of the truncated model, i.e., the essential states for describing the transformer dynamics, and δ_2 constitutes the states that have no impact on the transformer dynamics.

Plugging (2.62) and (2.63) into (2.61) produces

$$U_1\Sigma_1\dot{\delta}_1 = B_{\text{c}}\mathcal{C}_{\text{c}}C_{\text{sm}}\delta_{\text{sm}} + A_{\text{tf}}V_1\delta_1 + A_{\text{tf}}V_2\delta_2 - M_q\dot{\overline{W}}_{\text{tf}}\delta_q, \tag{2.64}$$

where $M_q = [M_x\ M_y\ M_z\ M_\theta\ M_\varphi]$ and $\dot{\overline{W}}_{\text{tf}} = \text{diag}\left(\dot{\bar{w}},\ \dot{\bar{w}}, \dot{\bar{w}},\ \dot{\bar{w}},\ \dot{\bar{w}}\right)$. Independently left multiplying by U_1^T and U_2^T yields the set of equations

$$\begin{aligned} \Sigma_1\dot{\delta}_1 &= U_1^TB_{\text{c}}\mathcal{C}_{\text{c}}C_{\text{sm}}\delta_{\text{sm}} + U_1^TA_{\text{tf}}V_1\delta_1 + U_1^TA_{\text{tf}}V_2\delta_2 - U_1^TM_q\dot{\overline{W}}_{\text{tf}}\delta_q \\ 0 &= U_2^TB_{\text{c}}\mathcal{C}_{\text{c}}C_{\text{sm}}\delta_{\text{sm}} + U_2^TA_{\text{tf}}V_1\delta_1 + U_2^TA_{\text{tf}}V_2\delta_2 - U_2^TM_q\dot{\overline{W}}_{\text{tf}}\delta_q, \end{aligned} \tag{2.65}$$

where $U_2^TA_{\text{tf}}V_2$ is invertible so that δ_2 can be expressed in terms of δ_{sm}, δ_1, and δ_q:

$$\delta_2 = -\left(U_2^TA_{\text{tf}}V_2\right)^{-1}U_2^T\left(B_{\text{c}}\mathcal{C}_{\text{c}}C_{\text{sm}}\delta_{\text{sm}} + A_{\text{tf}}V_1\delta_1 - M_q\dot{\overline{W}}_{\text{tf}}\delta q\right). \tag{2.66}$$

Plugging this expression for δ_2 into the differential equation describing the essential states of the transformer dynamics and defining $Q = V_2\left(U_2^TA_{\text{tf}}V_2\right)^{-1}U_2^T$ and $R = \Sigma_1^{-1}U_1^T\left(I - A_{\text{tf}}Q\right)$ yields

$$\dot{\delta}_1 = RB_{\text{c}}\mathcal{C}_{\text{c}}C_{\text{sm}}\delta_{\text{sm}} + RA_{\text{tf}}V_1\delta_1 - RM_q\dot{\overline{W}}_{\text{tf}}\delta_q. \tag{2.67}$$

The non-essential states propagate through the model via the disk and anti-alias filter dynamics, however, these states are easily removed by recognizing that

$$\delta_{\text{tf}} = -QB_{\text{c}}\mathcal{C}_{\text{c}}C_{\text{sm}}\delta_{\text{sm}} + \left(I - QA_{\text{tf}}\right)V_1\delta_1 + QM_q\dot{\overline{W}}_{\text{tf}}\delta_q \tag{2.68}$$

so that the reduced-order analog dynamics can be written as

$$\begin{aligned}
\dot{\delta}_{\mathrm{sm}} &= A_{\mathrm{sm}}\delta_{\mathrm{sm}} + B_{\mathrm{sm}}\delta_u \\
\dot{\delta}_1 &= RB_{\mathrm{c}}\mathcal{C}_{\mathrm{c}}C_{\mathrm{sm}}\delta_{\mathrm{sm}} + RA_{\mathrm{tf}}V_1\delta_1 - RM_q\dot{\overline{W}}_{\mathrm{tf}}\delta_q \\
\dot{\delta}_q &= \delta_{\dot{q}} \\
\dot{\delta}_{\dot{q}} &= -\nabla_{w_{\mathrm{tf}}} f(\bar{q},\dot{\bar{q}},\bar{w}_{\mathrm{tf}})QB_{\mathrm{c}}\mathcal{C}_{\mathrm{c}}C_{\mathrm{sm}}\delta_{\mathrm{sm}} + \nabla_{w_{\mathrm{tf}}} f(\bar{q},\dot{\bar{q}},\bar{w}_{\mathrm{tf}})\left(I - QA_{\mathrm{tf}}\right)V_1\delta_1 \\
&\quad + \left(\nabla_{w_{\mathrm{tf}}} f(\bar{q},\dot{\bar{q}},\bar{w}_{\mathrm{tf}})QM_q\dot{\overline{W}}_{\mathrm{tf}} + \nabla_q f(\bar{q},\dot{\bar{q}},\bar{w}_{\mathrm{tf}})\right)\delta q + \nabla_{\dot{q}} f(\bar{q},\dot{\bar{q}},\bar{w}_{\mathrm{tf}})\delta_{\dot{q}} \\
\dot{\delta}_{\mathrm{aa}} &= -B_{\mathrm{aa}}\mathcal{C}_{\mathrm{s}}C_{\mathrm{tf}}QB_{\mathrm{c}}\mathcal{C}_{\mathrm{c}}C_{\mathrm{sm}}\delta_{\mathrm{sm}} + B_{\mathrm{aa}}\mathcal{C}_{\mathrm{s}}C_{\mathrm{tf}}(I - QA_{\mathrm{tf}})V_1\delta_1 \\
&\quad + B_{\mathrm{aa}}\mathcal{C}_{\mathrm{s}}C_{\mathrm{tf}}QM_q\dot{\overline{W}}_{\mathrm{tf}}\delta_q + A_{\mathrm{aa}}\delta_{\mathrm{aa}} \\
\delta_g &= C_{\mathrm{aa}}\delta_{\mathrm{aa}},
\end{aligned} \tag{2.69}$$

where 76 states have been shed from the model in (2.61). Collecting all essential perturbation states in the state vector δ, the model is compactly expressed as the time-varying state-space realization

$$\begin{aligned}
\dot{\delta} &= A_\delta(t)\delta + B_\delta\delta_u \\
\delta_g &= C_\delta\delta.
\end{aligned} \tag{2.70}$$

An approximate time-invariant discrete-time model is characterized by solving the initial value problem posed by (2.70):

$$\delta(t) = \Theta(t,t_0)\delta(t_0) + \int_{t_0}^{t}\Theta(t,\tau)B_\delta\delta_u(\tau)d\tau,\ \ t \geq t_0, \tag{2.71}$$

where $\Theta(t,t_0)$ is the state transition matrix over the time interval $[t_0,\ t]$. While the starting time, t_0, specifies the phase of the periodic solution, it has been shown in [AM18] that its impact on the system is negligible from a frequency-domain perspective, therefore $t_0 = 0$ is assumed for the following analysis. A key feature of the discretization procedure is selecting the carrier period, $T_0 = 2\pi/\omega_0 = 1/25000\,\mathrm{s}$, to be an integer divisor of the DSP sampling period, $t_s = 1/5000\,\mathrm{s}$. The periodicity in (2.70) guarantees that

$$\Theta(2\pi\ell/\omega_0, 2\pi n/\omega_0) = \Theta^{\ell-n}(2\pi/\omega_0, 0) \quad \forall \quad \ell, n \in \mathbb{Z}. \tag{2.72}$$

By selecting the carrier frequency in the manner specified,

$$\Theta((\ell+1)t_s, \ell t_s) = \Theta^5(2\pi/\omega_0, 0) \quad \forall \quad \ell \in \mathbb{Z}. \tag{2.73}$$

When viewing the solution to the initial value problem over successive samples of the DSP,

$$\delta((\ell+1)t_s) = \Theta((\ell+1)t_s, \ell t_s)\delta(\ell t_s) + \int_{\ell t_s}^{(\ell+1)t_s} \Theta((\ell+1)t_s, \tau)B_\delta \delta_u(\tau)d\tau, \tag{2.74}$$

the input signal, δ_u, can be extracted from the integral since it is constant over the integration bounds due to the zero-order hold instituted by the DSP. Once δ_u is removed from the integrand, the integral is constant from one sample to the next because the remaining integrand is periodic with period T_0, thus, the solution to (2.70) is approximated by

$$\begin{aligned} \delta((\ell+1)t_s) &= \Phi\delta(\ell t_s) + \Gamma\delta_u(\ell t_s) \\ \delta_g &= C_\delta \delta(\ell t_s), \end{aligned} \tag{2.75}$$

where $\Phi = \Theta(t_s, 0)$ and $\Gamma = \int_0^{t_s} \Theta(t_s, \tau)B_\delta d\tau$ are numerically computed.

2.2.6 Analysis of the Linearized Model

The four-input/six-output discrete-time system in (2.75) is evaluated for $a_{\mathrm{ct}_1} = 17.7\,\mathrm{mA}$, $a_{\mathrm{ct}_2} = 1.2\,\mathrm{mA}$, and each element of $\bar{u}$ equal to $1.7\,\mathrm{V}$. The model order is 78: 10 states are associated with disk motion, 36 states characterize the six electrode transformers (the transformers supplying the center taps are not modeled), 8 states describe the four input signal smoothing filter dynamics, and 24 states are associated with the six anti-alias filters. The model in (2.75), however, contains the actuator-to-pick-off feedthrough that must be removed for controller design. A feedforward filter, denoted F and shown in Figure 2.10, is designed to cancel this feedthrough and is modeled by constraining the states associated with the disk degrees of freedom in (2.75) to be zero. Complete feedthrough cancellation is assumed, although this is unrealistic in practice. The predicted feedforward filter is nonzero only along the diagonal, where each diagonal element is identical, and contributes another 68 states to the analytical plant model, P. The discrete-time poles of P are plotted in Figure 2.11. Three unstable modes are present in the model, given in discrete time as $\lambda_1 = 1.0011$ and $\lambda_2 = \lambda_3 = 1.0026$. These instabilities correspond to continuous-time approximations of 5.60 and 13.0 rad/s, respectively, confirming that the disk dynamics evolve on a much slower time scale than the carrier signal. The geometric multiplicity of λ_2 and λ_3

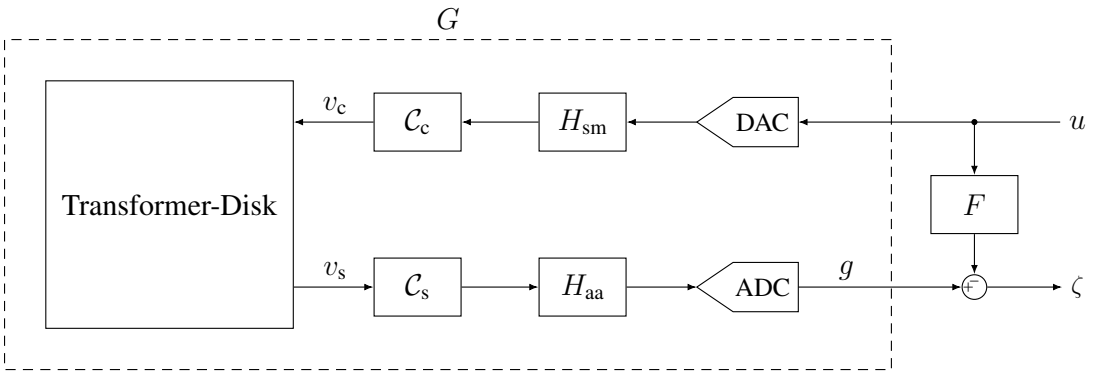

Figure 2.10: Block diagram of the plant, $P = G - F$, that includes the subsystem G, whose input is the DSP-generated signal u and output is the sampled signal g, as well as the digital feedforward filter, F.

is two. Two pairs of lightly damped, stable resonant modes lie just inside of the unit circle with natural frequencies equal to 0.98 rad/s.

The pole directions are useful for understanding the instabilities in terms of the disk's degrees of freedom –see [SP05], for example, for definitions of input and output pole directions. The input pole directions for $\{\lambda_1, \lambda_2, \lambda_3\}$ are approximately

$$\begin{aligned} v_{1_i} &= \begin{bmatrix} \frac{1}{2} & \frac{1}{2} & \frac{1}{2} & \frac{1}{2} \end{bmatrix}^T \\ v_{2_i} &= \begin{bmatrix} 0 & \frac{1}{\sqrt{2}} & 0 & -\frac{1}{\sqrt{2}} \end{bmatrix}^T \\ v_{3_i} &= \begin{bmatrix} -\frac{1}{\sqrt{2}} & 0 & \frac{1}{\sqrt{2}} & 0 \end{bmatrix}^T, \end{aligned} \tag{2.76}$$

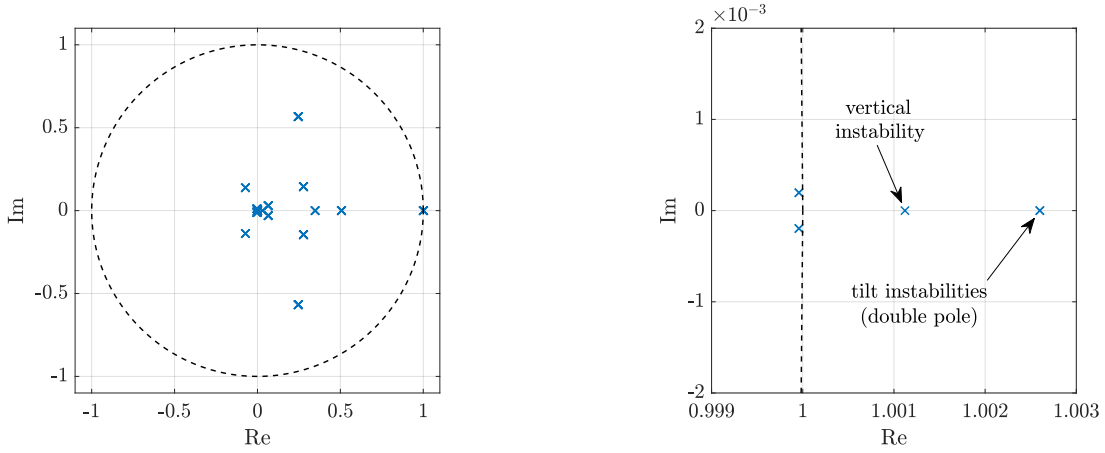

Figure 2.11: Discrete-time poles of the analytical plant model. Left: all poles; right: zoomed-in plot of the unstable poles.

respectively, however, because of the geometric multiplicity of λ_2 and λ_3, any two linearly independent vectors in the space spanned by v_{2_i} and v_{3_i} are input pole directions. Infinitesimal deviations from the reported directions exist due to the imbalances present in the non-idealized transformer model. The input directions reveal how the electrostatic actuators couple to the unstable modes. An input of the form $u = v_{1_\text{i}}$ corresponds to applying a net vertical force on the disk, meanwhile inputs represented by $u = v_{2_\text{i}}$ and $u = v_{3_\text{i}}$ correspond to moments about the N_1- and N_2-axes, respectively. Similarly, the output pole directions associated with $\{\lambda_1, \lambda_2, \lambda_3\}$, respectively, are given by

$$\begin{aligned} v_{1_\text{o}} &= \begin{bmatrix} \frac{1}{2} & \frac{1}{2} & \frac{1}{2} & \frac{1}{2} & 0 & 0 \end{bmatrix}^T \\ v_{2_\text{o}} &= \begin{bmatrix} 0 & \frac{1}{\sqrt{2}} & 0 & -\frac{1}{\sqrt{2}} & 0 & -\epsilon \end{bmatrix}^T \\ v_{3_\text{o}} &= \begin{bmatrix} -\frac{1}{\sqrt{2}} & 0 & \frac{1}{\sqrt{2}} & 0 & \epsilon & 0 \end{bmatrix}^T, \end{aligned} \tag{2.77}$$

where $\epsilon \ll 1$. The output pole directions provide a useful interpretation of the instabilities in terms of the measurements. Recall that the measurements ζ_k, $k = 1, 2, 3, 4$, are related to the disk's vertical position local to each primary electrode pair, thus, they provide insight into the disk's vertical and angular positions; meanwhile, ζ_5 and ζ_6, are purely in-plane measurements. With this knowledge, the unstable pole λ_1 represents a pure vertical translational instability, λ_2 corresponds to the disk rotating about the N_1-axis coupled with translational motion in

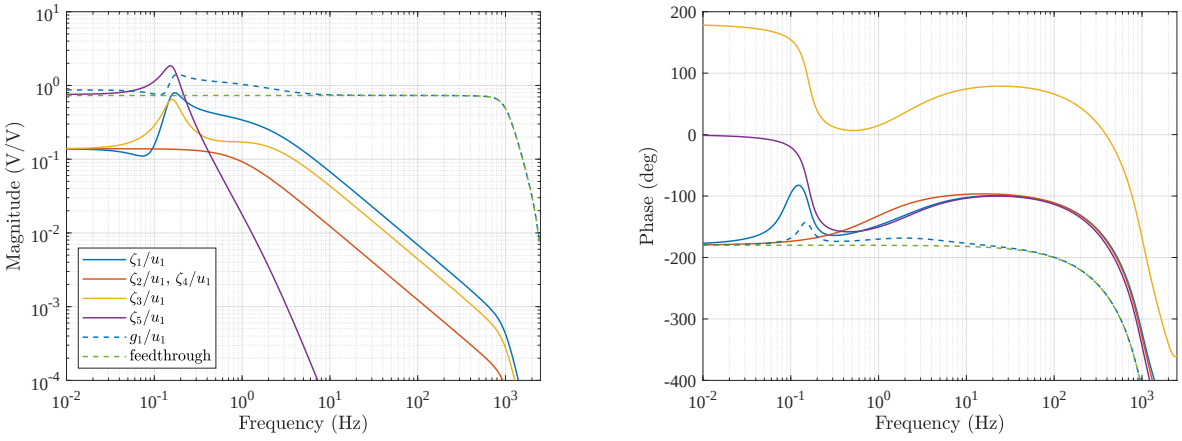

Figure 2.12: Analytical frequency responses of the feedthrough-compensated plant outputs to input channel u_1. The uncompensated output, g_1, and feedthrough itself are also shown. Feedthrough is only predicted in the diagonal channels.

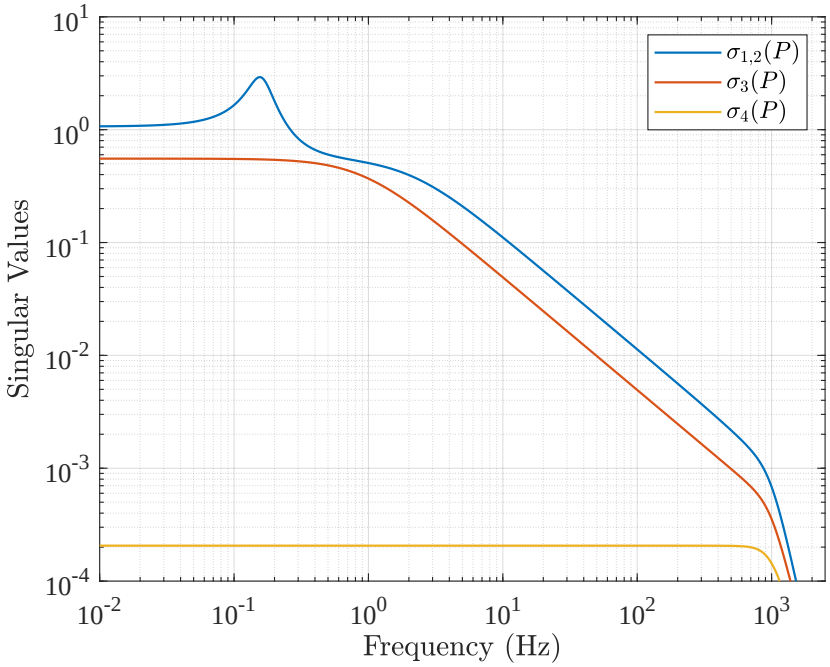

Figure 2.13: Singular values, σ_j, $j = 1, 2, 3, 4$, of the analytical plant model (feedthrough removed). Only three traces appear because $\sigma_1 = \sigma_2$.

the N_2-direction, and λ_3 is associated with an angular rotation about the N_2-axis coupled with translational motion in the N_1-direction. Recall that the angular and lateral degrees of freedom were inherently coupled in the disk's equations of motion. The correspondence between $\{\lambda_1, \lambda_2, \lambda_3\}$ and these degrees of freedom is confirmed by analyzing the eigenvectors associated with each unstable mode. The λ_1 and $\{\lambda_2, \lambda_3\}$ instabilities are appropriately named the "vertical" and "tilt" instabilities, respectively.

The discrete-time frequency response from u to the feedthrough-compensated signal, ζ, is computed and is plotted in Figure 2.12 for input u_1, where it should be noted that $\zeta_6/u_1 = 0$. The remaining input/output channels are easily identified from the system's symmetry, i.e., $\zeta_1/u_1 = \zeta_2/u_2$, $\zeta_1/u_2 = \zeta_2/u_1$, $\zeta_5/u_1 = \zeta_6/u_2$, etc. The feedthrough is also included in Figure 2.12 and indicates that the magnitude of the feedthrough exceeds the motional gain of the plant. The singular values of the plant are provided in Figure 2.13, where only three traces are shown because $\sigma_1 = \sigma_2$. The plot reveals a "low gain" (σ_4) with

right and left singular vectors that are independent of frequency and given by

$$\begin{aligned} v_{4_{\mathrm{r}}} &= \begin{bmatrix} \frac{1}{2} & -\frac{1}{2} & \frac{1}{2} & -\frac{1}{2} \end{bmatrix}^T \\ v_{4_{\mathrm{l}}} &= \begin{bmatrix} \frac{1}{2} & -\frac{1}{2} & \frac{1}{2} & -\frac{1}{2} & 0 & 0 \end{bmatrix}^T, \end{aligned} \tag{2.78}$$

respectively. The remaining right singular vectors correspond to two independent moments and a vertical force acting on the disk. The remaining left singular vectors include $v_{1_{\mathrm{o}}}$ and four vectors that coincide with two orthogonal rotations of the disk coupled to two independent lateral translations. The magnitudes of the rotations relative to the lateral translations vary with frequency because the measurements are dominated by in-plane motion at low frequencies, however, this motion is negligible beyond 1 Hz (see ζ_5/u_1 in Figure 2.12).

CHAPTER 3

Previous Results

Stabilization of the system described in Chapter 2 has been reported in [AM21]. In that work, classical loop-shaping techniques are used to design single-input/single-output feedback controllers around each nonzero channel of a decoupled plant. The plant decomposition,

$$\tilde{P} = \mathcal{D}_{\mathrm{o}}^{T} P \mathcal{D}_{\mathrm{i}}, \tag{3.1}$$

utilizes transformations based on the input and output directions associated with the plant's unstable poles, $v_{l_{\mathrm{i}}}$ and $v_{l_{\mathrm{o}}}$, $l = 1, 2, 3$, respectively, where

$$\mathcal{D}_{\mathrm{i}} = \begin{bmatrix} v_{1_{\mathrm{i}}} & v_{2_{\mathrm{i}}} & v_{3_{\mathrm{i}}} \end{bmatrix}, \qquad \mathcal{D}_{\mathrm{o}} = \begin{bmatrix} v_{1_{\mathrm{o}}} & v_{2_{\mathrm{o}}} & v_{3_{\mathrm{o}}} & v_x & v_y \end{bmatrix} \tag{3.2}$$

are the input and output decoupling matrices, respectively. The input and output directions associated with the unstable poles correspond to the vertical and rotational modes of the system and the remaining output decoupling vectors,

$$\begin{aligned} v_x &= \begin{bmatrix} 0 & 0 & 0 & 0 & 1 & 0 \end{bmatrix}^T \\ v_y &= \begin{bmatrix} 0 & 0 & 0 & 0 & 0 & 1 \end{bmatrix}^T, \end{aligned} \tag{3.3}$$

provide measurements of the lateral degrees of freedom in the inertial coordinate frame. The low gain input direction of the plant, $v_{4_{\mathrm{r}}}$, essentially exerts no net forces nor moments on the disk and is omitted from the transformation –see Section 2.2.6. Similarly, rigid body motion of the disk cannot produce measurements in the low gain output direction, $v_{4_{\mathrm{l}}}$: if included in the decoupling transformation, the measurement corresponding to this channel is virtually zero. Hence, this vector is also omitted from the transformation to yield a

three-input/five-output model of the form

$$\tilde{P} = \begin{bmatrix} \star & 0 & 0 \\ 0 & \star & 0 \\ 0 & 0 & \star \\ 0 & 0 & \star \\ 0 & \star & 0 \end{bmatrix}, \tag{3.4}$$

where the elements labeled by a $\star$ are nonzero. The transformation $\mathcal{D}_{\mathrm{o}}^{T} P \mathcal{D}_{\mathrm{i}}$ correlates the inputs and outputs of $\tilde{P}$ with the disk's controllable and observable degrees of freedom, respectively.

In [AM21], the vertical and tilt degrees of freedom are stabilized by an inner control loop, meanwhile, an outer loop regulates the lateral modes. In these coordinates, however, the inner loop plant is not strongly stabilizable, necessitating unstable feedback controllers in these channels for disk suspension [YBL74]. The system is incapable of maintaining nonzero angular rotations of the disk since the DC loop gain corresponding to the pitch and roll feedback loops is zero. The feedforward filter implemented in practice fit an FIR filter to the electrical response to broadband random inputs with the disk resting at its bottom position. Inputs were independently applied at each input channel in separate experiments where the amplitude of the input signals was not large enough to actuate the disk, so any electrical response was the direct result of feedthrough from u to g. With the disk suspended, empirical measurements of the system were captured that align quite well with the model in (2.75), nevertheless, the work in [AM21] presented a number of challenges to consistently suspending the disk that must be addressed prior to miniaturization to the scale of microresonators.

The first challenge made apparent in that work is the implementation of unstable controllers due to rapid windup of the state variable and subsequent saturation of the control command upon startup. Stabilization is inconsistent and unreliable: the disk must be lifted to just the right position for the controller to "catch it". Saturation limits are imposed upon the state variable, however, the bounds must be fine-tuned such that nonzero error signals can provide enough energy to relieve the state from saturation while simultaneously

providing large enough controller gain for stabilization. A more systematic and consistent approach to suspend the disk is desired, motivating the next challenge of improving closed-loop robustness margins. Cross-channel coupling not predicted by the model is indicated in [AM21] due to inherent differences in the transduction gains between channels that ruin the symmetry of the system such that the coordinate transformation mixes the variables. Additional controller synthesis techniques that provide robust stability against such uncertainties present in the plant model should be investigated, as these uncertainties play a role in the unreliability of the previously designed controller. On the other hand, improved robustness margins are ineffective without an accurate model of the plant. Accurate empirical models of the plant based on spectral analysis of long data records (the lightly damped resonances occur below 0.2 Hz) are possible, however, more advanced multivariable control techniques rely on parametric models of the system. Thus, obtaining an accurate parametric model of the plant from closed-loop data presents another challenge. Additionally, the feedforward filter is only capable of rejecting about 90% of the feedthrough coupling within the system. Above 10 Hz, residual feedthrough dominates the plant response and introduces significant phase lag, effectively constraining the loop bandwidth.

In addition to the modeling paradigm developed in Chapter 2, this dissertation addresses the final three challenges laid out in the previous paragraph. Furthermore, the modeling framework is expanded to additional electrode-disk configurations. A two-pronged approach is investigated: first, parametric identification and robust stability to coprime factor perturbations of the system are examined for a smaller disk that reduces the number of actively controlled degrees of freedom to three; second, the challenges addressed with the simpler system are applied to a system redesign that eliminates feedthrough by separating the control and sense electronics. Chapter 4 discusses the design of a robustly stabilizing multivariable controller and iteration of the control design to improve robust performance using a novel parametric identification technique. Furthermore, the unstable pole input and output directions of the parametric fit are used to identify differences in transduction gains. The simpler system is strongly stabilizable, even when decoupled, so the implementation of unstable controllers is not addressed. Part II investigates the modeling, fabrication, and control design

of the updated system that incorporates segregated control and sense electrodes. Both disks –the one discussed in Chapter 2 and the smaller one used in Chapter 4 –are studied, again using a controller synthesis procedure designed to maximize robustness margins to perturbations of the plant's normalized coprime factors. The control algorithm produces an unstable controller for the larger disk, however, an additional, albeit less robust, stable controller is designed for the four-input/six-output, non-decoupled plant since this system is strongly stabilizable.

CHAPTER 4

The Three-Degree-of-Freedom Disk

A smaller, 37 mm radius disk is etched from a 400 μm thick double side polished silicon wafer and coated with conductive films of 5 nm titanium and 1μm aluminum to create an equipotential body. The radius of this disk matches the outer radii of the primary electrodes so that fringe field forces passively stabilize the disk's lateral position. The electrodes and electronics are identical to those discussed previously, however, all electronics corresponding to the outer ring of electrodes, i.e., $i = 2$, have been disconnected and powered down. Continued use of the electrodes for both actuation and sensing sustains the feedthrough dilemma. The center tap amplitude to the primary electrodes, carrier frequency, and modulation and demodulation phases remain unchanged and the schematic shown in Figure 2.5 of a single input/output channel of the analog subsystem of the plant for the larger disk is valid for the smaller disk as well. The same DSP interfaces between the transformer electronics and digital filters at a 5 kHz sample rate. Digital feedthrough compensation is still considered internal to the plant. With the lateral electrodes disconnected, the plant is a four-input/four-output system.

New silicon spacers are etched from the same wafer as the smaller disk so that the nominal air gaps of 114 μm are maintained by the aluminum shims used prior. The rigid body motion of the disk is described by three degrees of freedom –vertical position, pitch, and roll. As before, the electrode arrangement is incapable of measuring yaw rotation and provides no means of spinning the disk about the vertical axis. Lateral motion, however, is essentially unobservable with the updated electrode-disk configuration. The system remains under development for testing of MEMS gyroscopic resonators and it should be noted that when the suspension system is scaled down, the outer radius of the electrodes will be designed to

match the resonator stem radius so that fringe field forces constrain lateral motion of the device's center of mass.

4.1 Analytical Model

Generating an analytical model of the system with the smaller disk follows the same procedure laid out in Chapter 2. The disk mass, m, and transverse- and spin-axis moments of inertia, J_t and J_s, respectively, are evaluated from the disk radius and thickness. A free body diagram of this disk is pictured in Figure 4.1. Gravitational and viscous damping effects remain present and the electrostatic forces continue to be modeled as point forces normal to the disk. With the lateral electrodes disconnected, however, only four top and four bottom electrostatic point forces act on the disk. Although the lateral degrees of freedom are immeasurable, they are included in the model out of consideration of in-plane forces due to electrical field fringing. These terms are assumed to be proportional to translations in the N_1- and N_2-directions so that the forces act as virtual springs. The "spring" stiffnesses, $\{k_x, k_y\}$, are selected so that the lateral modes have a 2 Hz resonance. Lateral fringing forces were ignored with the larger disk since these terms were negligible for mild deviations from the nominal setpoint: for small perturbations from the inertial origin, the net lateral forces acting on the disk from the electrical fringe fields effectively "cancel out" since the in-plane component of the fringing forces from the electrodes pull outwards on the disk sidewall in all directions. Significant lateral deviations of the larger disk results in fringing forces dominated by a lateral electrode on one side of the disk and primary electrode on the opposing side, creating an imbalance in the in-plane forces acting on the disk since the primary electrodes operate at larger voltage amplitudes and have larger area. Thus, fringing forces provided a barrier several millimeters larger in diameter than the disk that kept the disk from shooting out horizontally but inside of the barrier the disk was free to move laterally. In contrast, the distributed fringe field forces oppose any in-plane motion of the smaller disk since any lateral displacement results in stronger pulling forces on the disk sidewall that lies within the outer radii of the electrodes. While the lateral restoring forces are exerted on the disk

sidewall, the disk is constrained to very small angular rotations and is assumed thin so that the spring forces are modeled at the disk's center of mass.

Collecting the forces and following the procedure laid out in Chapter 2, the motion of the smaller disk is governed by

$$\begin{aligned}
m\ddot{x} &= -c_x\dot{x} - k_x x + \varphi \sum_{i,j} F_{\mathrm{n}_{ij}} \\
m\ddot{y} &= -c_y\dot{y} - k_y y - \theta \sum_{i,j} F_{\mathrm{n}_{ij}} \\
m\ddot{z} &= -c_z\dot{z} - ma_{\mathrm{g}} + \sum_{i,j} F_{\mathrm{n}_{ij}} \qquad\qquad i = 1 \\
J_{\mathrm{t}}\ddot{\theta} &= -c_\theta\dot{\theta} + 2\left(J_{\mathrm{t}} - J_{\mathrm{s}}\right)\varphi\dot{\theta}\dot{\varphi} + \sum_{i,j}\left(\bar{y}_{ij} - y\right) F_{\mathrm{n}_{ij}} \qquad\qquad j = 1,2,3,4 \\
J_{\mathrm{t}}\ddot{\varphi} &= -c_\varphi\dot{\varphi} + \left(J_{\mathrm{s}} - J_{\mathrm{t}}\right)\varphi\dot{\theta}^2 + \sum_{i,j}\left(x - \bar{x}_{ij}\right) F_{\mathrm{n}_{ij}}.
\end{aligned} \tag{4.1}$$

The most glaring difference between the analytical models for the two differently sized disks is the presence of the $k_x x$ and $k_y y$ fringing terms in the lateral degree of freedom equations for the smaller disk. The system of equations in (4.1) is concisely written as

$$\frac{d}{dt}\begin{bmatrix} q \\ \dot{q} \end{bmatrix} = \begin{bmatrix} \dot{q} \\ f(q, \dot{q}, w_{\mathrm{tf}}) \end{bmatrix}. \tag{4.2}$$

The remaining dynamics of the model remain nearly identical to those of the larger disk and are briefly reviewed. The only electronic changes stem from the fact that fewer transformers, analog demodulators, and anti-alias filters are necessary since the measurements associated with the lateral electrodes have been removed. The states and pick-offs corresponding to the disconnected electronics are eliminated from (2.55) so that

$$w_{\mathrm{tf}} = \begin{bmatrix} w_{\mathrm{tf}_{11}} \\ \vdots \\ w_{\mathrm{tf}_{14}} \end{bmatrix}, \quad v_{\mathrm{c}} = \begin{bmatrix} v_{\mathrm{c}_1} \\ \vdots \\ v_{\mathrm{c}_4} \end{bmatrix}, \quad v_{\mathrm{s}} = \begin{bmatrix} v_{\mathrm{s}_1} \\ \vdots \\ v_{\mathrm{s}_4} \end{bmatrix}$$

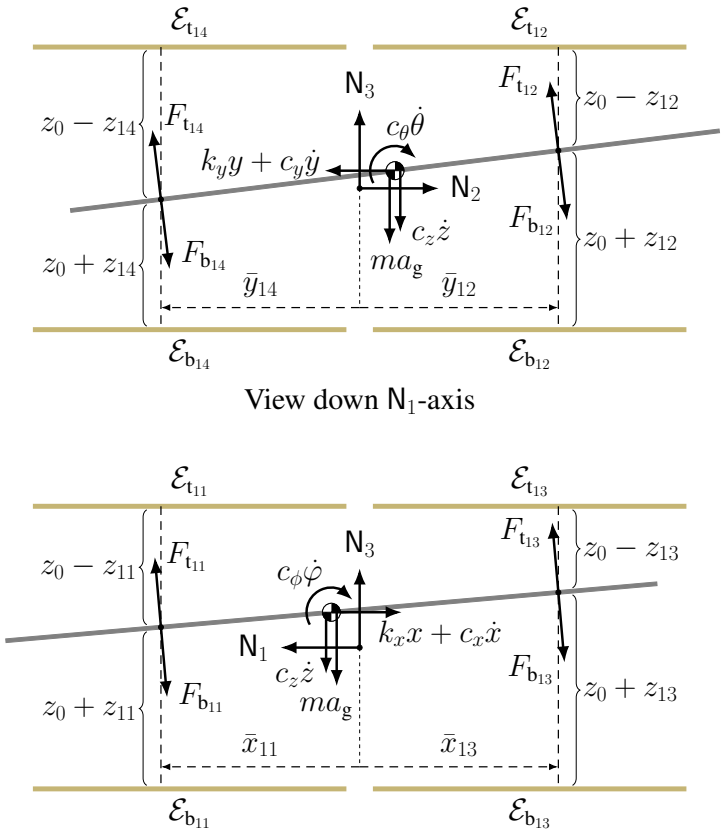

Figure 4.1: Free body diagram of the smaller disk (not to scale). The disk diameter is equal to the electrode diameter. The fringe field creates in-plane restoring forces with equivalent spring constants $\{k_x, k_y\}$.

and the state-space matrices are

$$M_{\text{tf}}(q) = \text{diag}\left(M_{\text{tf}_{11}}, M_{\text{tf}_{12}}, M_{\text{tf}_{13}}, M_{\text{tf}_{14}}\right) \in \mathbb{R}^{76\times 76}$$

$$A_{\text{tf}} = \text{diag}\left(A_{\text{tf}_1}, A_{\text{tf}_1}, A_{\text{tf}_1}, A_{\text{tf}_1}\right) \in \mathbb{R}^{76\times 76}$$

$$C_{\text{tf}} = \text{diag}\left(C_{\text{tf}_1}, C_{\text{tf}_1}, C_{\text{tf}_1}, C_{\text{tf}_1}\right) \in \mathbb{R}^{4\times 76}$$

$$B_{\text{ct}} = \begin{bmatrix} B_{\text{ct}_1} \\ -B_{\text{ct}_1} \\ B_{\text{ct}_1} \\ -B_{\text{ct}_1} \end{bmatrix} \in \mathbb{R}^{76\times 1}, \quad B_{\text{c}} = \begin{bmatrix} B_v & 0 & 0 & 0 \\ 0 & B_v & 0 & 0 \\ 0 & 0 & B_v & 0 \\ 0 & 0 & 0 & B_v \end{bmatrix} \in \mathbb{R}^{76\times 4}.$$

Similarly, the state vector w_{aa} and block diagonal matrices represented by $(A_{\text{aa}}, B_{\text{aa}}, C_{\text{aa}})$ and $\mathcal{C}_{\text{s}}$ are truncated from those in (2.57) to only contain the electronics corresponding to

the primary electrodes. The model order of the truncated anti-alias filtering electronics is 16. The smoothing filter dynamics remain unchanged from (2.56) and the analog subsystem is collectively governed by

$$\begin{aligned}
\dot{w}_{\mathrm{sm}} &= A_{\mathrm{sm}} w_{\mathrm{sm}} + B_{\mathrm{sm}} u \\
M(q)\dot{w}_{\mathrm{tf}} &= B_{\mathrm{c}} \mathcal{C}_{\mathrm{c}} C_{\mathrm{sm}} w_{\mathrm{sm}} + A_{\mathrm{tf}} w_{\mathrm{tf}} + B_{\mathrm{ct}} i_{\mathrm{ct}} \\
\frac{d}{dt} \begin{bmatrix} q \\ \dot{q} \end{bmatrix} &= \begin{bmatrix} \dot{q} \\ f(q, \dot{q}, w_{\mathrm{tf}}) \end{bmatrix} \\
\dot{w}_{\mathrm{aa}} &= B_{\mathrm{aa}} \mathcal{C}_{\mathrm{s}} C_{\mathrm{tf}} w_{\mathrm{tf}} + A_{\mathrm{aa}} w_{\mathrm{aa}} \\
g &= C_{\mathrm{aa}} w_{\mathrm{aa}},
\end{aligned} \tag{4.3}$$

where $g = [g_1 \; g_2 \; g_3 \; g_4]^T$. Following the procedure outlined in Section 2.2.5, small signal linearization about the nominal operating point, $\bar{q} = 0$, $\dot{\bar{q}} = 0$, is used to approximate a linear time-periodic realization,

$$\begin{aligned}
\dot{\delta} &= A_\delta(t)\delta + B_\delta \delta_u \\
\delta_g &= C_\delta \delta,
\end{aligned} \tag{4.4}$$

where δ contains the perturbation states of the linear variational equations and δ_u and δ_g are the perturbed input and electronic pick-off, respectively. Using the fact that the carrier period is an integer divisor of the DSP sampling period, the solution to an initial value problem posed by (4.4) can be effectively discretized to yield the time-invariant discrete-time model

$$\begin{aligned}
\delta((\ell+1)t_s) &= \Phi\delta(\ell t_s) + \Gamma\delta_u(\ell t_s) \\
\delta_g &= C_\delta \delta(\ell t_s)
\end{aligned} \tag{4.5}$$

for sample index integer ℓ.

The four-input/four-output frequency response of the discrete-time system (4.5) is computed with $a_{\mathrm{ct}} = 17.7\,\mathrm{mA}$ and each element of $\bar{u}$ equal to $1.41\,\mathrm{V}$. The DC input signal required to suspend the disk by counteracting the gravitational force is lower than that required for the larger disk due to the reduced disk mass. The model order is 58: there

are 24 states associated with the four transformers used for transduction (transformers supplying the center tap currents are not modeled), 10 states associated with the disk, and 24 states associated with the smoothing and anti-alias filters. The model (4.5) contains the actuator-to-pick-off feedthrough that must be removed for controller design and the feedforward filter, denoted F in Figure 2.10, is implemented to "cancel" this feedthrough. The signal used for feedback is denoted $\zeta = [\zeta_1\ \zeta_2\ \zeta_3\ \zeta_4]^T$. The response of ζ to u_1 is shown in Figure 4.2. The remaining input/output channels can be determined from the system's symmetry, i.e., the plant frequency response is symmetric and all diagonal channels are identical. In the model, the feedthrough is only present in the diagonal entries and is determined by constraining the states associated with the disk degrees of freedom in (4.5) to be zero. The graphs assume complete feedthrough cancellation, although in practice this is not the case (see Section 4.3). The feedthrough is also shown in Figure 4.2 and indicates that the magnitude of the feedthrough exceeds the motional gain of the plant. The lateral modes are barely evident in a neighborhood of 2 Hz. These modes are stable and weakly coupled to the pick-offs since the capacitive transducers are insensitive to small perturbations to the disk's lateral position. Removing the in-plane degrees of freedom yields a nearly identical model: the disappearance of the 2 Hz lateral modes is the only difference.

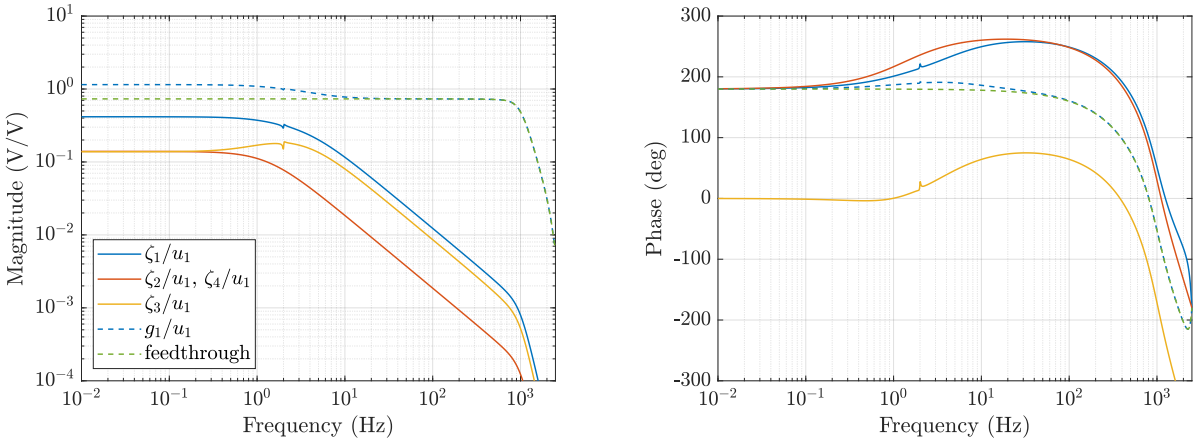

Figure 4.2: Analytical frequency responses of the four compensated plant outputs to input channel u_1. The uncompensated signal g_1 and the feedthrough are shown by the dashed traces.

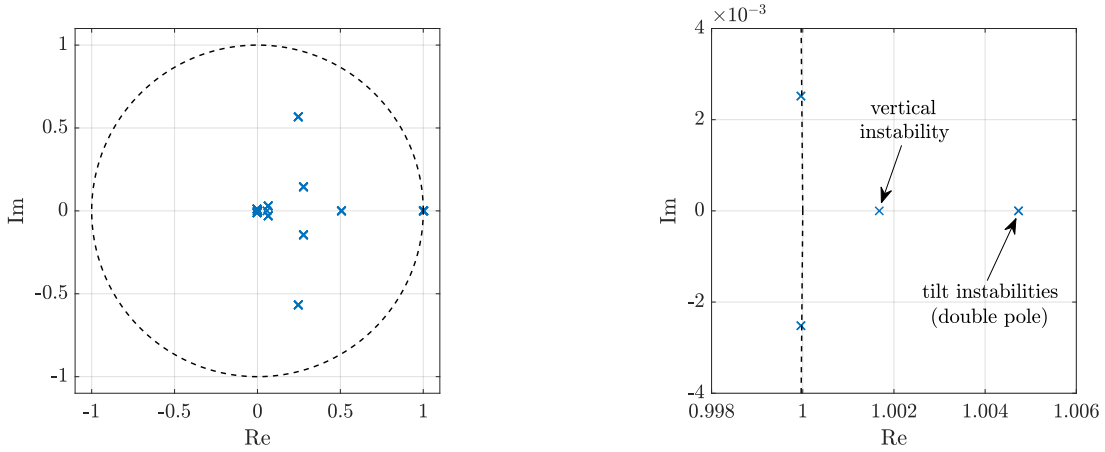

Figure 4.3: Left: Discrete-time poles of the analytical plant model. Right: Zoomed-in view of the three instabilities present in the model.

Despite the high model order, the plant frequency response has a simple low-pass characteristic. There are, however, three unstable eigenvalues given in discrete-time as $\lambda_1 = 1.0017$, $\lambda_2 = \lambda_3 = 1.0047$ (corresponding to 8.38 and 23.6 rad/s, respectively, in continuous-time). The plant poles are plotted in Figure 4.3. The geometric multiplicity of λ_2 and λ_3 is two. Both the input *and* output directions associated with $\{\lambda_1, \lambda_2, \lambda_3\}$, respectively, are given by

$$\begin{aligned} v_1 &= \begin{bmatrix} \frac{1}{2} & \frac{1}{2} & \frac{1}{2} & \frac{1}{2} \end{bmatrix}^T \\ v_2 &= \begin{bmatrix} 0 & \frac{1}{\sqrt{2}} & 0 & -\frac{1}{\sqrt{2}} \end{bmatrix}^T \\ v_3 &= \begin{bmatrix} -\frac{1}{\sqrt{2}} & 0 & \frac{1}{\sqrt{2}} & 0 \end{bmatrix}^T . \end{aligned} \tag{4.6}$$

Due to the geometric multiplicity of λ_2 and λ_3, though, any two linearly independent vectors in the space spanned by v_2 and v_3 are also input and output directions. The output directions are informative for understanding the instabilities in terms of the measurements: λ_1 corresponds to a translational instability in which the disk is moving in the N_3-direction with no rotation (see Figure 4.1) –this is confirmed by analysis of the eigenvector associated with λ_1; similarly, λ_2 corresponds to the disk rotating about N_1 and λ_3 corresponds to the disk rotating about N_2. Accordingly, λ_1 is designated the "vertical instability" whereas λ_2 and λ_3 are the "tilt instabilities." The input directions also indicate how the four electrostatic actuators couple to each unstable mode: v_1 corresponds to applying a vertical force to the disk with no moments, whereas v_2 and v_3 correspond to pure moments with no net vertical

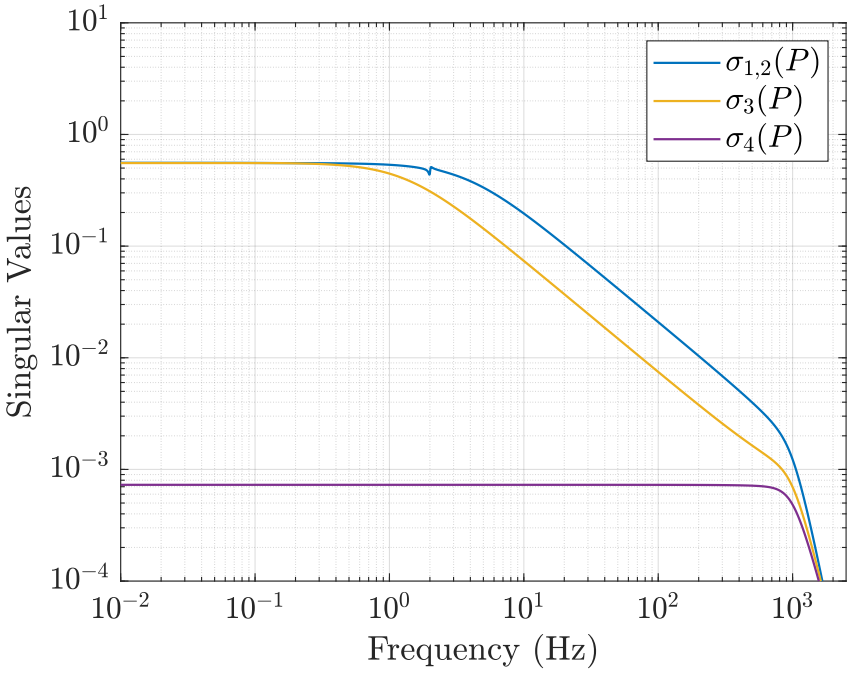

Figure 4.4: Singular values of the analytical plant. Only three traces appear since $\sigma_1 = \sigma_2$.

force.

The plant singular values in Figure 4.4 reveal a "low gain" with both input and output singular vectors independent of frequency and equal to

$$v_4 = \begin{bmatrix} \frac{1}{2} & -\frac{1}{2} & \frac{1}{2} & -\frac{1}{2} \end{bmatrix}^T. \tag{4.7}$$

This is not surprising because the disk's pose is specified by its vertical position, pitch, and roll. Thus, a vertical force and two moments in the disk plane are necessary to hold a given pose. Four independent electrostatic forces applied by the electrodes exceed this minimal requirement (recall that the choice of four electrode pairs was motivated by a hardware-based solution to maintain the disk at ground potential). The low gain input singular vector gives the combination of electrostatic forces that yield essentially zero net vertical force and zero net moments. The output singular vector yields capacitive gap measurement voltages that cannot be produced by a rigid body pose of the disk.

The orthogonal transformation $[v_1\ v_2\ v_3\ v_4]^T$ can be applied to the four capacitive gap measurement potentials to produce four new potentials proportional to the states $\{\delta_z, \delta_\theta, \delta_\varphi\}$.

The last element in the new potentials is essentially zero and insensitive to changes in the disk pose. Proportionality constants, or scale factors, are determined by applying independent perturbations to δ_z, δ_θ, and δ_φ and noting the corresponding change in the new potentials. The estimated scale factors are $14.1\,\mu$m/V and $0.887\,$mrad/V to convert the new potentials into vertical and rotational positions with units of μm and mrad, respectively.

4.2 Robust Stabilization of the Linearization

Deviations between the model and physical system can be attributed to many sources: misalignment of paired electrodes, non-parallel plates, differences in transformer parameters, inexact cancellation of the actuator-to-pick-off feedthrough, damping errors, and so forth. These will not only change the transduction gains but also shift the unstable eigenvalues. In view of this, a conservative control design approach is adopted in which robust stabilization is the initial objective. Once the disk is stabilized, identification of the plant dynamics from closed-loop measurements will yield an accurate empirical model of the plant and provide an opportunity for a second control design iteration.

A controller, denoted K_s in Figure 4.5, is synthesized to maximize the closed-loop stability margin with respect to perturbations of a normalized left coprime factorization of the shaped plant, $P_s = M^{-1}N$ –see [Vid85, Fra87, ZDG96, SP05]. The shaped plant is a filtered version

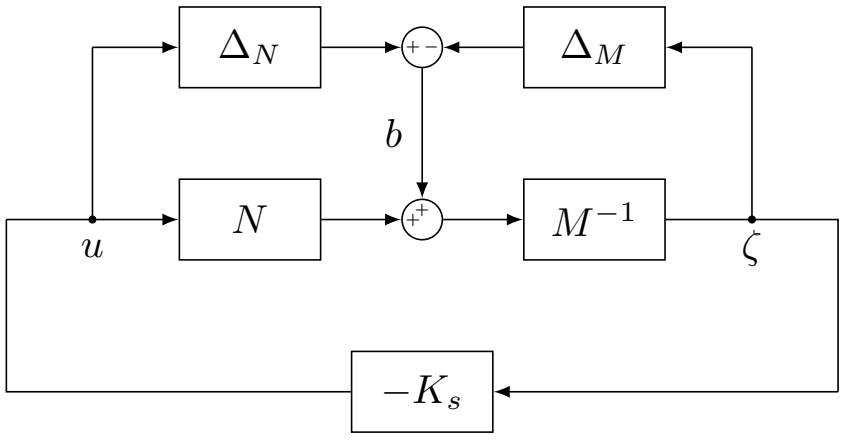

Figure 4.5: Controller, K_s, in feedback with a left coprime factorization of the shaped plant.

of the model in (4.5) and is discussed below. The coprime rational functions M and N are both stable, implying that N contains all right half-plane zeros of P_s and the unstable poles of P_s appear as zeros of M. Coprimeness indicates that there are no common right half-plane zeros in M and N that would result in unstable pole-zero cancellations of $M^{-1}N$. Mathematically, this implies that there exist stable matrices U and V such that M and N satisfy the Bezout identity

$$NU + MV = I. \tag{4.8}$$

Coprime factorizations are not unique, however, a normalized left coprime factorization is co-inner, i.e., it satisfies the frequency response identity

$$N(\jmath\omega)N^*(\jmath\omega) + M(\jmath\omega)M^*(\jmath\omega) = I, \tag{4.9}$$

and is unique to within a left multiplication by a unitary matrix. A minimal state-space realization for a normalized left coprime factorization of the shaped plant is given by

$$\begin{bmatrix} N & M \end{bmatrix} = \left[\begin{array}{c|cc} A + HC & B + HD & H \\ \hline R^{-1/2}C & R^{-1/2}D & R^{-1/2} \end{array}\right], \tag{4.10}$$

where (A, B, C, D) is the state-space realization of the shaped plant, $R = I + DD^T$,

$$H = -\left(BD^T + ZC^T\right)R^{-1},$$

Z is the unique positive definite solution to the algebraic Riccati equation

$$\left(A - BS^{-1}D^TC\right)Z + Z\left(A - BS^{-1}D^TC\right)^T - ZC^TR^{-1}CZ + BS^{-1}B^T = 0, \tag{4.11}$$

and $S = I + D^TD$. The reader is referred to [Vid88] for the realization for a normalized right coprime factorization.

The perturbed plant is given by $(M + \Delta_M)^{-1}(N + \Delta_N)$ for the complex perturbations $\{\Delta_M,\ \Delta_N\}$ –see Figure 4.5. This highly generalized unstructured uncertainty description characterizes low frequency parameter errors, neglected high frequency dynamics, and uncertain (quantities of) right half-plane poles and zeros and is especially useful when

a priori information regarding sources of uncertainty in a system is unknown. The controller that internally stabilizes the closed-loop system over the largest set of perturbations ($\|[\Delta_N \ \Delta_M]\|_\infty < 1/\gamma$) is found by solving

$$\gamma = \inf_{K_s} \left\| \begin{bmatrix} K_s \\ I \end{bmatrix} (I + P_s K_s)^{-1} M^{-1} \right\|_\infty \tag{4.12}$$

over the set of stabilizing controllers. The solution to this problem was solved in [GM89] and is quickly reviewed (see [MG90, ZDG96, SP05, ZDG96] also). The maximum achievable stability margin of the closed-loop system shown in Figure 4.5 is given by

$$\gamma_{\min} = \sqrt{1 + \rho(XZ)} \tag{4.13}$$

where $\rho(\cdot)$ is the spectral radius of the matrix argument and X is the unique positive definite solution to the algebraic Riccati equation

$$\left(A - BS^{-1}D^T C\right)^T X + X\left(A - BS^{-1}D^T C\right) - XBS^{-1}B^T X + C^T R^{-1} C = 0. \tag{4.14}$$

The controller that guarantees (4.12) for the suboptimal problem, $\gamma > \gamma_{\min}$, is given as

$$K_s = \left[\begin{array}{c|c} A + BF + \gamma^2 L^{-T} Z C^T (C + DF) & -\gamma^2 L^{-T} Z C^T \\ \hline B^T C & D^T \end{array}\right], \tag{4.15}$$

where

$$F = -S^{-1}\left(D^T C + B^T X\right)$$
$$L = \left(1 - \gamma^2\right) I + XZ.$$

While the control synthesis technique outlined above optimizes robust stability, performance requirements of the system cannot be specified. Improved performance can be achieved, however, by pre- and post-compensating the plant to shape the open-loop singular values prior to implementing the controller algorithm. The shaped plant, P_s, that is used for control design is given by

$$P_s = W_2 P W_1, \tag{4.16}$$

where W_1 and W_2 are the pre- and post-compensation weights shown in Figure 4.6. For the disk suspension problem, the shaping is simply a scaling of the open-loop plant, $P_s = 4P$, i.e., $W_1 = 4$ and $W_2 = I$, so that the three largest singular values of the frequency response cross over between 1 and 10 Hz –see Figure 4.8. For the shaped plant, $\gamma_{\min} \approx 1.9$.

Using the algorithm proposed in [MG90] requires a continuous-time representation of the plant, so the bilinear transform is used to map the discrete-time model in (4.5) to the continuous-time domain. The synthesized controller is stable for the suboptimal problem $\gamma = 1.1 \times \gamma_{\min}$, however, the controller is of equal dimension to the system model, which contains 106 states (feedthrough cancellation contributes an additional 48 states to the plant model). Implementing such a controller is not feasible with the DSP, so a model reduction by balanced truncation is performed. Inspection of the controller's Hankel singular values suggests that the controller dimension can be reasonably approximated by a 3-state system, denoted K_r. The error in the reduced-order controller is subject to the bound

$$\|K_s - K_r\|_\infty \leq 2(\sigma_{r+1} + \sigma_{r+2} + ... + \sigma_N), \tag{4.17}$$

where $\{\sigma_{r+1}, ..., \sigma_N\}$ represent the truncated Hankel singular values, though this bound can be loose when the Hankel singular values are close to one another [Enn84, Glo84]. The maximum singular values of K_s, K_r, and $K_s - K_r$ are plotted in Figure 4.7. The graph indicates that K_r approximates K_s with little frequency response error. Furthermore, the

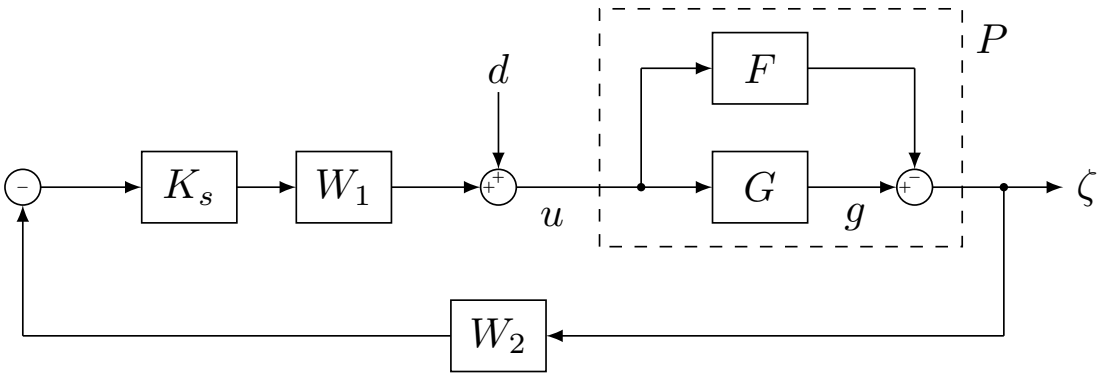

Figure 4.6: Feedback diagram with the plant pre- and post-shaping weights, W_1 and W_2, respectively. The controller, K_s, is synthesized from a normalized coprime factorization of the shaped plant. The reduced-order approximation of K_s is implemented in practice and the plant shaping weights are lumped into the controller realization.

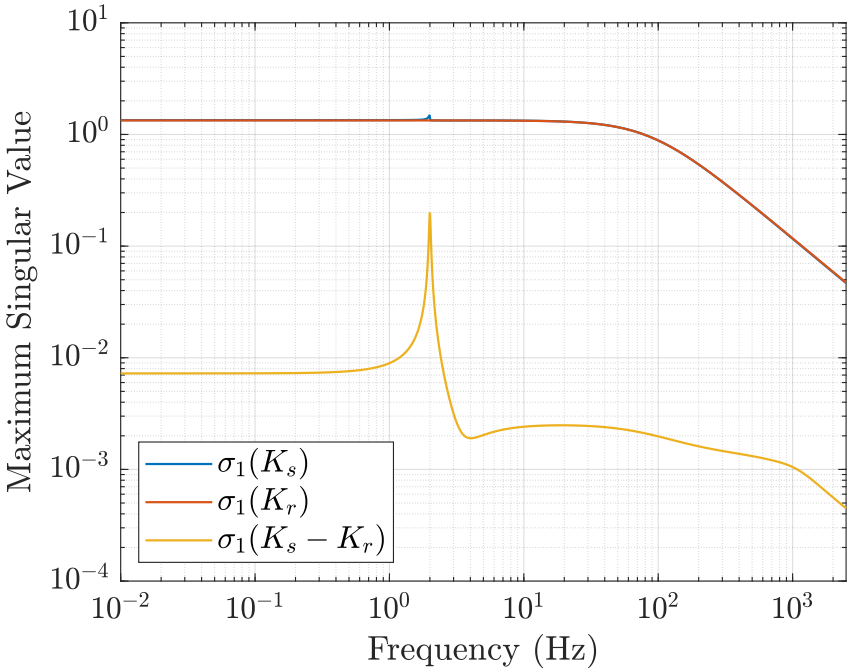

Figure 4.7: Maximum singular values of the 106-state robustly stabilizing controller, reduced 3-state controller generated from a balanced truncation, and difference between the two controller realizations.

plot reveals that the upper bound of 0.81 provided by (4.17) is quite conservative. With the reduced-order controller, the closed-loop system is robustly stable to coprime factor perturbations of norm 0.46.

The plant shaping weight is absorbed into the filter implemented, K_0, according to

$$K_0 = W_1 K_r W_2. \tag{4.18}$$

For the disk suspension shaping weights, this corresponds to $K_0 = 4K_r$. The $\mathcal{H}_\infty$ norm of both the sensitivity and complementary sensitivity functions with K_0 are shown in Figure 4.8 to be approximately 1.2 and 1.5, respectively. Thus, the closed-loop system is robust to large unstructured multiplicative uncertainty at the plant output. Furthermore, the low gain input-output direction of the system is essentially open-loop, so the norm of S_o is close to 1 at low frequencies. Analysis of the input sensitivity and input complementary sensitivity functions yields very similar results.

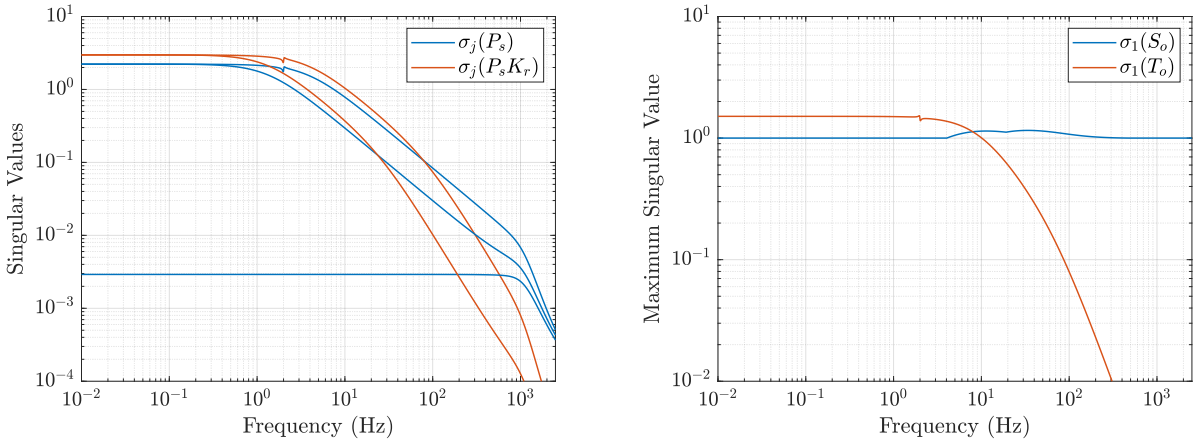

Figure 4.8: Left: Singular values, σ_j, $j = 1, 2, 3, 4$, of the shaped plant, P_s, and output loop gain, P_sK_r, using the reduced-order controller. Only three traces appear for each function because $\sigma_1 = \sigma_2$. Right: Maximum singular values of the predicted output sensitivity function, S_o, and output complementary sensitivity function, T_o.

4.3 Identification of the Stabilized Plant

4.3.1 Plant empirical frequency response

Prior to closing the loop, the actuator-to-pick-off feedthrough must be estimated. This is accomplished by supplying the transformer center taps with their nominal currents and then applying broadband test signals at the inputs, u_j. The amplitude of test inputs is too small to move the disk, which is at rest on the photoresist coating the bottom electrodes, thus, the measurements are due solely to the feedthrough. Unlike the analytical model in which the feedthrough is present only in the diagonal elements of the four-input/four-output system, all sixteen elements of the feedthrough matrix must be quantified in the physical system to determine the feedforward filter, F. The empirical frequency response of the feedthrough is shown in Figure 4.9. The largest off-diagonal elements, with DC magnitudes of about 0.06 V/V, correspond to the subdiagonal and superdiagonal channels that share a common supply transformer, i.e., $\{F_{12}, F_{21}\}$ and $\{F_{34}, F_{43}\}$. Each channel is fit with a 15-tap FIR filter to create the feedforward filter, F, that is implemented by the DSP in parallel with the subsystem, G, as shown in Figure 4.6.

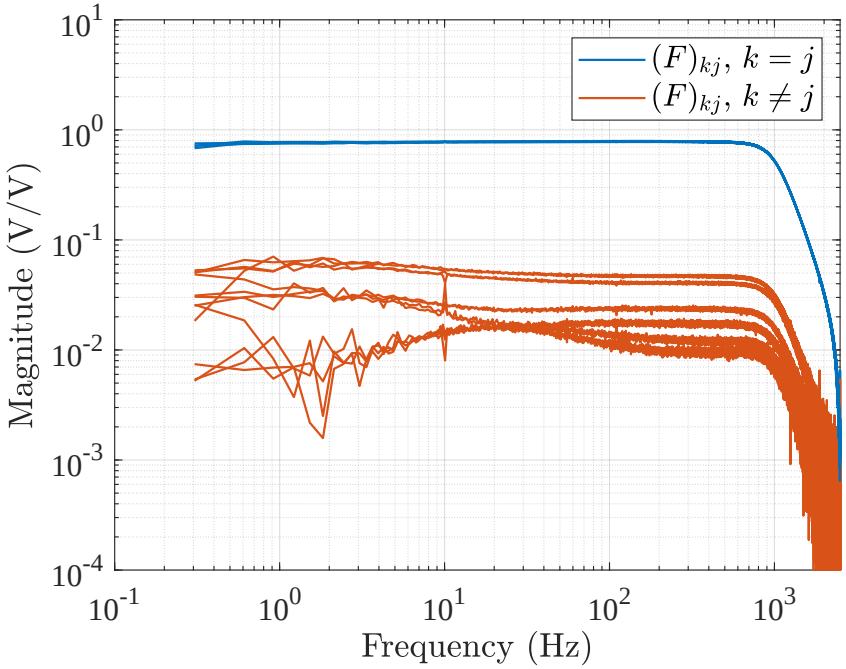

Figure 4.9: Measurements of actuator-to-pick-off feedthrough with the disk resting at its bottom position. The diagonal channels dominate, however, an FIR model is fit to all elements and implemented as the four-input/four-output feedforward filter, F.

With the feedforward filter in place, the 3-state controller, K_0, is discretized using Tustin's method and closing the loop successfully suspends the disk. Broadband test inputs are injected at d in Figure 4.6 to generate empirical frequency responses of the closed-loop transfer matrices PS_i and S_i, where S_i is the input sensitivity function. The plant identification process is time consuming due to the relatively low frequency dynamics, however, there are no constraints on the duration of the system identification tests so low variance closed-loop frequency responses are obtained by time-averaging the periodograms computed from non-overlapping segments of Tukey-windowed data. Since the condition number of S_i does not exceed 3.5, the empirical frequency response of the open-loop plant, denoted P_{emp}, is reliably computed by evaluating $(PS_i)(S_i)^{-1}$ on a frequency-by-frequency basis. The results are shown in Figure 4.10 from the perspective of input u_1. The responses of the individual channels display good agreement with the first principles analytical model, which is represented by the dashed traces in the figure. The frequency responses of the remaining channels are provided in Figure 4.13, though the dashed lines in these plots represent the parametric fit

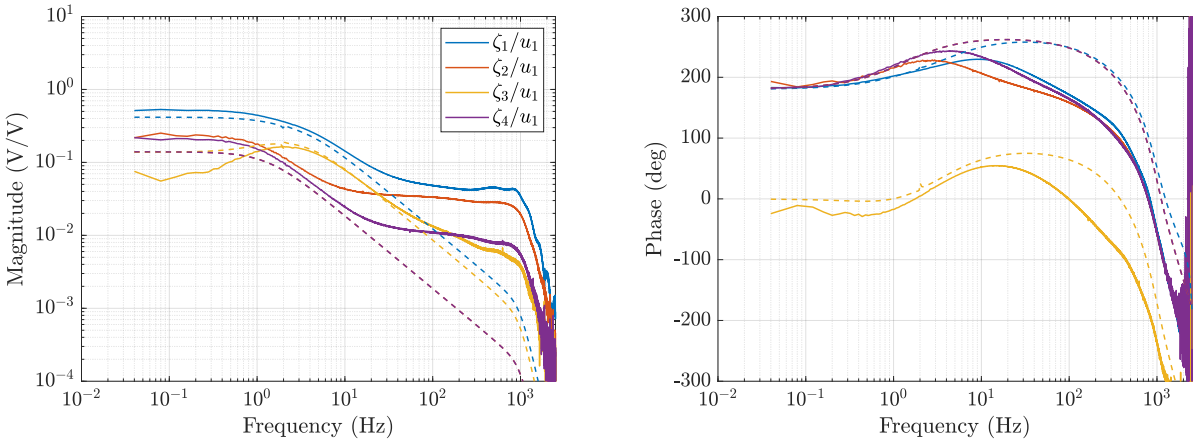

Figure 4.10: Comparison of the measured (solid) and analytical (dashed) frequency responses for input u_1. Empirical frequency responses for the remaining input/output channels are pictured in Figure 4.13.

of the following subsection. The DC gains are larger, and the unstable tilt eigenvalues are "faster" in the physical system compared to those of the analytical model. This is most likely due to errors in the estimate of the actual center tap currents applied to the transformers –larger than modeled currents will produce both of these observed effects. The unstable vertical eigenvalue, however, is slower in the physical system than in the analytical model. The instabilities are dependent on the system damping, thus, error in the estimated vertical damping coefficient is likely the culprit. Nevertheless, the controller synthesized for the analytical model is robust enough to suspend the physical disk. The largest discrepancy between the system and its analytical model is due to inexact cancellation of actuator-to-pick-off feedthrough. Although the degree of cancellation varies by channel, a 20× reduction in feedthrough can be routinely achieved. Residual feedthrough, though, causes the plant singular values to level off above 50 Hz. This has the deleterious effect of creating right half-plane zeros in the elements with larger residual feedthrough. This is clear from the empirical frequency response in Figure 4.10, where the high frequency phase exhibits more lag than the analytical model. This behavior can also be confirmed using only partial feedthrough cancellation in the analytical model. Although difficult to see in Figure 4.10, the lateral modes are damped oscillators with a frequency of about 2.6 Hz.

4.3.2 Parametric plant model

A parametric model can be derived from the empirical frequency response using the eigensystem realization algorithm [HK66]. Since FFT-based techniques were used to obtain P_{emp}, the system's impulse response, h, is estimated by applying the inverse discrete Fourier transform to P_{emp}. The signals produced from the inverse FFT are shown in Figure 4.11, where it is clear that the plant instabilities manifest in the noncausal response for sample indices $\ell \leq 0$, where $t = \ell t_s$. It is necessary to have sufficient frequency resolution so that the time-domain transients are fully captured. In the present work, the resolution of the empirical frequency response is 0.04 Hz, which corresponds to estimating h over a 25 second interval centered about $t = 0$ –this duration is much longer than required to capture the transients in h. The samples for $\ell > 0$ and for $\ell \leq 0$ can be used in two separate identification problems based on the Ho-Kalman method as discussed in [AB17]. This segregates the system into two isolated subsystems: one purely stable and the other purely unstable. Let discrete-time realizations for the stable and unstable components be

$$\begin{cases} x_{\text{s}}(\ell t_s) = A_{\text{s}} x_{\text{s}}(\ell t_s) + B_{\text{s}} u(\ell t_s) \\ y_{\text{s}}(\ell t_s) = C_{\text{s}} x_{\text{s}}(\ell t_s) \end{cases} \tag{4.19}$$

$$\begin{cases} x_{\text{u}}(\ell t_s) = A_{\text{u}} x_{\text{u}}(\ell t_s) + B_{\text{u}} u(\ell t_s) \\ y_{\text{u}}(\ell t_s) = C_{\text{u}} x_{\text{u}}(\ell t_s), \end{cases} \tag{4.20}$$

respectively. The state-space feedthrough, or "D", matrices can be assumed to be zero because of the anti-alias and smoothing filters and the zero-order hold implemented in the DACs. The impulse response of the stable system given in terms of its Markov parameters is

$$h_{\text{s}}(\ell t_s) = \begin{cases} 0 & \ell = \ldots, -2, -1, 0 \\ C_{\text{s}} A_{\text{s}}^{k-1} B_{\text{s}} & \ell = 1, 2, 3, \ldots \end{cases} \tag{4.21}$$

and the eigensystem realization algorithm establishes a 19-state model from the causal segment of the impulse response data. Identifying the Markov parameters for the $\ell \leq 0$ component of the impulse response is achieved by manipulating the frequency response function

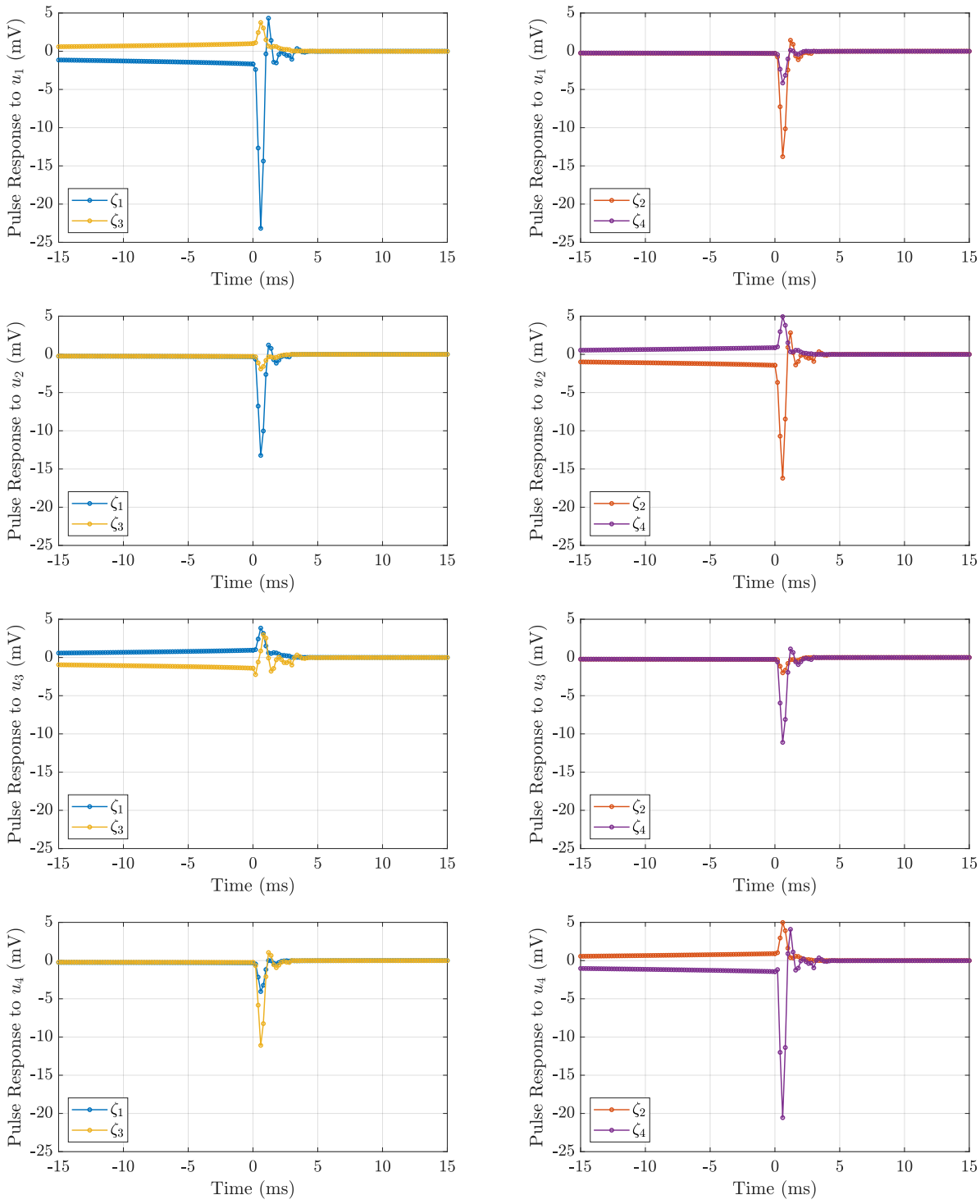

Figure 4.11: Pulse response of ζ from u, estimated by applying the inverse discrete Fourier transform to the empirical frequency response. The markers indicate the individual samples.

of (4.20):

$$\begin{aligned} H_{\mathrm{u}}(\omega) &= C_{\mathrm{u}} \left(e^{\jmath\omega t_s} I - A_{\mathrm{u}}\right)^{-1} B_{\mathrm{u}} \\ &= C_{\mathrm{u}} \left(e^{\jmath\omega t_s} \left(A_{\mathrm{u}}^{-1} - e^{-\jmath\omega t_s} I\right) A_{\mathrm{u}}\right)^{-1} B_{\mathrm{u}} \\ &= -C_{\mathrm{u}} A_{\mathrm{u}}^{-1} \left(e^{-\jmath\omega t_s} I - A_{\mathrm{u}}^{-1}\right)^{-1} B_{\mathrm{u}} e^{-\jmath\omega t_s}. \end{aligned} \tag{4.22}$$

Defining $\tilde{A}_{\mathrm{u}} = A_{\mathrm{u}}^{-1}$, $\tilde{B}_{\mathrm{u}} = B_{\mathrm{u}}$, and $\tilde{C}_{\mathrm{u}} = -C_{\mathrm{u}} A_{\mathrm{u}}^{-1}$, the frequency response in (4.22) can be expressed as

$$H_{\mathrm{u}}(\omega) = \tilde{C}_{\mathrm{u}} \left(e^{-\jmath\omega t_s} I - \tilde{A}_{\mathrm{u}}\right)^{-1} \tilde{B}_{\mathrm{u}} e^{-\jmath\omega t_s}. \tag{4.23}$$

The time-domain samples can be recovered using the inverse discrete-time Fourier transform,

$$\begin{aligned} h_{\mathrm{u}}(\ell t_s) &= \frac{1}{2\pi} \int_{-\omega_N}^{\omega_N} H_{\mathrm{u}}(\omega) e^{\jmath\omega\ell t_s} d\omega \\ &= \frac{1}{2\pi} \int_{-\omega_N}^{\omega_N} \tilde{C}_{\mathrm{u}} \left(e^{-\jmath\omega t_s} I - \tilde{A}_u\right)^{-1} \tilde{B}_{\mathrm{u}} e^{\jmath\omega(\ell-1)t_s} d\omega, \end{aligned} \tag{4.24}$$

where ω_N is the Nyquist frequency. Applying the change of variable $\nu = -\omega$ and defining a new sample index, $\tilde{\ell} = -(\ell - 1)$, the recovered pulse response samples are given by

$$h_u((-\tilde{\ell} + 1)t_s) = \frac{1}{2\pi} \int_{-\omega_N}^{\omega_N} \tilde{C}_{\mathrm{u}} \left(e^{\jmath\nu t_s} I - \tilde{A}_{\mathrm{u}}\right)^{-1} \tilde{B}_{\mathrm{u}} e^{\jmath\nu\tilde{\ell} t_s} d\nu. \tag{4.25}$$

The $\tilde{C}_{\mathrm{u}} \left(e^{\jmath\nu t_s} I - \tilde{A}_{\mathrm{u}}\right)^{-1} \tilde{B}_{\mathrm{u}}$ portion of the integrand resembles the frequency response of an asymptotically stable, causal system, so

$$\frac{1}{2\pi} \int_{-\omega_N}^{\omega_N} \tilde{C}_{\mathrm{u}} \left(e^{\jmath\nu t_s} I - \tilde{A}_{\mathrm{u}}\right)^{-1} \tilde{B}_{\mathrm{u}} e^{\jmath\nu\tilde{\ell} t_s} d\nu = \begin{cases} 0 & \tilde{\ell} \leq 0 \\ \tilde{C}_{\mathrm{u}} \tilde{A}_{\mathrm{u}}^{\tilde{\ell}-1} \tilde{B}_{\mathrm{u}} & \tilde{\ell} > 0. \end{cases} \tag{4.26}$$

Converting back to the original sample index and state-space realization, $(A_{\mathrm{u}}, B_{\mathrm{u}}, C_{\mathrm{u}})$, the impulse response of the unstable system is given by

$$h_u(\ell t_s) = \begin{cases} -C_{\mathrm{u}} A_{\mathrm{u}}^{\ell-1} B_{\mathrm{u}} & \ell \leq 0 \\ 0 & \ell > 0. \end{cases} \tag{4.27}$$

Two Hankel matrices of the backward-time transient –starting from $\ell = 0$ and $\ell = -1$, respectively, and propagating backward in time –are used to identify the $(\tilde{A}_{\mathrm{u}}, \tilde{B}_{\mathrm{u}}, \tilde{C}_{\mathrm{u}})$ realization in balanced coordinates following the Ho-Kalman method, from which $\{A_{\mathrm{u}}, B_{\mathrm{u}}, C_{\mathrm{u}}\}$ can be recovered.

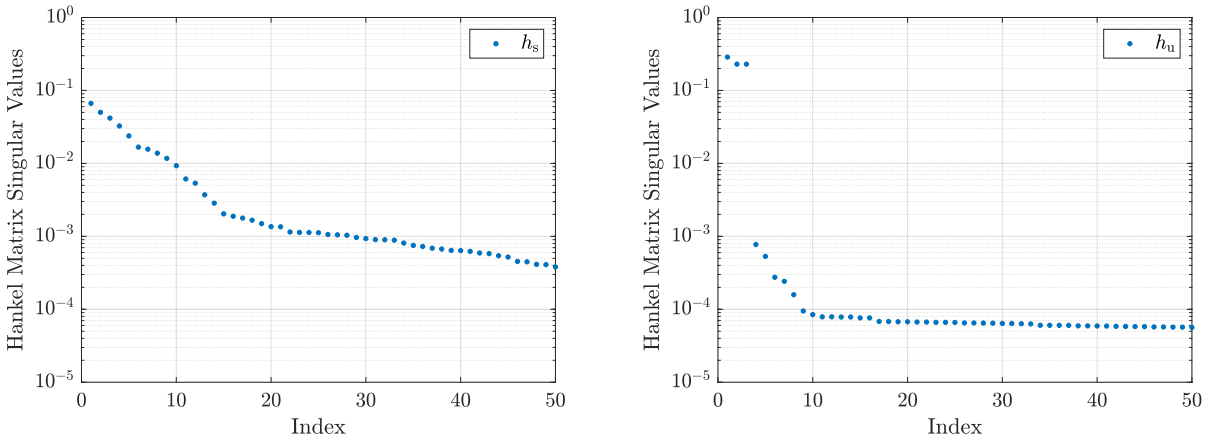

Figure 4.12: Fifty largest singular values of the Hankel matrices composed of the causal (left) and noncausal (right) segments of the impulse response. Three singular values dominate the noncausal segment of the response, implying that the system is characterized by three instabilities.

The singular values of the Hankel matrices developed for the stable and unstable components of h are graphed in Figure 4.12. The singular values suggest that the noncausal segment of h can be modeled by a 3-state system, thus confirming the number of instabilities predicted by the analytical model. Meanwhile, the singular values of the Hankel matrix constructed by the causal segment of h do not provide much information as to the state dimension of a low-order model that matches the impulse response data well. An iterative process to reasonably fit the causal data with the minimum number of states identifies a stable model of order 19. The parametric discrete-time realization of P_{emp} is the aggregate of the model fits to the stable and unstable components, yielding a 22-state model characterized by the state-space realization

$$A = \begin{bmatrix} A_{\text{s}} & 0 \\ 0 & A_{\text{u}} \end{bmatrix}, \quad B = \begin{bmatrix} B_{\text{s}} \\ B_{\text{u}} \end{bmatrix}, \quad C = \begin{bmatrix} C_{\text{s}} & C_{\text{u}} \end{bmatrix}. \tag{4.28}$$

The frequency response of the identified (parametric) plant model shows excellent agreement with the empirical frequency response –the dotted traces in Figure 4.13 are the identified model frequency response and Figure 4.14 compares the singular values of the measured frequency response data and to those of the identified model.

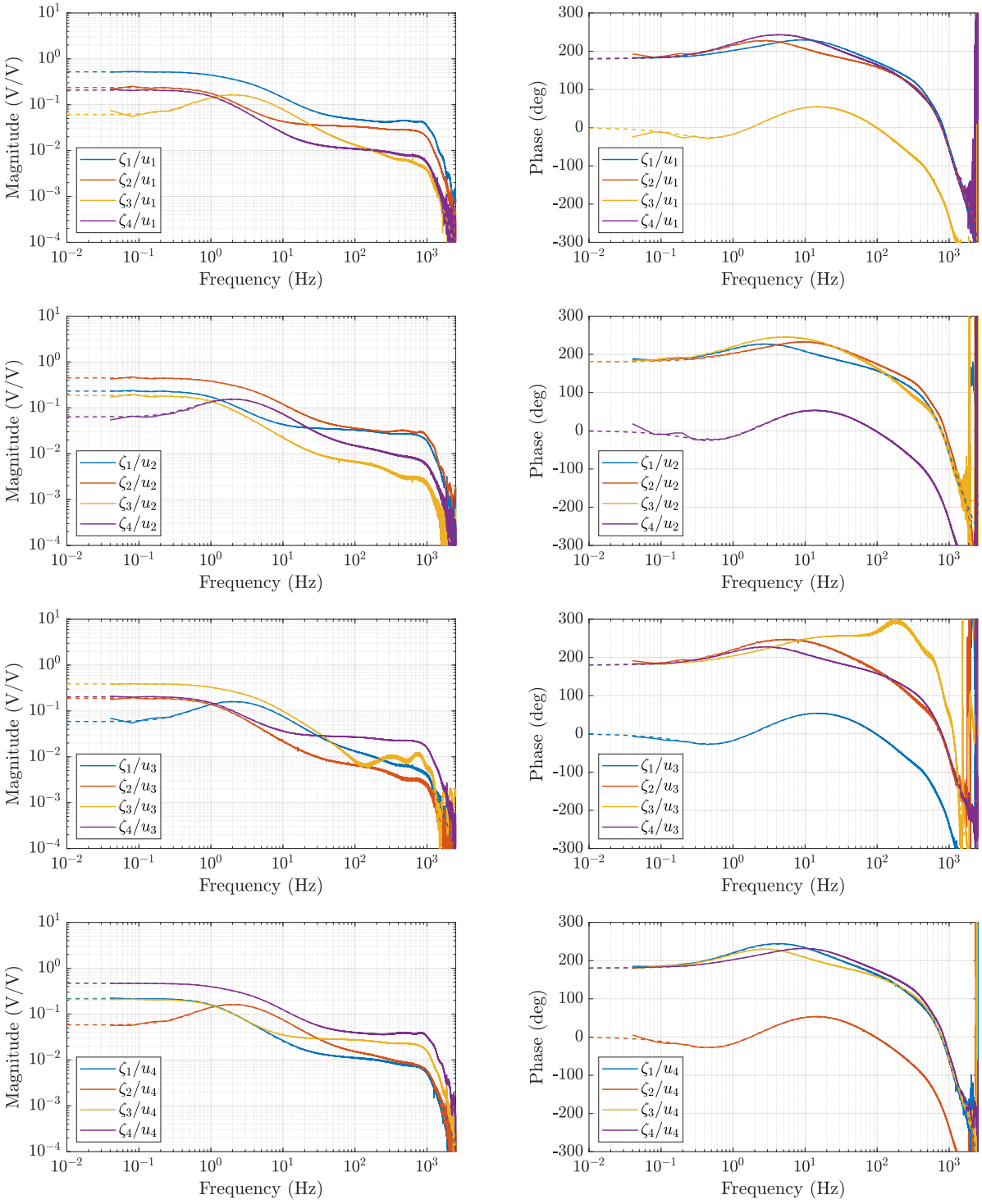

Figure 4.13: Empirical (solid) and 22-state parametric fit (dashed) frequency response from u to ζ.

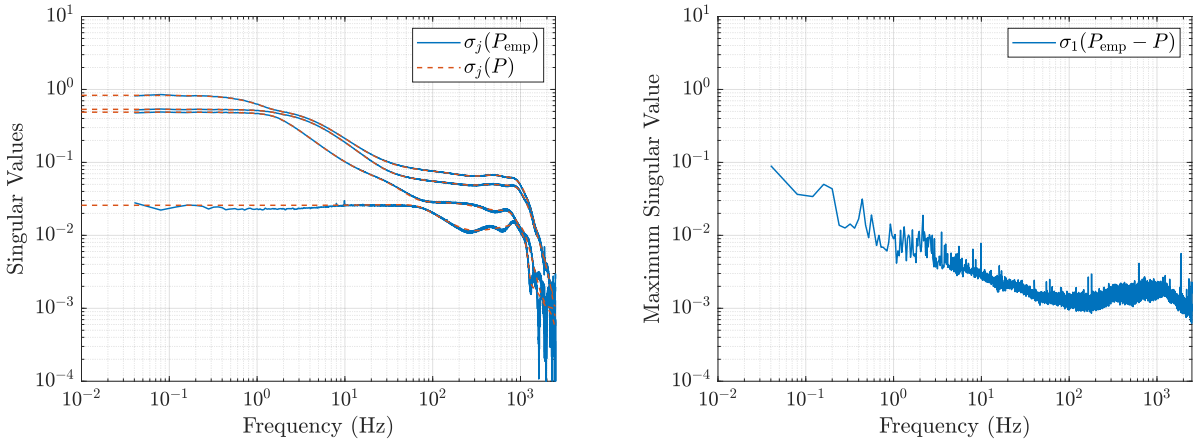

Figure 4.14: Left: Singular values of the empirical model, P_{emp}, and parametric fit, P. Right: Norm of the error between the empirical model and the parametric model.

4.4 Updated Controller

The norm of the sensitivity and complementary sensitivity functions computed with the initial controller, K_0, and identified plant model from Section 4.3, denoted P, are shown later in Figure 4.16. The stability margins are adequate ($\|S_o\|_\infty \approx 2.0$ and $\|T_o\|_\infty \approx 1.6$), however, the lack of integrators in the loop means low frequency disturbance rejection and command tracking will suffer. A second controller design, which includes integral action, is based on the identified plant. Weighting each of the four control efforts with integrators, however, destabilizes the closed-loop system. This is unsurprising considering the disk's $\{z, \theta, \varphi\}$ configuration is defined by three points, so an inconsistent specification can be produced by defining four gaps. Since it is desired to regulate the disk's vertical position and two angles, the four measurements are consolidated into three new signals proportional to these variables. This is accomplished by determining the directions associated with the unstable eigenvalues. Following the notation used in Section 2.2.6, the normalized output directions are

$$\begin{aligned} v_{1_o} &= \begin{bmatrix} 0.5308 & 0.5024 & 0.4770 & 0.4882 \end{bmatrix}^T \\ v_{2_o} &= \begin{bmatrix} 0.0053 & 0.7107 & 0.0175 & -0.7033 \end{bmatrix}^T \\ v_{3_o} &= \begin{bmatrix} -0.7293 & -0.0476 & 0.6801 & 0.0577 \end{bmatrix}^T, \end{aligned} \tag{4.29}$$

corresponding to eigenvalues $\lambda_1 = 1.0014$, $\lambda_2 = 1.0050$, and $\lambda_3 = 1.0052$. These represent the vertical and two tilt instabilities, respectively. The output directions are nearly orthonormal so $\mathcal{D}_{\text{o}} \in \mathbb{R}^{4\times 3}$ is defined as

$$\mathcal{D}_{\text{o}} = \arg \min_{\substack{\mathcal{D} \\ \mathcal{D}^T\mathcal{D}=I}} \left\| \mathcal{D} - \begin{bmatrix} v_{1_{\text{o}}} & v_{2_{\text{o}}} & v_{3_{\text{o}}} \end{bmatrix} \right\|_F, \tag{4.30}$$

where the Frobenius norm is used. The solution to the optimization problem in (4.30) is based on the left and right singular vectors of $[v_{1_{\text{o}}}\ v_{2_{\text{o}}}\ v_{3_{\text{o}}}]$ and yields a matrix whose columns are orthonormal and are closest to the output directions of the unstable eigenvalues [Hig89]. Similarly, the unstable input directions are

$$\begin{aligned} v_{1_{\text{i}}} &= \begin{bmatrix} 0.5338 & 0.4806 & 0.4681 & 0.5148 \end{bmatrix}^T \\ v_{2_{\text{i}}} &= \begin{bmatrix} -0.0570 & 0.6898 & 0.0521 & -0.7199 \end{bmatrix}^T \\ v_{3_{\text{i}}} &= \begin{bmatrix} -0.7406 & -0.0041 & 0.6720 & 0.0018 \end{bmatrix}^T, \end{aligned} \tag{4.31}$$

and a matrix, denoted $\mathcal{D}_{\text{i}} \in \mathbb{R}^{4\times 3}$, whose rows are orthonormal and is the closest approximation to the matrix of input directions is computed from the optimization problem

$$\mathcal{D}_{\text{i}} = \arg \min_{\substack{\mathcal{D} \\ \mathcal{D}^T\mathcal{D}=I}} \left\| \mathcal{D} - \begin{bmatrix} v_{1_{\text{i}}} & v_{2_{\text{i}}} & v_{3_{\text{i}}} \end{bmatrix} \right\|_F. \tag{4.32}$$

Pre- and post-multiplying the identified plant produces the three-input/three-output diagonally dominant system, denoted $\tilde{P} = \mathcal{D}_{\text{o}}^T P \mathcal{D}_{\text{i}}$, in Figure 4.15. The three scalar output signals of $\tilde{P}$ are voltages approximately proportional to the $\{z, \theta, \varphi\}$ kinematic variables of the disk with the proportionality constants approximated as the scale factors reported at the end of Section 4.1. Meanwhile, each of the three input signals to $\tilde{P}$ controls a single degree of freedom of the disk. The inputs and outputs of $\tilde{P}$ are denoted $\tilde{u} = [u_z\ u_\theta\ u_\varphi]^T$ and $\tilde{\zeta} = [\zeta_z\ \zeta_\theta\ \zeta_\varphi]^T$, respectively. The nonzero DC gain in the diagonal channels corresponding to the tilt degrees of freedom is indicative of this system's ability to specify out-of-plane rotational motion of the disk. This is in contrast to the larger disk discussed in the preceding chapters and investigated in [AM21], which was incapable of maintaining nonzero angular rotations.

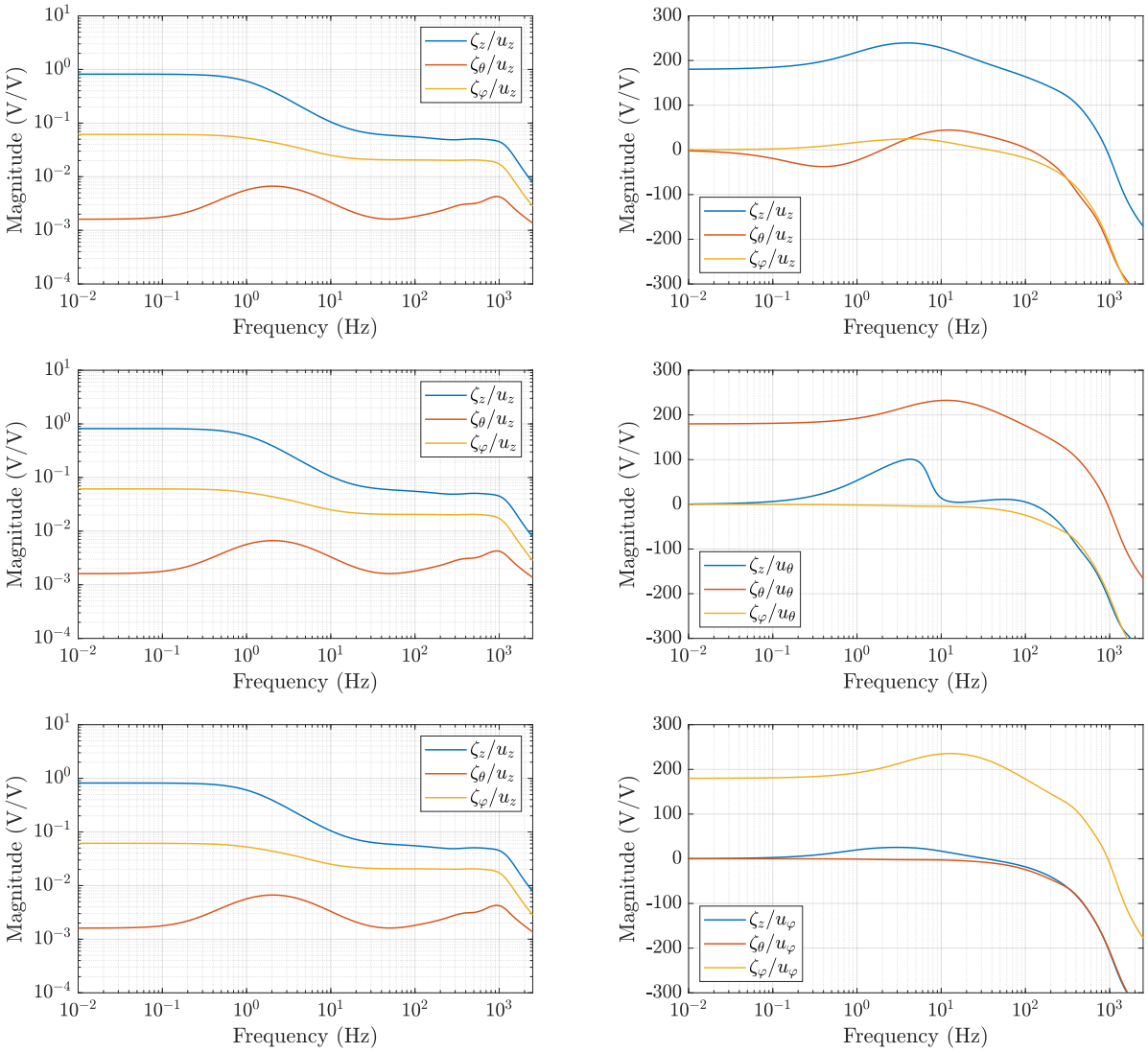

Figure 4.15: Frequency response of the three-input/three-output transformed plant, $\tilde{P}$.

A new controller is designed to achieve precise control over the disk's vertical displacement and angles. The synthesis procedure is based on a coprime factorization of the identified plant, with the input and output transformations noted above. Accordingly, asymptotic regulation to desired values of $\{z, \theta, \varphi\}$ is achieved with proportional-integral pre-weighting of $\tilde{P}$ to produce the shaped plant

$$\tilde{P}_s = \left(4 + \tfrac{30}{s}\right) \tilde{P}. \tag{4.33}$$

A continuous-time representation of the weight is shown for readability. The singular values of $\tilde{P}$ and $\tilde{P}_s$ are shown in Figure 4.16. For the shaped plant, $\gamma_{\min} = 2.6$. A filter is synthesized

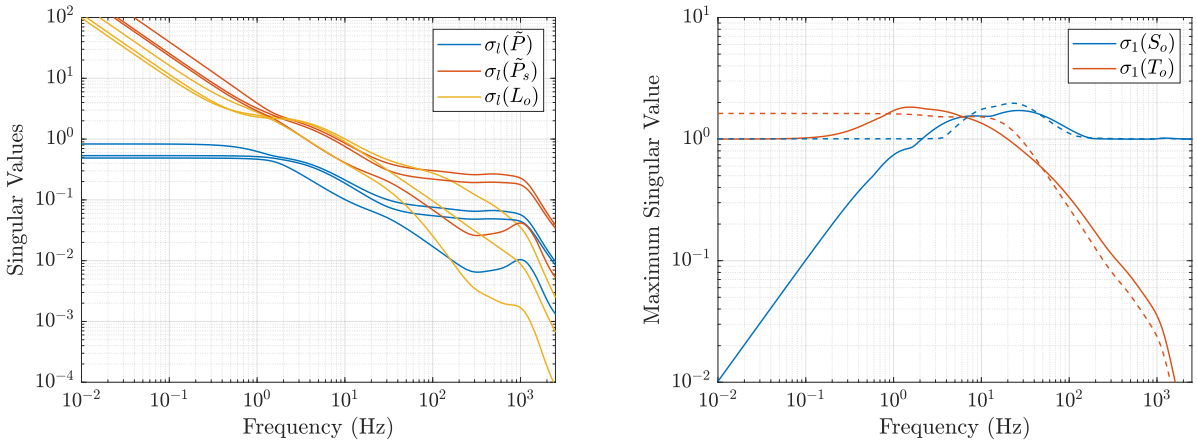

Figure 4.16: Left: Singular values of $\tilde{P}$, the shaped plant, $\tilde{P}_s$, and the output loop gain, L_o. Right: Maximum singular values of the output sensitivity and output complementary sensitivity functions computed with the identified plant model and two differing controllers: the updated controller, K, (solid traces) and initial controller, K_0, (dashed traces).

according to (4.15) using a normalized left coprime factorization of $\tilde{P}_s$ and $\gamma = 1.1 \times \gamma_{\min}$. After absorbing the plant weight into the filter, the controller can be reduced to a 9-state system, denoted K, with no loss in fidelity. The controller is implemented according to the block diagram in Figure 4.17 and produces a stable closed-loop system.

The output voltages of $\tilde{P}$ are converted into estimates of $\{z, \theta, \varphi\}$ using the scale factors from the analytical model (see Section 4.1). Step references are applied at r in Figure 4.17 and the responses are shown in Figure 4.18 with reference step heights of 2.8 μm for z and 0.18 mrad (0.01 degree) for $\{\theta, \varphi\}$. Note that these step sizes correspond to 0.2 V. The step references are applied in separate experiments to each channel of r: the first channel

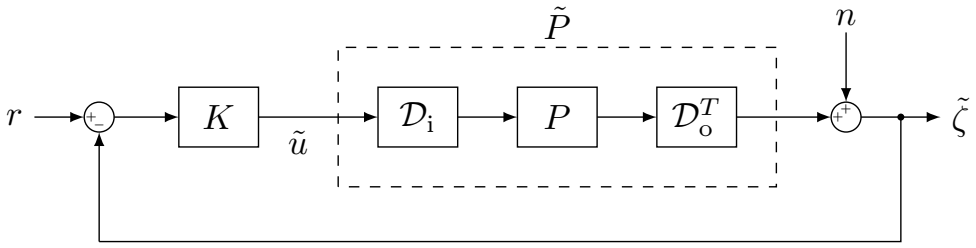

Figure 4.17: Closed-loop block diagram with the input and output transformation matrices that convert the plant into a diagonally dominant three-input/three-output system with output voltages proportional to the disk's kinematic variables $\{z, \theta, \varphi\}$. Measurement noise is represented by n.

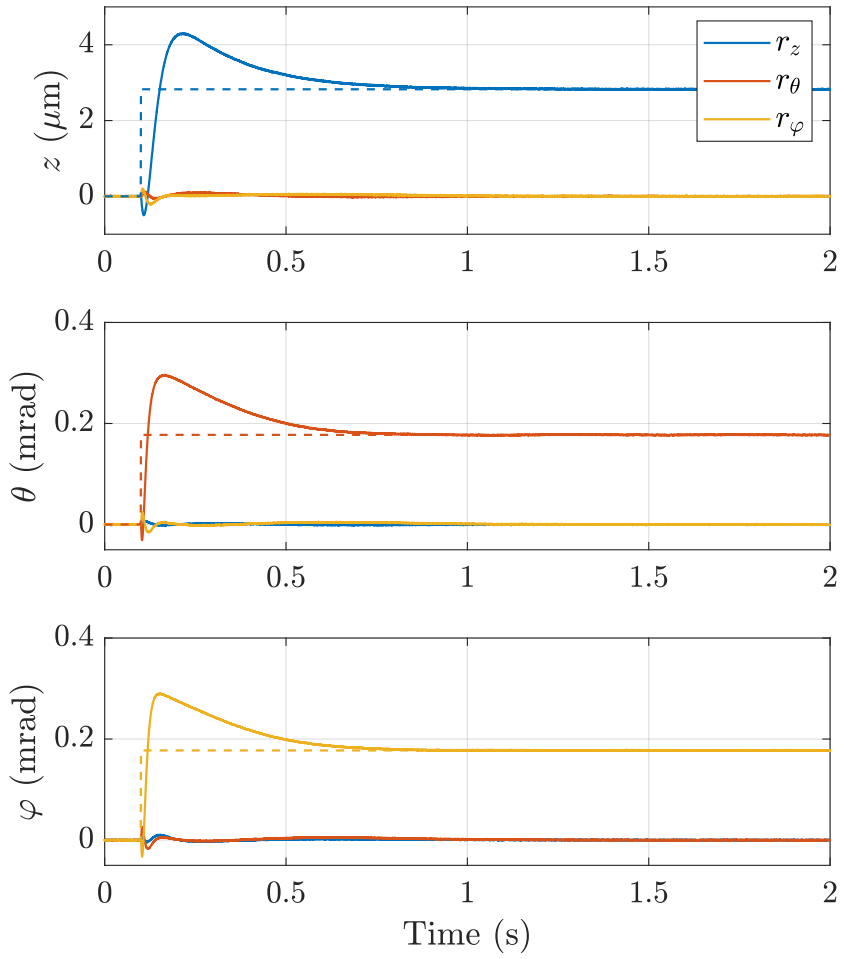

Figure 4.18: Step responses of $\{z, \theta, \varphi\}$ with references shown by the dotted lines. Top: $r_z \neq 0, r_\theta = 0, r_\varphi = 0$; middle: $r_z = 0, r_\theta \neq 0, r_\varphi = 0$; bottom: $r_z = 0, r_\theta = 0, r_\varphi \neq 0$.

corresponds to the vertical displacement and is denoted r_z; likewise, r_θ and r_φ represent the references for the angle measurements. The closed-loop time constants are consistent with the singular value crossover frequencies associated with $\tilde{P}_s$.

The noise spectral density, S_{nn}, reflected to the output of $\tilde{P}$ is of interest since this will determine the ultimate measurement resolution of the disk's position and angles. With $r = 0$, the auto-spectral densities, $S_{\tilde{u}\tilde{u}}$ and $S_{\tilde{\zeta}\tilde{\zeta}}$, and cross-spectral density, $S_{\tilde{\zeta}\tilde{u}}$, of the closed-loop

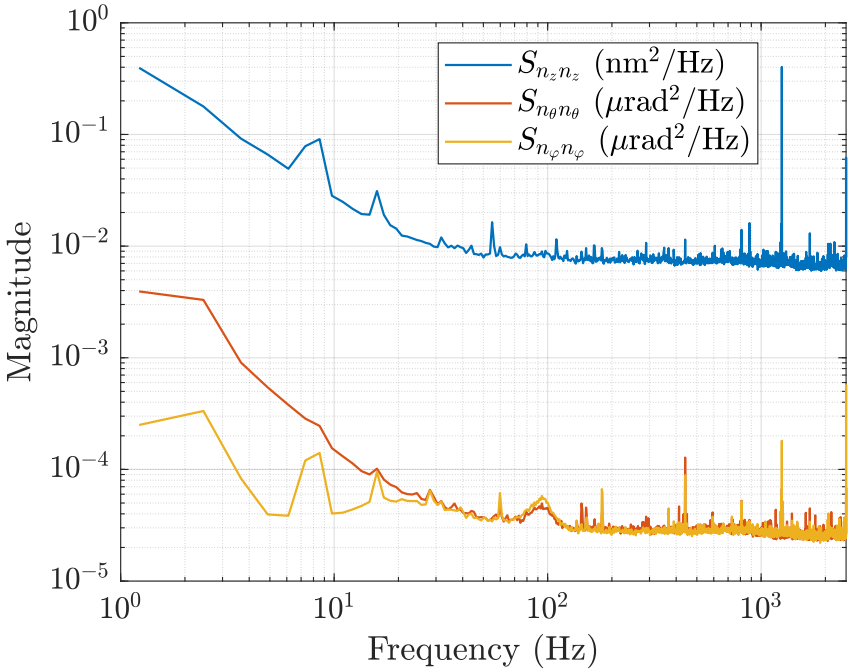

Figure 4.19: Power spectral density of signal noise at the plant output with the disk suspended at its nominal position.

signals in Figure 4.17 are estimated and S_{nn} is recovered from

$$\begin{bmatrix} S_{\tilde{\zeta}\tilde{\zeta}} & S_{\tilde{\zeta}\tilde{u}} \\ S^*_{\tilde{\zeta}\tilde{u}} & S_{\tilde{u}\tilde{u}} \end{bmatrix} = \begin{bmatrix} S_o \\ -KS_o \end{bmatrix} S_{nn} \begin{bmatrix} S_o^* & -(KS_o)^* \end{bmatrix}. \tag{4.34}$$

The diagonal elements of S_{nn}, which describe the noise spectra of $\{z, \theta, \varphi\}$, are shown in Figure 4.19 (double-sided spectral densities are shown for positive frequencies). Shorter data records are used in the spectral estimation so the frequency resolution is coarser than the empirical frequency responses. The noise identification experiments exhibit a greater number of periodogram averaging, however, so the time durations of the experiments are similar, representing the trade-off between variance and frequency resolution.

The noise spectra reveal that the disk position and angles are measured with high precision: the full bandwidth (DC-2.5 kHz) resolution of the vertical disk position is approximately 6.3 nm; similarly, the angle measurement resolution is approximately 0.41 μrad, or about 23 μdeg. This sensitivity to motion is due to the large capacitances formed between the disk and electrodes. If narrowband measurements are desired, these noise figures are

reduced even further, i.e., the measurement uncertainty in z is 2.1 nm from DC-100 Hz. The RMS errors estimated from the noise spectra are corroborated by measuring the RMS errors of the settled step response signals in Figure 4.18.

Part II

Segregated Control and Sense Electrodes

CHAPTER 5

Levitation Platform II

A new electrode configuration is designed to mitigate feedthrough by establishing separate control and sense electrodes. The new electrode arrangement, shown from above in Figure 5.1, mimics the design of the previous electrodes, however, each of the primary electrodes from Part I has been sliced into two sectors of roughly equal area by an arc of constant radius. This creates an additional "ring" of electrodes on each glass plate and the top and bottom electrodes are denoted $\mathcal{E}_{\mathrm{t}_{ij}}$ and $\mathcal{E}_{\mathrm{b}_{ij}}$, respectively, for $i = 1, 2, 3,\ j = 1, 2, 3, 4$. The new top and bottom sets of electrodes are mirror images of one another. The inner ring of electrodes, corresponding to $i = 1$, are coined the "control electrodes" and will be used strictly for regulating the disk's vertical position, pitch, and roll. The middle annulus of electrodes, that is, $i = 2$, are deemed the "primary sense electrodes" and are used to measure vertical translations and two in-plane angular rotations of the disk. Finally, the outermost, or "lateral", electrodes, i.e., $i = 3$, measure in-plane translations of the disk. The updated electrodes provide no means of measuring rotations about the vertical axis nor can yaw moments be applied.

The electrodes are patterned on soda-lime glass plates and a $14.4\,\mu$m layer of photoresist is baked over the electrodes to guarantee a nonzero gap between the disk and electrodes and avoid electrical breakdown. Precision shims specify the net air gap between the disk and the two electrode sets so that the nominal air gaps of $114\,\mu$m remain unchanged. The inner radius of the control electrodes and outer radius of the primary sense electrodes are 1.5 mm and 37 mm, respectively, matching the inner and outer radii of the primary electrodes in Part I, and the lateral electrode geometry here is identical to before. When the disk is horizontally suspended with its center of mass located at the origin of the inertial frame, the

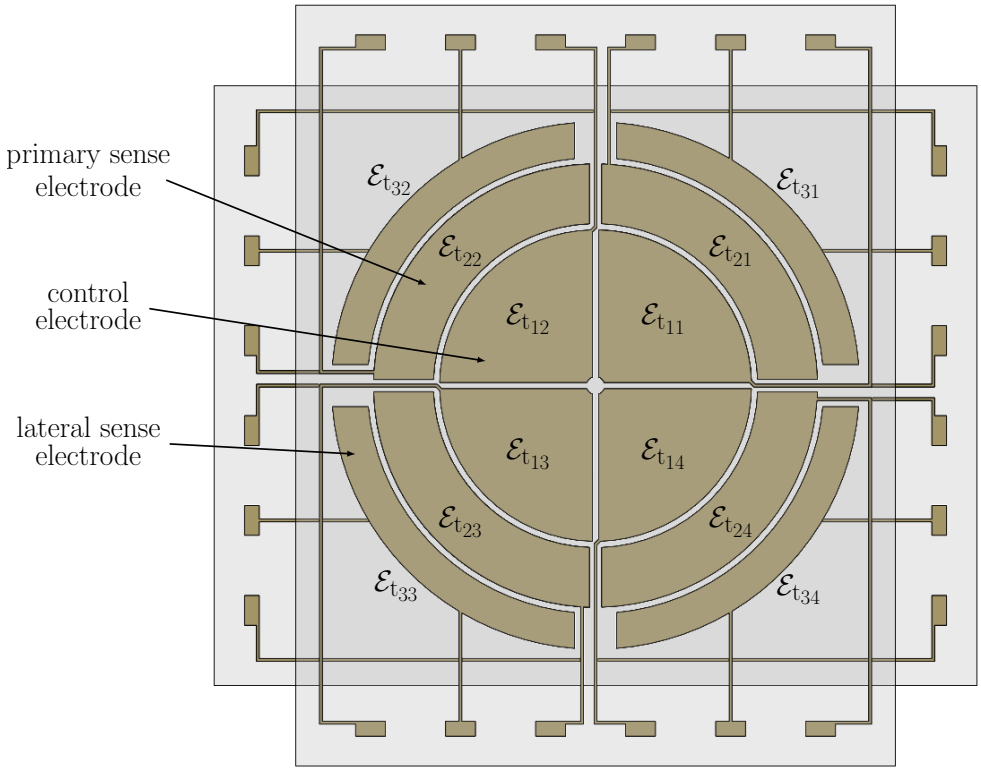

Figure 5.1: Top view of the updated electrode configuration. The bottom set of electrodes is a duplicate of the top set.

capacitances between the disk and each of the control electrodes are 37.9 pF. The electrode-disk capacitances of the primary sense electrodes and lateral electrodes are approximately 36.3 and 12.4 pF, respectively, with the disk in this position. For additional details on the electrode geometry, refer to Appendix A.

The primary leads of center-tapped transformers are used to couple the electrodes in the manner described in Chapter 2, though each of the transformer circuits now serves a sole purpose: either actuation *or* measurement. The control and primary sense electrodes are configured in pairs of facing electrodes so that $\{\mathcal{E}_{t_{ij}}, \mathcal{E}_{b_{ij}}\}$, $i = 1, 2$, form a pair and the lateral electrodes are grouped antipodally where the top and bottom electrodes are shorted (see Figures 2.3 and 2.4). A total of fifteen transformers are required for the new electrodes –ten to pair the electrodes and five to supply the center tap currents. All transformers are designed to be matched. No measurements are taken from the control electrodes, i.e., the load across the transformer secondary is not picked-off. The "sense voltage" signals, $v_{s_{ij}}$, are conditioned

and measured only for the primary sense and lateral electrodes. The electrode redesign calls for separate circuits for the control and pick-off signals in order to eliminate feedthrough, thus additional signal conditioning electronics are required even though the number of control inputs (four) and measurements (six) remains unchanged. The prior electronics are assigned to the control and lateral electrodes, and new boards are printed for the primary sense electrodes that match the signal transduction gains reported in Section 2.2.4. Photographs of the assembled electronics are provided in Figure 5.2, however, at the time of the photographs, the updated electrodes had not been fully fabricated, so the previous electrode plates are shown in place.

In an effort to mitigate residual coupling between the control inputs and measurements through sources such as common power supplies, the disk, etc., the control and sensing electrodes operate at separate carrier frequencies. The control carrier frequency, ω_{c}, and sense carrier frequency, ω_{s}, are 25 kHz and 30 kHz, respectively. The measurement demodulation phases, ψ_{s_k}, must be adjusted accordingly.

The reduced area of the control electrodes compared to the primary electrodes from Part I diminishes the control authority of the system. The area has effectively been cut in half so the voltages required to lift the disk using only the control electrodes must increase by a factor of $\sqrt{2}$. In order to avoid electrical arcing, however, the primary sense electrodes are used to provide additional lift so that similar electrode voltages to Part I are maintained for the disk at its nominal setpoint. This is accomplished using a constant amplitude, 30 kHz signal, v_{b}, added in series to the transformer secondary load to bias the primary sense electrodes. The bias signal, v_{b}, is supplied to all four primary sense electrode pairs and the signal phase is selected to maximize the voltage differential on the top and bottom electrodes. This provides a new avenue for actuator-to-pick-off feedthrough, however, the bias signal amplitude is generated by the DSP and analog modulated to 30 kHz so that the analog demodulated sampled signal contains only a DC feedthrough term that is easily identified and negated by a constant gain feedforward filter in the DSP.

At the time of writing, system testing with the new electrode plates has not commenced,

so empirical results for the updated system are provided. Nevertheless, the following chapters develop models and synthesize controllers for the suspension of both the 37 mm and 41 mm radius disks.

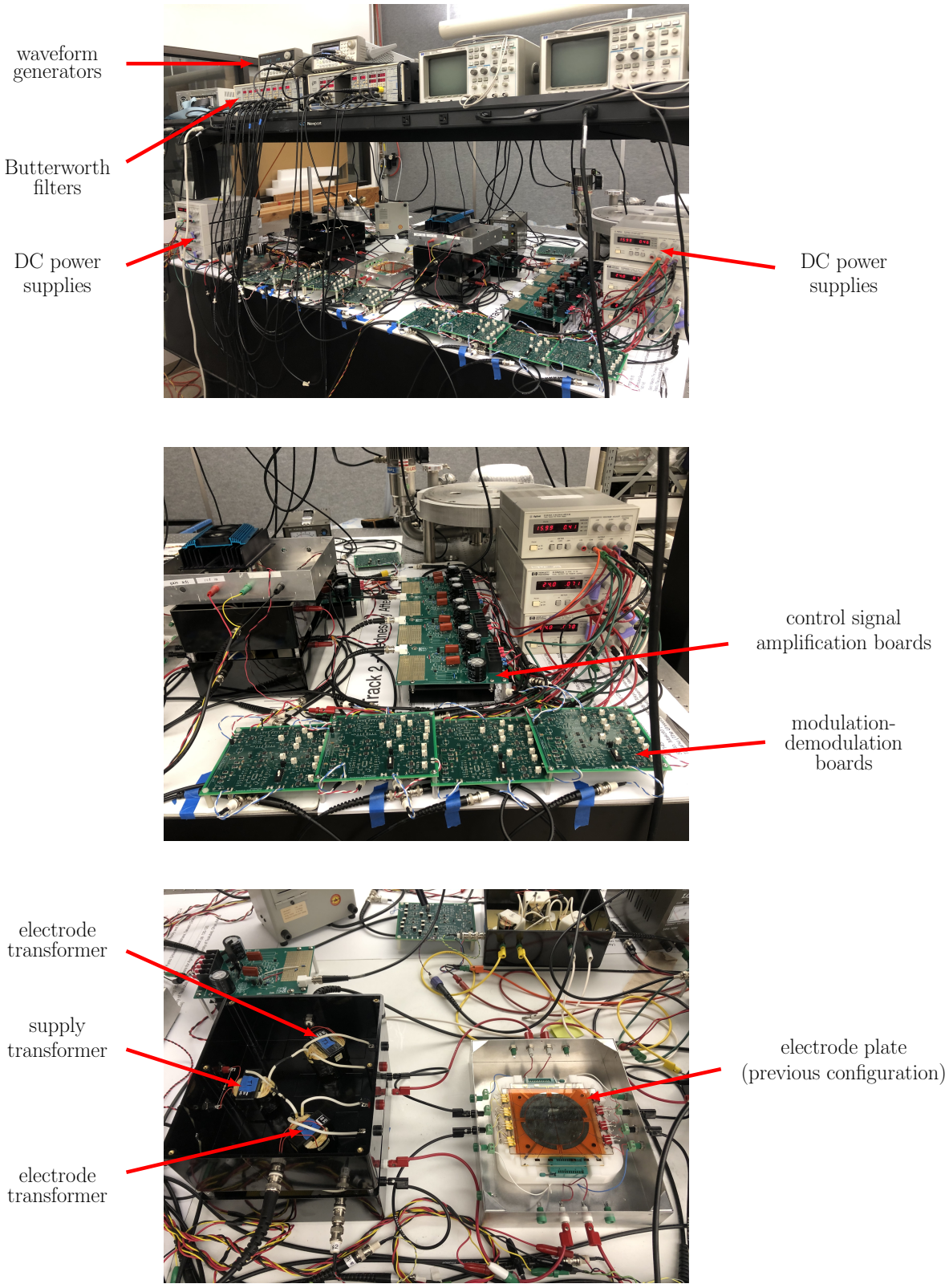

Figure 5.2: Photographs of the assembled electronics for the updated electrode configuration. Top: overview of all electronics; middle: signal conditioning boards; bottom: transformers.

CHAPTER 6

Three-Degree-of-Freedom Disk

Modeling and control design for the 37 mm radius disk is investigated in this chapter. Since the disk radius matches the outer radius of the primary sense electrodes, the electrostatic fringing field passively centers the disk laterally so that only the vertical position, roll, and pitch must be actively controlled. All electronics used for the lateral electrodes are disconnected.

6.1 Analytical Model

An analytical model of the disk with the new electrodes is developed following the modeling procedure outlined in Chapter 2. A free body diagram of the disk is provided in Figure 6.1 and shows the same forces and moments acting on the disk as in Figure 4.1, however, additional electrostatic forces are present and the magnitudes of the electrostatic forces are reduced from those of the prior electrode configuration. The lateral degrees of freedom are included in the model, though they have little impact. The yaw degree of freedom is ignored. The translational disk dynamics are governed by

$$\begin{aligned} m\ddot{x} &= -c_x\dot{x} - k_x x + \varphi \sum_{i,j} F_{\mathrm{n}_{ij}} \\ m\ddot{y} &= -c_y\dot{y} - k_y y - \theta \sum_{i,j} F_{\mathrm{n}_{ij}} \qquad\qquad i = 1,2 \\ m\ddot{z} &= -c_z\dot{z} - ma_{\mathrm{g}} + \sum_{i,j} F_{\mathrm{n}_{ij}} \qquad\qquad j = 1,2,3,4 \end{aligned} \tag{6.1}$$

and the equations for the observable angular degrees of freedom are

$$\begin{aligned} J_{\mathrm{t}}\ddot{\theta} &= -c_\theta\dot{\theta} + 2\left(J_{\mathrm{t}} - J_{\mathrm{s}}\right)\varphi\dot{\theta}\dot{\varphi} + \sum_{i,j}\left(\bar{y}_{ij} - y\right)F_{\mathrm{n}_{ij}} && i = 1,2 \\ J_{\mathrm{t}}\ddot{\varphi} &= -c_\varphi\dot{\varphi} + \left(J_{\mathrm{s}} - J_{\mathrm{t}}\right)\varphi\dot{\theta}^2 + \sum_{i,j}\left(x - \bar{x}_{ij}\right)F_{\mathrm{n}_{ij}}, && j = 1,2,3,4 \end{aligned} \tag{6.2}$$

where the coefficients of viscous damping are computed in Appendix C and the virtual springs that represent the fringing field forces are selected so that the lateral modes have a 2 Hz resonance.

The transformer dynamics for each control electrode are modeled from the schematic in

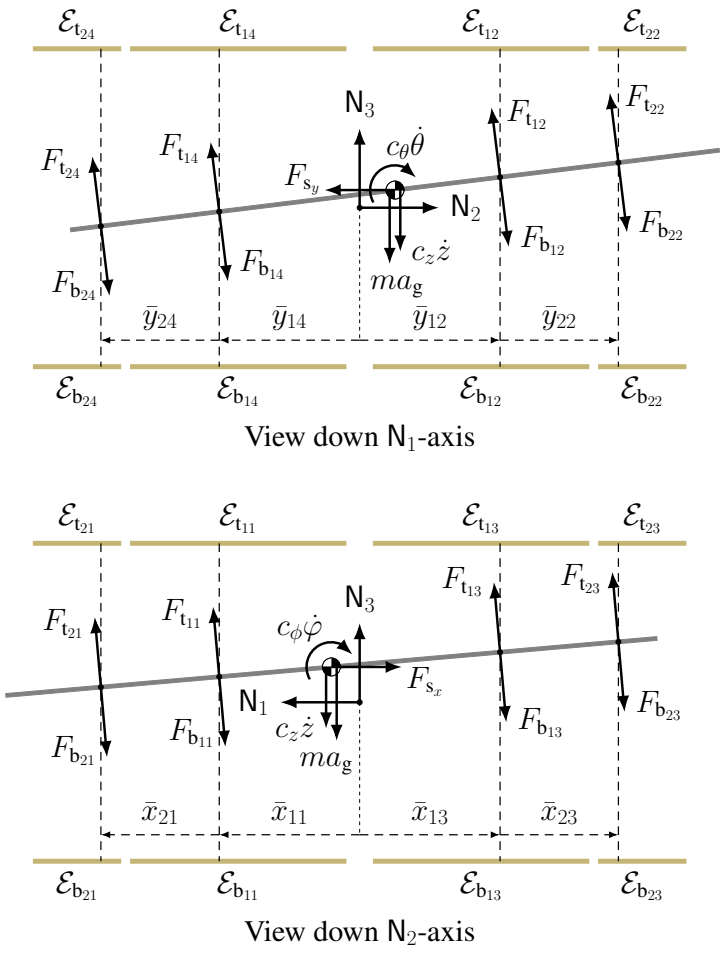

Figure 6.1: Free body diagram of the smaller disk with the new electrodes. All forces present in the previous electrode arrangement remain and additional electrostatic forces due to the increased number of electrodes are accounted for.

Figure 2.8 and given by

$$M_{\mathrm{tf}_{1j}}(q)\dot{w}_{\mathrm{tf}_{1j}} = A_{\mathrm{tf}_1} w_{\mathrm{tf}_{1j}} + (-1)^{j-1} B_{\mathrm{ct}_1} i_{\mathrm{ct}_1} + B_v v_{\mathrm{c}_j}, \qquad j = 1,2,3,4 \tag{6.3}$$

where the center tap current, $i_{\mathrm{ct}_1} = a_{\mathrm{ct}_1}\cos(\omega_{\mathrm{c}} t)$, has an amplitude of 12.8 mA. The current amplitude has been reduced from Part I in order to maintain similar voltages on the electrodes when the disk is suspended in its nominal position. Note that no output equation is included in (6.3) since the "sense voltages" for the control electrodes are not picked-off. The transformers for the primary sense electrodes are modeled on the same non-idealized transformers as the control electrodes, however, the bias voltage, v_{b}, replaces each of the control inputs, v_{c_j}. The bias voltage is equivalent in amplitude for each transformer, however the phases differ based on the phase of the center tap current. Thus, the bias voltage corresponding to electrode pair $\{\mathcal{E}_{\mathrm{t}_{21}}, \mathcal{E}_{\mathrm{b}_{21}}\}$ is in anti-phase with the bias voltage on electrode pair $\{\mathcal{E}_{\mathrm{t}_{22}}, \mathcal{E}_{\mathrm{b}_{22}}\}$. The same is true for the $j = 2, 4$ electrodes. To simplify the model, rather than consider four bias input signals to the system, only a single bias voltage input is modeled and the sign of the corresponding "B" matrix alternates on a channel-by-channel basis. The dynamics for the primary sense electrode transformers are governed by

$$\begin{aligned} M_{\mathrm{tf}_{2j}}(q)\dot{w}_{\mathrm{tf}_{2j}} &= A_{\mathrm{tf}_2} w_{\mathrm{tf}_{2j}} + (-1)^{j-1} B_{\mathrm{ct}_2} i_{\mathrm{ct}_2} + (-1)^{j-1} B_{v_2} v_{\mathrm{b}} \\ v_{\mathrm{s}_{2j}} &= C_{\mathrm{tf}_2} w_{\mathrm{tf}_{2j}}, \end{aligned} \qquad j = 1,2,3,4 \tag{6.4}$$

where $M_{\mathrm{tf}_{2j}} = M_{\mathrm{tf}_{1j}}$, $A_{\mathrm{tf}_2} = A_{\mathrm{tf}_1}$, $B_{\mathrm{ct}_2} = B_{\mathrm{ct}_1}$, $B_{v_2} = B_v$, and $C_{\mathrm{tf}_2} = C_{\mathrm{tf}_1}$ since the control and primary sense transformers are identical and analogous states are used to describe the dynamics of each transformer. The center tap current, $i_{\mathrm{ct}_2} = a_{\mathrm{ct}_2}\cos(\omega_{\mathrm{s}} t)$, has an amplitude of 15.7 mA. The dynamics of all eight transformers (the supply transformers that produce the center tap currents are not modeled) are collectively governed by the seven-input/four-output system

$$\begin{aligned} M_{\mathrm{tf}}(q)\dot{w}_{\mathrm{tf}} &= A_{\mathrm{tf}} w_{\mathrm{tf}} + B_{\mathrm{ct}} i_{\mathrm{ct}} + B_{\mathrm{c}} v_{\mathrm{c}} + B_{\mathrm{b}} v_{\mathrm{b}} \\ v_{\mathrm{s}} &= C_{\mathrm{tf}} w_{\mathrm{tf}}, \end{aligned} \tag{6.5}$$

whose inputs, i_{ct}, v_{c}, and v_{b}, and output, v_{s}, are

$$i_{\mathrm{ct}} = \begin{bmatrix} i_{\mathrm{ct}_1} \\ i_{\mathrm{ct}_2} \end{bmatrix}, \quad v_{\mathrm{c}} = \begin{bmatrix} v_{\mathrm{c}_1} \\ \vdots \\ v_{\mathrm{c}_4} \end{bmatrix}, \quad v_{\mathrm{b}} = k_{\mathrm{c}} \cos(\omega_{\mathrm{s}} t + \psi_{\mathrm{b}}) u_{\mathrm{b}}, \quad v_{\mathrm{s}} = \begin{bmatrix} v_{\mathrm{s}_1} \\ \vdots \\ v_{\mathrm{s}_4} \end{bmatrix},$$

where u_{b} is the DSP-generated signal that sets the bias amplitude and ψ_{b} is the bias modulation phase. Each of sense voltages, $v_{\mathrm{s}_{ij}}$, has been relabeled so that the "i" in the subscript "ij" is dropped, i.e., $[v_{\mathrm{s}_1}\ v_{\mathrm{s}_2}\ v_{\mathrm{s}_3}\ v_{\mathrm{s}_4}]^T = [v_{\mathrm{s}_{21}}\ v_{\mathrm{s}_{22}}\ v_{\mathrm{s}_{23}}\ v_{\mathrm{s}_{24}}]^T$. The state vector in (6.5) is given by $w_{\mathrm{tf}} = [w_{\mathrm{tf}_{11}}\ \ldots\ w_{\mathrm{tf}_{14}}\ w_{\mathrm{tf}_{21}}\ \ldots\ w_{\mathrm{tf}_{24}}]^T$ and the aggregate state-space matrices are

$$\begin{aligned} M_{\mathrm{tf}}(q) &= \mathrm{diag}\left(M_{\mathrm{tf}_{11}}, M_{\mathrm{tf}_{12}}, M_{\mathrm{tf}_{13}}, M_{\mathrm{tf}_{14}}, M_{\mathrm{tf}_{21}}, M_{\mathrm{tf}_{22}}, M_{\mathrm{tf}_{23}}, M_{\mathrm{tf}_{24}}\right) \in \mathbb{R}^{152\times 152} \\ A_{\mathrm{tf}} &= \mathrm{diag}\left(A_{\mathrm{tf}_1}, A_{\mathrm{tf}_1}, A_{\mathrm{tf}_1}, A_{\mathrm{tf}_1}, A_{\mathrm{tf}_2}, A_{\mathrm{tf}_2}, A_{\mathrm{tf}_2}, A_{\mathrm{tf}_2}\right) \in \mathbb{R}^{152\times 152} \\ C_{\mathrm{tf}} &= \mathrm{diag}\left(C_{\mathrm{tf}_2}, C_{\mathrm{tf}_2}, C_{\mathrm{tf}_2}, C_{\mathrm{tf}_2}\right) \in \mathbb{R}^{4\times 152} \end{aligned}$$

$$B_{\mathrm{ct}} = \begin{bmatrix} B_{\mathrm{ct}_1} & 0 \\ -B_{\mathrm{ct}_1} & 0 \\ B_{\mathrm{ct}_1} & 0 \\ -B_{\mathrm{ct}_1} & 0 \\ 0 & B_{\mathrm{ct}_2} \\ 0 & -B_{\mathrm{ct}_2} \\ 0 & B_{\mathrm{ct}_2} \\ 0 & -B_{\mathrm{ct}_2} \end{bmatrix} \in \mathbb{R}^{152\times 2}, \quad B_{\mathrm{c}} = \begin{bmatrix} B_v & 0 & 0 & 0 \\ 0 & B_v & 0 & 0 \\ 0 & 0 & B_v & 0 \\ 0 & 0 & 0 & B_v \\ 0 & 0 & 0 & 0 \\ 0 & 0 & 0 & 0 \\ 0 & 0 & 0 & 0 \\ 0 & 0 & 0 & 0 \end{bmatrix} \in \mathbb{R}^{152\times 4},$$

$$B_{\mathrm{b}} = \begin{bmatrix} 0 & 0 & 0 & 0 & B_{v_2} & -B_{v_2} & B_{v_2} & -B_{v_2} \end{bmatrix}^T \in \mathbb{R}^{152\times 1}.$$

The remaining analog filtering dynamics are not reviewed as the only updates are the result of the change in the sense carrier frequency and demodulation phases.

The linearization and discretization framework described in Section 2.2.5 is applied and a four-input/four-output linear time-invariant discrete-time model, G, is generated. The control input required for suspension about the disk's nominal setpoint, $\bar{u}$, is equal to 1.26 V in each element and the DC bias signal generated by the DSP, u_{b}, is also 1.26 V. The model

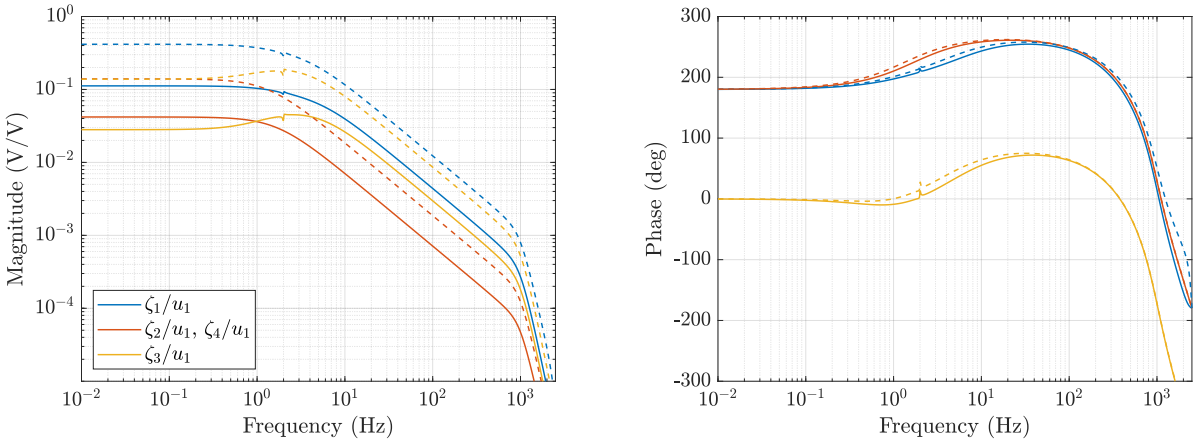

Figure 6.2: Frequency response of the analytical model from the perspective of u_1. The model developed in Section 4.1 for the previous electrode configuration is shown by the dashed traces for comparison.

consists of 82 states: 8 for the smoothing filters, 48 associated with the transformers, 10 for the disk dynamics, and 16 associated with the anti-alias filters. This model contains the DC feedthrough that must be removed prior to controller design. A constant gain feedforward filter, F, that operates in parallel to G is identified to cancel the feedthrough. This filter is considered internal to the plant, P, so that $P = G - F$. The feedthrough-compensated signal is denoted $\zeta = [\zeta_1\ \zeta_2\ \zeta_3\ \zeta_4]^T$ and a frequency response of u_1 to ζ is plotted in Figure 6.2. The remaining input/output channels are easily identified from the system's symmetry. For comparison, the frequency response of u_1 to ζ using the previous electrode arrangement is shown by the dashed lines in the figure. Similar trends are observed, however, the gain is approximately $4\times$ lower with the updated electrodes. This is expected since the sensing and actuation electrode areas have both decreased by a factor of nearly two, reducing both the control authority and measurement amplitude. Furthermore, the unstable eigenvalues of the plant, $\lambda_1 = 1.0021$ and $\lambda_2 = \lambda_3 = 1.066$ (corresponding to 10.7 and 33.0 rad/s continuous time), have shifted up in frequency.

6.2 Robustly Stabilizing Controller

A controller is synthesized to maximize the closed-loop stability margin to coprime factor perturbations of the shaped plant, P_s. Details of the controller synthesis technique are described in Section 4.2. The shaping filter is a scaling of the open loop plant, $P_s = 15P$, so that the three nonzero singular values of the shaped plant, shown in Figure 6.3, cross over between 3 and 10 Hz. Only two traces are shown in the figure since $\sigma_2(P_s) = \sigma_3(P_s)$ below 1.2 Hz and $\sigma_1(P_s) = \sigma_2(P_s)$ above 1.2 Hz. With the selected weight, $\gamma_{\min} \approx 1.9$ and a controller is synthesized for the suboptimal problem $\gamma = 1.1 \times \gamma_{\min}$ according to (4.15). The controller order is 82, though a balanced truncation of dimension 3 approximates the controller with little error. The plant shaping weight is absorbed into the feedback controller and negative feedback convention is employed. The output loop gain singular values with the reduced-order controller are included in Figure 6.3, along with the maximum singular values of the output sensitivity and complementary sensitivity functions. With the reduced-order controller, the closed-loop system is robust to coprime factor perturbations bounded by 0.45. Furthermore, the norm of both the input and output complementary sensitivity functions is 1.6, demonstrating that the closed-loop system is robust to large unstructured multiplicative uncertainty at both the plant input and output.

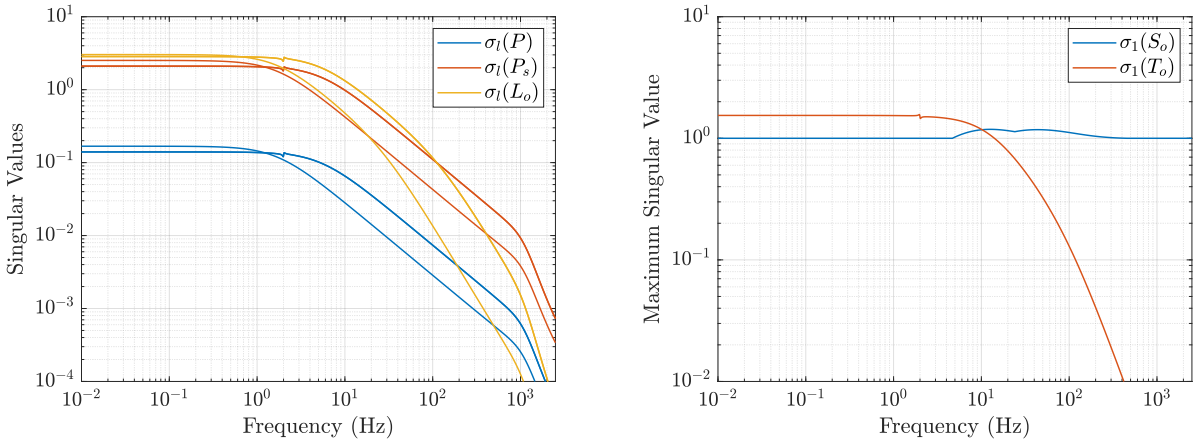

Figure 6.3: Left: Singular values of the plant, P, shaped plant, P_s, and output loop gain, L_o. Right: Maximum singular values of the predicted output sensitivity and output complementary sensitivity functions.

CHAPTER 7

Five-Degree-of-Freedom Disk

This chapter presents an analytical model for the 41 mm radius disk using the new electrode configuration and develops two unique stabilizing controllers. The electrode-disk geometry for this configuration results in weak fringe field forces, thus lateral motion of the disk must be regulated. The lateral electrodes ($i = 3$ electrodes in Figure 5.1) are reconnected to provide measurements of in-plane motion of the disk.

7.1 Analytical Model

Developing a model for the larger disk with the updated electrodes follows the framework used for the three previous electrode-disk configurations so the details of the disk and transformer dynamics are only quickly reviewed. A free body diagram of the disk is pictured in Figure 7.1. The same forces and moments are present as previous configurations: the omittance of the fringe field spring force is consistent with the weak electrical fringing effect on the larger disk. The yaw degree of freedom is neglected from the model and the disk's translational degrees of freedom are governed by

$$\begin{aligned} m\ddot{x} &= -c_x\dot{x} + \varphi \sum_{i,j} F_{\mathrm{n}_{ij}} \\ m\ddot{y} &= -c_y\dot{y} - \theta \sum_{i,j} F_{\mathrm{n}_{ij}} \qquad\qquad i = 1,2,3 \\ m\ddot{z} &= -c_z\dot{z} - ma_{\mathrm{g}} + \sum_{i,j} F_{\mathrm{n}_{ij}}. \qquad\qquad j = 1,2,3,4 \end{aligned} \tag{7.1}$$

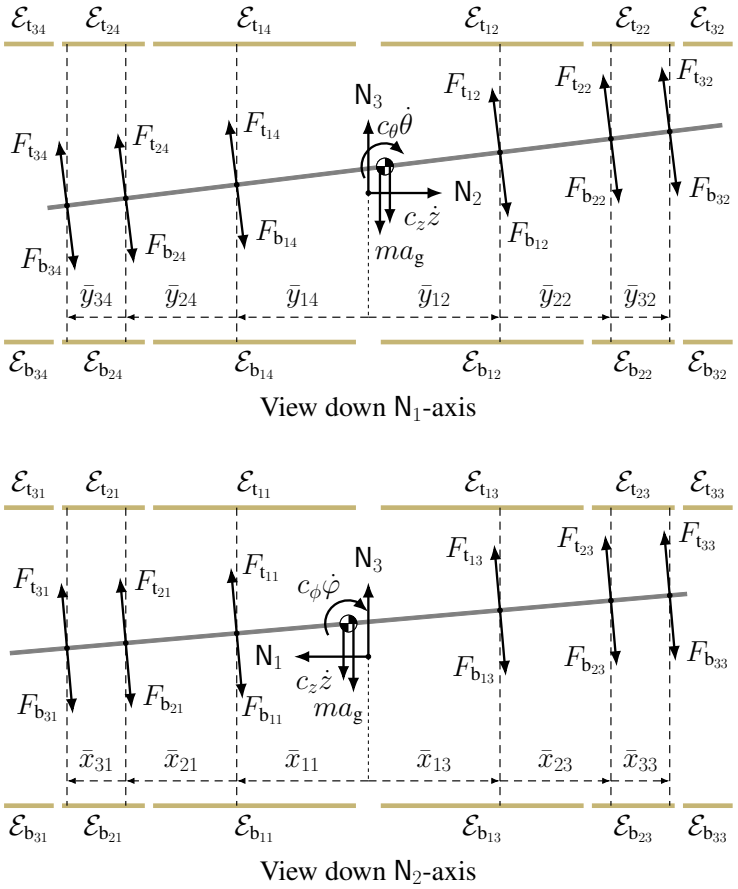

Figure 7.1: Free body diagram of the larger disk with the updated electrodes. Electrical fringe field forces are negligible for small deviations of the disk from its nominal position, thus, equivalent spring forces representative of fringing are omitted.

Meanwhile, the equations of motion for the pitch and roll degrees of freedom are

$$\begin{aligned} J_{\mathrm{t}}\ddot{\theta} &= -c_\theta\dot{\theta} + 2\left(J_{\mathrm{t}} - J_{\mathrm{s}}\right)\varphi\dot{\theta}\dot{\varphi} + \sum_{i,j}\left(\bar{y}_{ij} - y\right)F_{\mathrm{n}_{ij}} && i = 1,2,3 \\ J_{\mathrm{t}}\ddot{\varphi} &= -c_\varphi\dot{\varphi} + \left(J_{\mathrm{s}} - J_{\mathrm{t}}\right)\varphi\dot{\theta}^2 + \sum_{i,j}\left(x - \bar{x}_{ij}\right)F_{\mathrm{n}_{ij}}. && j = 1,2,3,4 \end{aligned} \tag{7.2}$$

The transformer dynamics for the control and primary sense electrodes are identical to those in Chapter 6. The lateral electrodes, however, were absent there, and the transformers for these electrodes are modeled on the non-idealized transformer of Figure 2.9. All currents and voltages present, except for the center tap current input, are collected in the 18-state

vector $w_{\mathrm{tf}_{3j}}$ and the lateral electrode transformers are governed by

$$\begin{aligned} M_{\mathrm{tf}_{3j}}(q)\dot{w}_{\mathrm{tf}_{3j}} &= A_{\mathrm{tf}_3} w_{\mathrm{tf}_{3j}} + (-1)^{j-1} B_{\mathrm{ct}_3} i_{\mathrm{ct}_3} \\ v_{\mathrm{s}_{3j}} &= C_{\mathrm{tf}_3} w_{\mathrm{tf}_{3j}}. \end{aligned} \qquad j = 1, 2 \tag{7.3}$$

The center tap current, $i_{\mathrm{ct}_3} = a_{\mathrm{ct}_3} \cos(\omega_{\mathrm{s}} t)$, has an amplitude of 2.5 mA. The dynamics of all ten electrode transformers are collectively governed by the eight-input/six-output system

$$\begin{aligned} M_{\mathrm{tf}}(q)\dot{w}_{\mathrm{tf}} &= A_{\mathrm{tf}} w_{\mathrm{tf}} + B_{\mathrm{ct}} i_{\mathrm{ct}} + B_{\mathrm{c}} v_{\mathrm{c}} + B_{\mathrm{b}} v_{\mathrm{b}} \\ v_{\mathrm{s}} &= C_{\mathrm{tf}} w_{\mathrm{tf}}, \end{aligned} \tag{7.4}$$

whose inputs, i_{ct}, v_{c}, and v_{b}, and output, v_{s}, are

$$i_{\mathrm{ct}} = \begin{bmatrix} i_{\mathrm{ct}_1} \\ i_{\mathrm{ct}_2} \\ i_{\mathrm{ct}_3} \end{bmatrix}, \quad v_{\mathrm{c}} = \begin{bmatrix} v_{\mathrm{c}_1} \\ \vdots \\ v_{\mathrm{c}_4} \end{bmatrix}, \quad v_{\mathrm{b}} = k_{\mathrm{c}} \cos(\omega_{\mathrm{s}} t + \psi_{\mathrm{b}}) u_{\mathrm{b}}, \quad v_{\mathrm{s}} = \begin{bmatrix} v_{\mathrm{s}_1} \\ \vdots \\ v_{\mathrm{s}_6} \end{bmatrix},$$

where the sense voltages, $v_{\mathrm{s}_{ij}}$, have been relabeled according to

$$\begin{bmatrix} v_{\mathrm{s}_1} & v_{\mathrm{s}_2} & v_{\mathrm{s}_3} & v_{\mathrm{s}_4} & v_{\mathrm{s}_5} & v_{\mathrm{s}_6} \end{bmatrix}^T = \begin{bmatrix} v_{\mathrm{s}_{21}} & v_{\mathrm{s}_{22}} & v_{\mathrm{s}_{23}} & v_{\mathrm{s}_{24}} & v_{\mathrm{s}_{31}} & v_{\mathrm{s}_{32}} \end{bmatrix}^T.$$

The state vector in (7.4) is given by

$$w_{\mathrm{tf}} = \begin{bmatrix} w_{\mathrm{tf}_{11}} & \dots & w_{\mathrm{tf}_{14}} & w_{\mathrm{tf}_{21}} & \dots & w_{\mathrm{tf}_{24}} & w_{\mathrm{tf}_{31}} & w_{\mathrm{tf}_{32}} \end{bmatrix}^T$$

and the aggregate state-space matrices are

$$\begin{aligned} M_{\mathrm{tf}}(q) &= \mathrm{diag}\left(M_{\mathrm{tf}_{11}}, M_{\mathrm{tf}_{12}}, M_{\mathrm{tf}_{13}}, M_{\mathrm{tf}_{14}}, M_{\mathrm{tf}_{21}}, M_{\mathrm{tf}_{22}}, M_{\mathrm{tf}_{23}}, M_{\mathrm{tf}_{24}}, M_{\mathrm{tf}_{31}}, M_{\mathrm{tf}_{32}}\right) \\ A_{\mathrm{tf}} &= \mathrm{diag}\left(A_{\mathrm{tf}_1}, A_{\mathrm{tf}_1}, A_{\mathrm{tf}_1}, A_{\mathrm{tf}_1}, A_{\mathrm{tf}_2}, A_{\mathrm{tf}_2}, A_{\mathrm{tf}_2}, A_{\mathrm{tf}_2}, A_{\mathrm{tf}_3}, A_{\mathrm{tf}_3}\right) \\ C_{\mathrm{tf}} &= \mathrm{diag}\left(C_{\mathrm{tf}_2}, C_{\mathrm{tf}_2}, C_{\mathrm{tf}_2}, C_{\mathrm{tf}_2}, C_{\mathrm{tf}_3}, C_{\mathrm{tf}_3}\right) \\ B_{\mathrm{b}} &= \begin{bmatrix} 0 & 0 & 0 & 0 & B_{v_2} & -B_{v_2} & B_{v_2} & -B_{v_2} & 0 & 0 \end{bmatrix}^T, \end{aligned}$$

$$B_{\mathrm{ct}} = \begin{bmatrix} B_{\mathrm{ct}_1} & 0 & 0 \\ -B_{\mathrm{ct}_1} & 0 & 0 \\ B_{\mathrm{ct}_1} & 0 & 0 \\ -B_{\mathrm{ct}_1} & 0 & 0 \\ 0 & B_{\mathrm{ct}_2} & 0 \\ 0 & -B_{\mathrm{ct}_2} & 0 \\ 0 & B_{\mathrm{ct}_2} & 0 \\ 0 & -B_{\mathrm{ct}_2} & 0 \\ 0 & 0 & B_{\mathrm{ct}_3} \\ 0 & 0 & -B_{\mathrm{ct}_3} \end{bmatrix}, \quad B_{\mathrm{c}} = \begin{bmatrix} B_v & 0 & 0 & 0 \\ 0 & B_v & 0 & 0 \\ 0 & 0 & B_v & 0 \\ 0 & 0 & 0 & B_v \\ 0 & 0 & 0 & 0 \\ 0 & 0 & 0 & 0 \\ 0 & 0 & 0 & 0 \\ 0 & 0 & 0 & 0 \\ 0 & 0 & 0 & 0 \\ 0 & 0 & 0 & 0 \end{bmatrix}.$$

The analog filtering dynamics follow those of Chapter 6. The additional lateral measurements, v_{s_5} and v_{s_6}, are demodulated with the phase-shifted sense carrier (whose phase is selected to maximize the measurement signals relative to lateral motion of the disk) and the signal conditioning gain of 6.3 matches the gain reported in Section 2.2.4.

A linear four-input/six-output time-invariant discrete-time model is approximated from the time-periodic nonlinear equations of motion using the procedure reported in Section 2.2.5. The DSP-generated control inputs and bias voltage necessary to suspend the disk at its nominal setpoint are each 1.53 V and the model order is 102. The four-input/six-output frequency response of the model, whose input is $u = [u_1\ u_2\ u_3\ u_4]^T$ and output is $g = [g_1\ g_2\ g_3\ g_4\ g_5\ g_6]^T$, is computed and shown by the solid lines in Figure 7.2 from the perspective of input u_1. The sampled signal, g, contains DC actuator-to-pick-off feedthrough, thus it does not appear on the logarithmic frequency response plots, i.e., the feedthrough-compensated signal, $\zeta = [\zeta_1\ \zeta_2\ \zeta_3\ \zeta_4\ \zeta_5\ \zeta_6]^T$, is equivalent to g for $\omega \neq 0$. The DC feedthrough is compensated by a constant gain feedforward filter that operates in parallel to the system. This feedforward filter is considered internal to the plant, P, whose input and output are u and ζ, respectively. The symmetry of the system makes identifying the frequency responses of the remaining input/output channels trivial. The frequency response of plant using the electrode configuration from Part I is included in Figure 7.2 for comparison. Similar trends are observed,

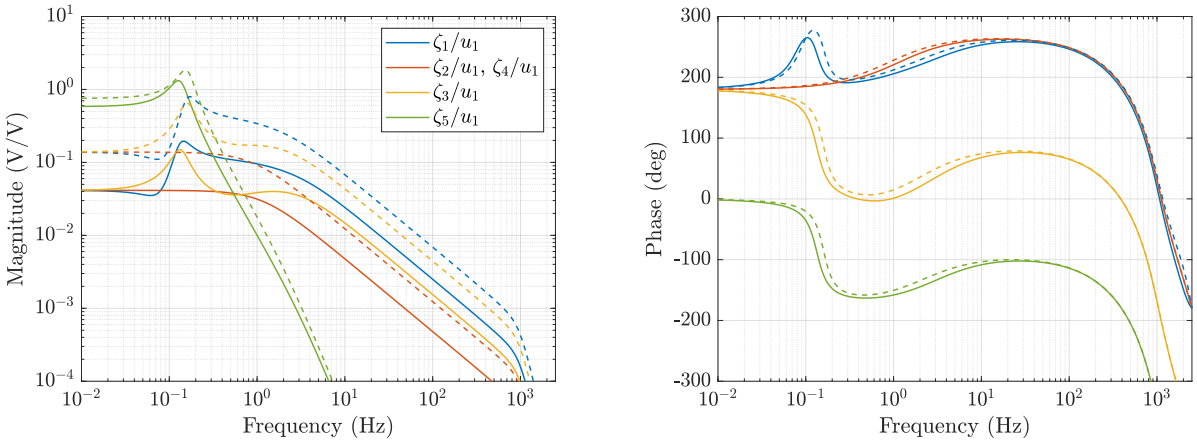

Figure 7.2: Frequency response of the analytical model from the perspective of u_1. The feedthrough-compensated model presented in Section 2.2.6 for the larger disk with the previous electrode configuration is shown by the dashed traces for comparison.

however, the gain is markedly lower with the updated electrodes. This is expected due to the reduced control authority and signal amplitude that results from decreased electrode areas, as well as the increased carrier frequency of the sense signals. The unstable eigenvalues of the plant, given in discrete-time as $\lambda_1 = 1.0015$ and $\lambda_2 = \lambda_3 = 1.037$ (corresponding to 7.27 and 18.7 rad/s continuous time), have increased in frequency from those of the initial electrode configuration. The three nonzero singular values of the plant are graphed in Figure 7.3. Only two traces are evident because $\sigma_1(P) = \sigma_2(P)$.

7.2 Initial Controller Design

The first controller synthesis technique investigated follows that of the previous electrode-disk configurations, where the controller is designed to maximize the closed-loop stability margin to coprime factor perturbations of the shaped plant (see Section 4.2 for details). The

post-compensation filter,

$$W_2 = \begin{bmatrix} 15 & 0 & 0 & 0 & 0 & 0 \\ 0 & 15 & 0 & 0 & 0 & 0 \\ 0 & 0 & 15 & 0 & 0 & 0 \\ 0 & 0 & 0 & 15 & 0 & 0 \\ 0 & 0 & 0 & 0 & 1 & 0 \\ 0 & 0 & 0 & 0 & 0 & 1 \end{bmatrix}, \tag{7.5}$$

is designed so that the three nonzero singular values of the shaped plant, $P_s = W_2 P$, shown in Figure 7.3, cross over between 2 and 10 Hz. Only two traces are visible in the figure because $\sigma_2(P_s) = \sigma_3(P_s)$ at low frequencies and $\sigma_1(P_s) = \sigma_2(P_s)$ near and above the resonance. For the shaped plant, $\gamma_{\min} \approx 2.0$ and a controller is synthesized for the suboptimal problem $\gamma = 1.1 \times \gamma_{\min}$ according to (4.15). The controller order is 102, though a balanced truncation reduces the controller dimension to 7 with little frequency response error. The reduced-order controller contains two unstable poles at 1.45 rad/s making implementation difficult in practice. Nevertheless, the closed-loop system is robust to coprime factor perturbations bounded by 0.45. The maximum singular values of the input and output sensitivity and complementary sensitivity functions using the 7-state controller are included in Figure 7.3. The norms of the input and output complementary sensitivity functions are 1.6 and

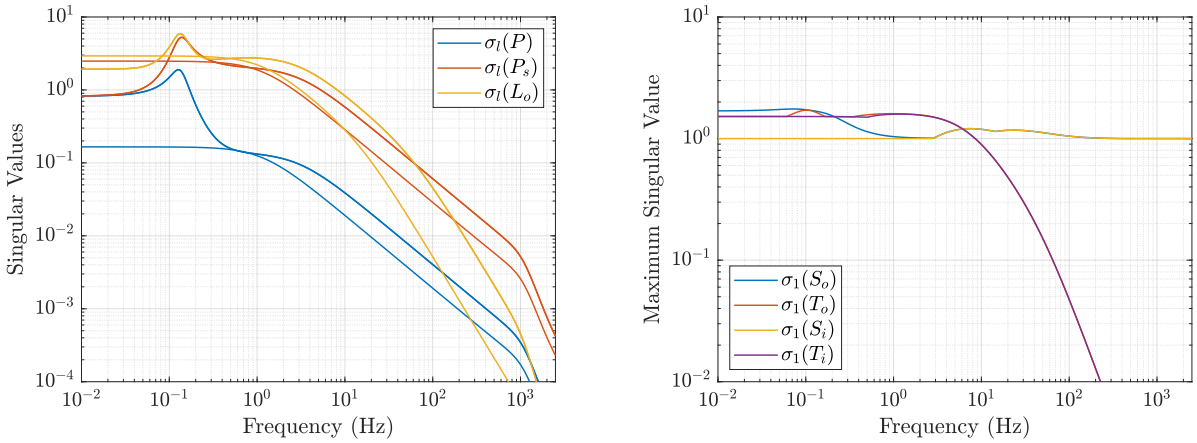

Figure 7.3: Left: Singular values of the plant, P, shaped plant, P_s, and output loop gain, L_o. Right: Maximum singular values of the predicted input and output sensitivity and complementary sensitivity functions.

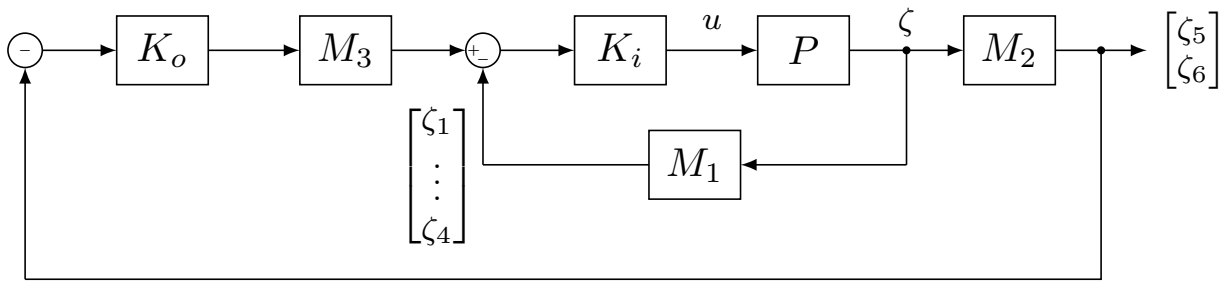

Figure 7.4: Cascade control schematic for suspension of the larger disk.

1.7, respectively, demonstrating that the closed-loop system is robust to large unstructured multiplicative uncertainty at both the plant input and output.

7.3 Stable Controller Design

A stable feedback controller is designed to stabilize the closed-loop system as an alternative to the unstable controller presented in Section 7.2. Stability margins to coprime factor perturbations and multiplicative uncertainty at the plant output are vastly reduced from the prior section, however, controller implementation, especially upon start-up, becomes significantly easier. A cascade feedback architecture is employed, as shown in Figure 7.4. The inner loop is designed to regulate the vertical position, roll, and pitch degrees of freedom using the primary sense electrode measurements, meanwhile the outer loop uses the lateral electrode measurements to specify the tilt references. The M_1, M_2, and M_3 matrices are given by

$$M_1 = \begin{bmatrix} I_4 & 0 \end{bmatrix} \in \mathbb{R}^{4\times 6}, \quad M_2 = \begin{bmatrix} 0 & I_2 \end{bmatrix} \in \mathbb{R}^{2\times 6}, \quad M_3 = \begin{bmatrix} I_2 \\ -I_2 \end{bmatrix} \in \mathbb{R}^{4\times 2}, \tag{7.6}$$

where I_2 and I_4 are the 2×2 and 4×4 identity matrices, respectively, and the "0" blocks are appropriately dimensioned so that M_1 picks off the first four elements of ζ and M_2 picks off ζ_5 and ζ_6. The M_3 matrix converts the lateral measurements into angular references using the fact that the tilt and lateral degrees of freedom are coupled.

The inner loop controller is a constant gain: $K_i = 50$. Closing the inner loop stabilizes the vertical degree of freedom, however, two (tilt) instabilities remain at 0.22 rad/s. The

outer loop controller, K_o, is a diagonal phase lead filter,

$$K_o = -25\frac{s+1.41}{s+28.1}I_2.$$

Closing the loop around K_o stabilizes the closed-loop system –all eigenvalues of the closed-loop system have real part strictly less than -1.75. The inner and outer controllers, as well as the M_1, M_2, and M_3 matrices can be absorbed into a single controller, K, according to

$$K = K_i\left(M_3 K_o M_2 + M_1\right). \tag{7.7}$$

The simplified feedback architecture of the closed-loop system using K, shown in Figure 7.5, is used to evaluate closed-loop stability margins. The norms of the input and output complementary sensitivity functions are shown in Figure 7.6, and demonstrate that the closed-loop system is not robust to unstructured uncertainty at the plant output. Furthermore, poor robustness to coprime factor perturbations are exhibited with the stable controller.

Considering the sources of uncertainty present in the system –electrode misalignment, plate warpage, transduction gains, viscous damping, photoresist thickness, center tap current estimation, etc. –unstructured uncertainty is overly conservative for the disk system. Sources of error that produce perturbations to the electrode-disk gaps primarily manifest in the four measurements $\{\zeta_1, \zeta_2, \zeta_3, \zeta_4\}$. Similarly, sources of uncertainty in the lateral measurements, ζ_5 and ζ_6, are not expected to couple to $\{\zeta_1, \zeta_2, \zeta_3, \zeta_4\}$. Thus, the structured singular value is used to analyze the robustness of the closed-loop system to structured multiplicative uncertainty at the plant output of the form

$$\Delta = \begin{bmatrix} \Delta_4 & 0 \\ 0 & \Delta_2 \end{bmatrix}. \tag{7.8}$$

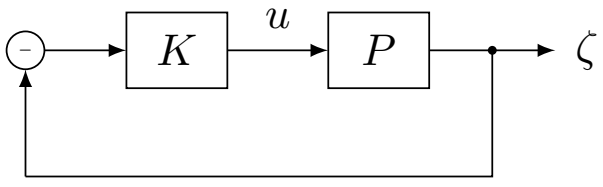

Figure 7.5: Simplified feedback schematic of the cascade controller. The controller, K, is given in (7.7) and is a function of the inner and outer loop controllers.

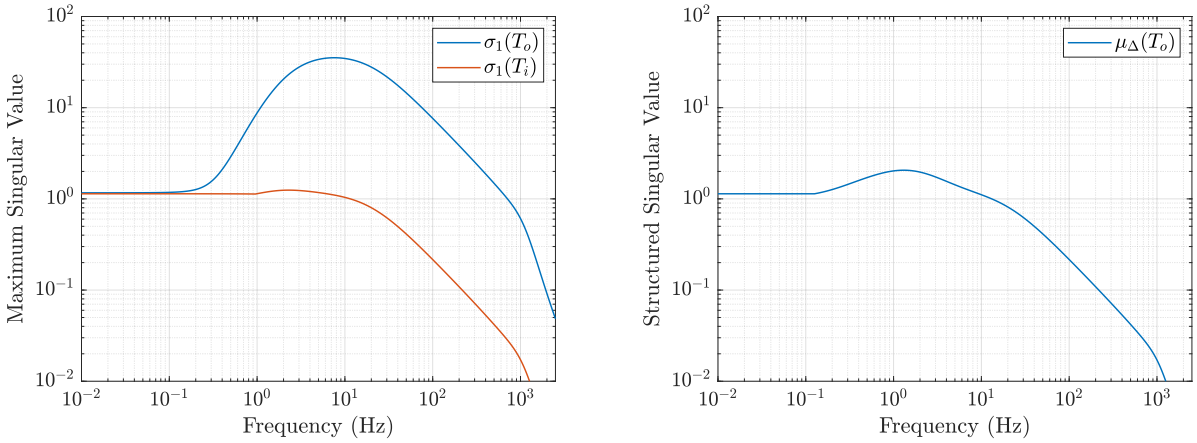

Figure 7.6: Left: Maximum singular values of the input and output complementary sensitivity functions. Right: Structured singular value of the output complementary sensitivity function.

The structured singular value, $\mu_\Delta(T_o)$, is defined as the reciprocal of the norm of smallest Δ that causes the matrix $I - T_o\Delta$ to become singular (see [SP05], for example). For the disk system using the stable controller, the norm of the smallest destabilizing multiplicative output perturbation, or $\mu_\Delta(T_o)^{-1}$, for the structured uncertainty in (7.8) is shown to be 0.48 in Figure 7.6, indicating that the closed-loop system is robustly stable to such uncertainty. Thus, the poor robustness margins to unstructured uncertainty at the plant output can be attributed to off-diagonal coupling that is improbable given knowledge of the modeling assumptions made and physical sources of error present in the system. Furthermore, it can be argued that perturbations to the measurements primarily couple in the adjacent channels that share a common center tap supply transformer so the structured uncertainty in (7.8) may still be conservative.

CHAPTER 8

Concluding Remarks

Two systems to electrostatically suspend conductive disks are presented. The dual variants employ similar levitation schemes, however, they differ in electrode arrangement –the first system uses common electrodes for both actuation and sensing, while the second system segregates the control and measurement electronics. A modeling framework is developed and applied to both systems and can easily be expanded to additional electrode-disk geometries. The notation ("ij" subscript) used for the electrode-disk gaps, capacitances, and electrostatic forces is designed with numerical computing in mind so that $i \times j$-dimensioned matrices can be initialized and element-by-element calculations performed. A family of robust multivariable controllers, largely based on normalized coprime factorizations of the analytical models generated, are synthesized using loop-shaping techniques. Stability margins to input and output multiplicative uncertainty and perturbations of the plant's normalized coprime factors are evaluated. Two disk sizes are investigated and an empirical model of the suspended smaller disk, which requires active stabilization of the vertical, pitch, and roll degrees of freedom, is captured for the first electrode configuration from closed-loop measurements. The analytical model compares favorably to the experimental results and a novel parametric identification technique fits a 22-state model with little frequency response error to the open-loop unstable plant. The identified model characterizes three unstable modes, whose input/output directions are used to transform the measurements into new signals proportional to the disk's vertical, pitch, and roll degrees of freedom. These directions provide insights into transduction asymmetries. A representation of the transformed plant is used to synthesize an updated controller with improved disturbance rejection and regulation. Sensor noise is quantified to confirm that the disk's vertical position and tilt angles are measured

with high accuracy, making the system a suitable prototype for manipulating micro-scale devices in a non-contact manner. Redundant use of the electrodes for actuation and sensing presents significant feedthrough coupling from the control inputs to the electronic pick-offs. This coupling is mitigated by a digital feedforward filter, nonetheless, residual feedthrough is evident in the experimental data. The second electrode arrangement is designed to eliminate this feedthrough, however, this comes at the cost of diminishing the motional gain of the plant: splitting the electrodes decreases sensitivity to disk motion and reduces control authority. The updated electrode configuration has been fabricated and assembled, though testing has not commenced. Thus, only analytical models and preliminary controller designs are presented for the two disks with this system. Stabilization of the two disks with the new electrodes is the immediate focus of the next phase of research.

In addition to testing the new system, the work herein presents several research opportunities that should be examined prior to miniaturization to the MEMS-scale for the suspension of micro-resonators. An improved estimate of the fringe field electrostatic forces in the analytical model is one topic of future inquiry. The lateral degrees of freedom are passively stabilized by these forces. Although well-damped at atmospheric pressure, these modes will feature much more prominently in the plant frequency response when the system in operated in vacuo, thus, accurate estimates of their modal frequencies are necessary for designing the initial controller. Effective lateral spring rates can be obtained from numerical techniques that include the disk and electrode geometries. Another direction of future research is to identify the measurement noise sources in the suspension electronics. A more fundamental understanding of the noise sources will be useful in predicting measurement uncertainty in new electrostatic suspension designs. Furthermore, while the differential capacitance transduction yields low-noise measurements, calibration of the electrode pairs must still be carried out to map the disk position to the pick-off voltages. Calibration will also yield updated scale factors since the noise spectra reported herein use scale factors estimated from the analytical model. Finally, electrode redesigns should auto-align the upper and lower electrode plates to reduce misalignment uncertainty.

APPENDIX A

Electrode-Disk Overlap Geometry

A simplified diagram of the electrode-disk overlap areas for a given annular electrode index, i, is shown in Figure A.1, where the gold shaded regions represent the overlap areas. It is assumed that the areas are dependent only on the electrode-disk geometry and the lateral position of the disk. Any angular rotations of the disk are assumed to have negligible effects on the overlap areas due to the angular constraints imposed by the shim spacers, therefore, this appendix views the system from a planar perspective.

A new coordinate-frame, the C-frame, is defined by a -45° rotation about the N_3-axis. This coordinate transformation is performed to simplify the computations by placing each electrode entirely within a single quadrant. The rotation matrix from the N-frame to the C-frame is given by

$$\mathcal{R}_{\mathsf{CN}} = \begin{bmatrix} \cos(-45^\circ) & \sin(-45^\circ) \\ -\sin(-45^\circ) & \cos(-45^\circ) \end{bmatrix}, \tag{A.1}$$

where the colinear N_3- and C_3-directions are omitted due to the planar nature of the problem.

Inner (Primary) Electrodes

For the case of the inner (non-lateral) electrodes, the overlap areas are dependent only on the electrode geometry because the disk completely overlaps these electrodes. Since each of the electrode areas are equal for a given annular index, i, the electrode in quadrant 1 of the C-frame is selected for the computations. The electrode area is calculated by first computing the area of the sector described by the entire shaded region in quadrant 1 (the combined gold and gray regions). The area of the gray sector is then computed and subtracted off.

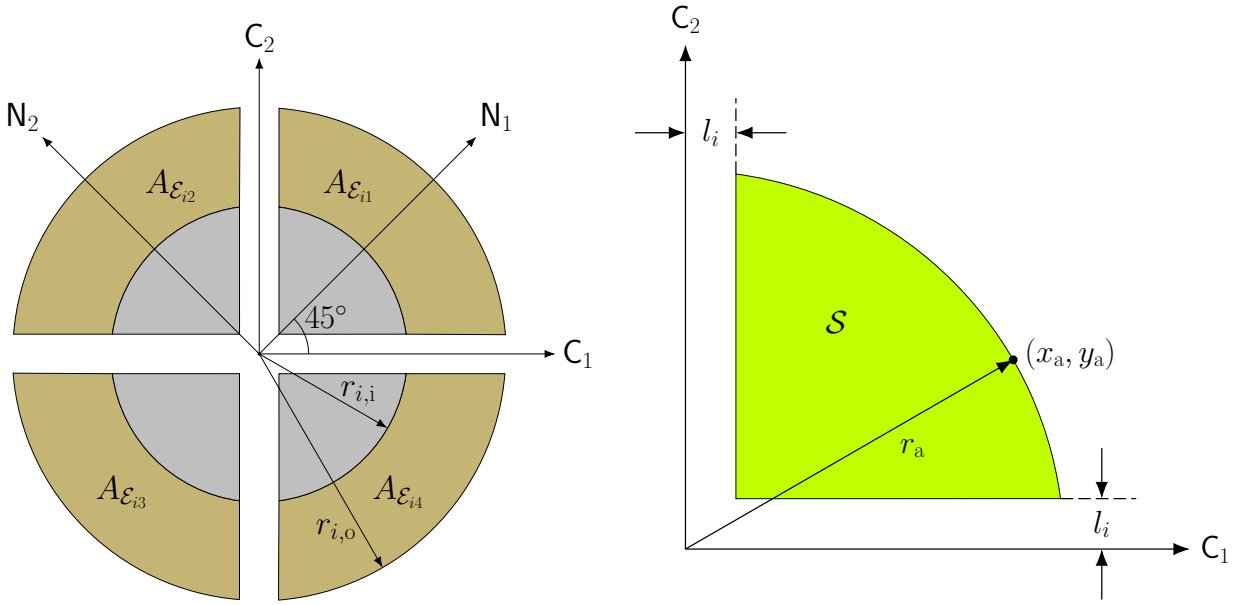

Figure A.1: Left: Schematic of the disk-electrode overlap surfaces, shown in gold. Right: Diagram of a sector used in the area computations.

Note that the shapes of these two surfaces (gray and gold plus gray) are identical –they are quarter circles with thin rectangular gaps removed along the sides. A general surface of this shape is defined as surface $\mathcal{S}$. In the C-frame, the points along the arc of surface $\mathcal{S}$ are given by

$$x_\mathrm{a}^2 + y_\mathrm{a}^2 = r_\mathrm{a}^2, \tag{A.2}$$

where r_a is the arc radius. The area of $\mathcal{S}$ is computed according to

$$\begin{aligned} A_\mathcal{S}(r_\mathrm{a}, l_i) &= \int_{l_i}^{\sqrt{r_\mathrm{a}^2 - l_i^2}} \int_{l_i}^{\sqrt{r_\mathrm{a}^2 - x_\mathrm{a}^2}} dy_\mathrm{a}\, dx_\mathrm{a} \\ &= \int_{l_i}^{\sqrt{r_\mathrm{a}^2 - l_i^2}} \left(\sqrt{r_\mathrm{a}^2 - x_\mathrm{a}^2} - l_i \right) dx_\mathrm{a} \\ &= \int_{l_i}^{\sqrt{r_\mathrm{a}^2 - l_i^2}} \sqrt{r_\mathrm{a}^2 - x_\mathrm{a}^2}\, dx_\mathrm{a} - \int_{l_i}^{\sqrt{r_\mathrm{a}^2 - l_i^2}} l_i\, dx_\mathrm{a}. \end{aligned} \tag{A.3}$$

Integration by substitution is used to solve the integral on the left. Let $x_\mathrm{a} = r_\mathrm{a} \sin(u)$ such that $dx_\mathrm{a} = r_\mathrm{a} \cos(u)\, du$ and note that u is the dummy variable used for u-substitution –it is separate from the control input vector used throughout the body of this dissertation. The use of u in this manner is constrained to this appendix. The integration bounds in the

u-domain are left general because a conversion back to x_a is performed.

$$\begin{aligned}
\int_{l_i}^{\sqrt{r_\mathrm{a}^2-l_i^2}} \sqrt{r_\mathrm{a}^2-x_\mathrm{a}^2}\,dx_\mathrm{a} &= \int_{u_1}^{u_2} r_\mathrm{a}\cos(u)\sqrt{r_\mathrm{a}^2-r_\mathrm{a}^2\sin^2(u)}\,du \\
&= \frac{r_\mathrm{a}^2}{2}\int_{u_1}^{u_2}\left(1+\cos(2u)\right)\,du \\
&= \frac{r_\mathrm{a}^2}{2}\left(u+\frac{1}{2}\sin(2u)\right)\Bigg|_{u_1}^{u_2} \\
&= \frac{r_\mathrm{a}^2}{2}\left(u+\sin(u)\cos(u)\right)\Bigg|_{u_1}^{u_2} \\
&= \frac{r_\mathrm{a}^2}{2}\left(\sin^{-1}\left(\frac{x_\mathrm{a}}{r_\mathrm{a}}\right)+\frac{x_\mathrm{a}}{r_\mathrm{a}}\sqrt{1-\frac{x_\mathrm{a}^2}{r_\mathrm{a}^2}}\right)\Bigg|_{l_i}^{\sqrt{r_\mathrm{a}^2-l_i^2}}
\end{aligned} \tag{A.4}$$

Returning back to the integral in (A.3),

$$A_{\mathcal{S}}(r_\mathrm{a},l_i) = \frac{r_\mathrm{a}^2}{2}\left(\sin^{-1}\left(\frac{x_\mathrm{a}}{r_\mathrm{a}}\right)+\frac{x_\mathrm{a}}{r_\mathrm{a}}\sqrt{1-\frac{x_\mathrm{a}^2}{r_\mathrm{a}^2}}\right) - l_i x_\mathrm{a}\Bigg|_{x_\mathrm{a}=l_i}^{x_\mathrm{a}=\sqrt{r_\mathrm{a}^2-l_i^2}}. \tag{A.5}$$

The electrode area is computed by subtracting the area of the gray sector from the entire shaded sector,

$$A_{\mathcal{E}_{i1}} = A_{\mathcal{S}}(r_{i,\mathrm{o}},l_i) - A_{\mathcal{S}}(r_{i,\mathrm{i}},l_i), \tag{A.6}$$

and the symmetry of the system guarantees that

$$A_{\mathcal{E}_{i1}} = A_{\mathcal{E}_{i2}} = A_{\mathcal{E}_{i3}} = A_{\mathcal{E}_{i4}}. \tag{A.7}$$

The computed values for the electrode-disk areas can be found in Table A.2 for the initial electrode configuration and Table A.3 for the updated electrode arrangement.

The electrode centroids are evaluated by computing the first moments of area and dividing by the electrode area. Only computations in quadrant 1 of the C-frame are performed since the remaining centroids can be easily determined from the symmetry of the system. The

first moment of area in the C_1-direction of sector $\mathcal{S}$ in quadrant 1 is given by

$$\begin{aligned} Q_x(r_\mathrm{a}, l_i) &= \int_{l_i}^{\sqrt{r_\mathrm{a}^2 - l_i^2}} \int_{l_i}^{\sqrt{r_\mathrm{a}^2 - x_\mathrm{a}^2}} y_\mathrm{a}\, dy_\mathrm{a} dx_\mathrm{a} \\ &= \frac{1}{2} \int_{l_i}^{\sqrt{r_\mathrm{a}^2 - l_i^2}} \left(r_\mathrm{a}^2 - x_\mathrm{a}^2 - l_i^2\right) dx_\mathrm{a} \\ &= \frac{1}{2}\left(r_\mathrm{a}^2 - l_i^2\right) x_\mathrm{a} - \frac{1}{6} x_\mathrm{a}^3 \Big|_{x_\mathrm{a}=l_i}^{x_\mathrm{a}=\sqrt{r_\mathrm{a}^2 - l_i^2}} . \end{aligned} \tag{A.8}$$

Similarly, the first moment of area in the C_2-direction of $\mathcal{S}$ in quadrant 1 is computed according to

$$\begin{aligned} Q_y(r_\mathrm{a}, l_i) &= \int_{l_i}^{\sqrt{r_\mathrm{a}^2 - l_i^2}} \int_{l_i}^{\sqrt{r_\mathrm{a}^2 - x_\mathrm{a}^2}} x_\mathrm{a}\, dy_\mathrm{a} dx_\mathrm{a} \\ &= \int_{l_i}^{\sqrt{r_\mathrm{a}^2 - l_i^2}} \left(\sqrt{r_\mathrm{a}^2 - x_\mathrm{a}^2} - l_i\right) x_\mathrm{a}\, dx_\mathrm{a} \\ &= \int_{l_i}^{\sqrt{r_\mathrm{a}^2 - l_i^2}} x_\mathrm{a} \sqrt{r_\mathrm{a}^2 - x_\mathrm{a}^2}\, dx_\mathrm{a} - \int_{l_i}^{\sqrt{r_\mathrm{a}^2 - l_i^2}} l_i x_\mathrm{a}\, dx_\mathrm{a}. \end{aligned} \tag{A.9}$$

Integration by substitution is used to solve the integral on the left. Let $u = r_\mathrm{a}^2 - x_\mathrm{a}^2$ such that $du = -2x_\mathrm{a}\, dx_\mathrm{a}$. Again, the integration bounds in the u-domain are left general since the integral is converted back to the x_a-domain.

$$\begin{aligned} \int_{l_i}^{\sqrt{r_\mathrm{a}^2 - l_i^2}} x_\mathrm{a} \sqrt{r_\mathrm{a}^2 - x_\mathrm{a}^2}\, dx_\mathrm{a} &= \int_{u_1}^{u_2} -\frac{1}{2} u^{1/2}\, du \\ &= -\frac{1}{3} u^{3/2} \Big|_{u_1}^{u_2} \\ &= -\frac{1}{3}\left(r_\mathrm{a}^2 - x_\mathrm{a}^2\right)^{3/2} \Big|_{l_i}^{\sqrt{r_\mathrm{a}^2 - l_i^2}} \end{aligned} \tag{A.10}$$

Substituting the expression in (A.10) into (A.9),

$$Q_y(r_\mathrm{a}, l_i) = -\frac{1}{3}\left(r_\mathrm{a}^2 - x_\mathrm{a}^2\right)^{3/2} - \frac{1}{2} l_i x_\mathrm{a}^2 \Big|_{x_\mathrm{a}=l_i}^{x_\mathrm{a}=\sqrt{r_\mathrm{a}^2 - l_i^2}} . \tag{A.11}$$

The first moment of area in each direction for an electrode is given by the difference between the first moments of area in that direction of the two sectors in Figure A.1 (gold plus gray

and gray), and the centroid in the C-frame, $(\bar{x}_{i1,\mathsf{c}}, \bar{y}_{i1,\mathsf{c}})$, is calculated according to

$$\begin{aligned} \bar{x}_{i1,\mathsf{c}} &= \frac{Q_y(r_{i,\mathrm{o}}, l_i) - Q_y(r_{i,\mathrm{i}}, l_i)}{A_{\mathcal{E}_{i1}}} \\ \bar{y}_{i1,\mathsf{c}} &= \frac{Q_x(r_{i,\mathrm{o}}, l_i) - Q_x(r_{i,\mathrm{i}}, l_i)}{A_{\mathcal{E}_{i1}}}. \end{aligned} \tag{A.12}$$

The rotation matrix $\mathcal{R}_{\mathsf{NC}} = \mathcal{R}_{\mathsf{CN}}^T$ is used to convert the centroids in the C-frame to the N-frame, i.e.,

$$\begin{bmatrix} \bar{x}_{i1} \\ \bar{y}_{i1} \end{bmatrix} = \mathcal{R}_{\mathsf{NC}} \begin{bmatrix} \bar{x}_{i1,\mathsf{c}} \\ \bar{y}_{i1,\mathsf{c}} \end{bmatrix} = \begin{bmatrix} \bar{r}_i \\ 0 \end{bmatrix}, \tag{A.13}$$

and the symmetry of the system results in the electrode centroids

$$(\bar{x}_{ij}, \bar{y}_{ij}) = \begin{cases} (\bar{r}_i, 0) & j = 1 \\ (0, \bar{r}_i) & j = 2 \\ (-\bar{r}_i, 0) & j = 3 \\ (0, -\bar{r}_i) & j = 4. \end{cases} \tag{A.14}$$

Calculated values for the centroids are also provided in Tables A.2 and A.3 for the first and second generation electrode configurations, respectively.

Outer (Lateral) Electrodes

The computations for the electrode-disk overlap areas for the outer (lateral) electrodes are similar to those of the inner electrodes, with the exception that the areas are now also a function of the disk geometry and its lateral position. It is assumed that the disk position is constrained to relatively small translations laterally such that the outer electrode-disk overlap areas always take on a shape whose perimeter consists of two arcs and two straight lines, like that shown in Figure A.1. Large translations that result in the overlap area shape breaking down, i.e., a perimeter defined by two arcs and a single straight line, are not allowed. A new surface, $\tilde{\mathcal{S}}_j$, is defined that is similar in shape to $\mathcal{S}$ in Figure A.1, however, the arc center is not fixed at the origin. The surface $\tilde{\mathcal{S}}_j$ is inscribed within the disk whereby the circumference of the disk constitutes the arc of $\tilde{\mathcal{S}}_j$. Because the disk can move laterally, the

Table A.1: Disk Sector Integration bounds

j	x_{d_1}	x_{d_2}
1	l_i	$x_{\mathsf{c}} + \sqrt{r_{\mathrm{d}}^2 - (l_i - y_{\mathsf{c}})^2}$
2	$x_{\mathsf{c}} - \sqrt{r_{\mathrm{d}}^2 - (l_i - y_{\mathsf{c}})^2}$	$-l_i$
3	$x_{\mathsf{c}} - \sqrt{r_{\mathrm{d}}^2 - (-l_i - y_{\mathsf{c}})^2}$	$-l_i$
4	l_i	$x_{\mathsf{c}} + \sqrt{r_{\mathrm{d}}^2 - (-l_i - y_{\mathsf{c}})^2}$

surface area of $\tilde{\mathcal{S}}_j$ is dependent on the quadrant of interest in the C-frame and is annotated with the "j" subscript accordingly.

The position of the points along the circumference of the disk, $(x_{\mathrm{d}}, y_{\mathrm{d}})$, are given by

$$(x_{\mathrm{d}} - x)^2 + (y_{\mathrm{d}} - y)^2 = r_{\mathrm{d}}^2, \tag{A.15}$$

where (x, y) represents the disk center of mass in the N-frame and r_{d} is the disk radius. The disk center can be converted to the C-frame,

$$\begin{bmatrix} x_{\mathsf{c}} \\ y_{\mathsf{c}} \end{bmatrix} = \mathcal{R}_{\mathsf{CN}} \begin{bmatrix} x \\ y \end{bmatrix}, \tag{A.16}$$

and the position of the points along the circumference can be written as

$$y_{\mathrm{d}} = y_{\mathsf{c}} \pm \sqrt{r_{\mathrm{d}}^2 - (x_{\mathrm{d}} - x_{\mathsf{c}})^2}. \tag{A.17}$$

The area of $\tilde{\mathcal{S}}_j$ is computed beginning with the sectors in quadrants 1 and 2 ($j = 1, 2$), where y_{d} takes on positive values in the C-frame. The upper and lower integration bounds on x_{d} are dependent on j and are provided in Table A.1. These bounds are left general in the calculations that follow so that the equations developed are valid for both $j = 1$ and $j = 2$. To compute the overlap area for the $j = 1$ lateral electrode, for example, use the lower and upper bounds $x_{\mathrm{d}_1} = l_i$ and $x_{\mathrm{d}_2} = x_{\mathsf{c}} + \sqrt{r_{\mathrm{d}}^2 - (l_i - y_{\mathsf{c}})^2}$, respectively, from the table.

$$\begin{aligned} A_{\tilde{\mathcal{S}}_j}(r_{\mathrm{d}}, l_i, x_{\mathsf{c}}, y_{\mathsf{c}}) &= \int_{x_{\mathrm{d}_1}}^{x_{\mathrm{d}_2}} \int_{l_i}^{y_{\mathsf{c}} + \sqrt{r_{\mathrm{d}}^2 - (x_{\mathrm{d}} - x_{\mathsf{c}})^2}} dy_{\mathrm{d}}\, dx_{\mathrm{d}} \\ &= \int_{x_{\mathrm{d}_1}}^{x_{\mathrm{d}_2}} \left[y_{\mathsf{c}} + \sqrt{r_{\mathrm{d}}^2 - (x_{\mathrm{d}} - x_{\mathsf{c}})^2} - l_i \right] dx_{\mathrm{d}} \\ &= \int_{x_{\mathrm{d}_1}}^{x_{\mathrm{d}_2}} (y_{\mathsf{c}} - l_i)\, dx_{\mathrm{d}} + \int_{x_{\mathrm{d}_1}}^{x_{\mathrm{d}_2}} \sqrt{r_{\mathrm{d}}^2 - (x_{\mathrm{d}} - x_{\mathsf{c}})^2}\, dx_{\mathrm{d}} \end{aligned} \tag{A.18}$$

Focusing strictly on the second integral, let $u = x_{\mathrm{d}} - x_{\mathsf{c}}$ such that $du = dx_{\mathrm{d}}$:

$$\int_{x_{\mathrm{d}_1}}^{x_{\mathrm{d}_2}} \sqrt{r_{\mathrm{d}}^2 - (x_{\mathrm{d}} - x_{\mathsf{c}})^2}\, dx_{\mathrm{d}} = \int_{u_1}^{u_2} \sqrt{r_{\mathrm{d}}^2 - u^2}\, du. \tag{A.19}$$

Now let $u = r_{\mathrm{d}} \sin(v)$ so that $du = r_{\mathrm{d}} \cos(v)\, dv$. Note that v is also a dummy variable used to integrate by substitution and is strictly contained to this appendix. It has no correlation to the velocities, voltages, or input/output vectors mentioned throughout this dissertation. The integration bounds on v are left general since a conversion back to the u-domain, and later, x_{d}-domain, is performed.

$$\begin{aligned}
\int_{u_1}^{u_2} \sqrt{r_{\mathrm{d}}^2 - u^2}\, du &= \int_{v_1}^{v_2} r_{\mathrm{d}} \cos(v) \sqrt{r_{\mathrm{d}}^2 - r_{\mathrm{d}}^2 \sin^2(v)}\, dv \\
&= \frac{r_{\mathrm{d}}^2}{2} \int_{v_1}^{v_2} \left(1 + \cos(2v)\right)\, dv \\
&= \frac{r_{\mathrm{d}}^2}{2} \left(v + \frac{1}{2} \sin(2v) \right) \Bigg|_{v_1}^{v_2} \\
&= \frac{r_{\mathrm{d}}^2}{2} \left(v + \sin(v) \cos(v) \right) \Big|_{v_1}^{v_2} \\
&= \frac{r_{\mathrm{d}}^2}{2} \left(\sin^{-1}\left(\frac{u}{r_{\mathrm{d}}} \right) + \frac{u}{r_{\mathrm{d}}} \sqrt{1 - \frac{u^2}{r_{\mathrm{d}}^2}} \right) \Bigg|_{u_1}^{u_2}
\end{aligned} \tag{A.20}$$

Substituting $u = x_{\mathrm{d}} - x_{\mathrm{c}}$ back into the equation, the area of the sector created by the disk is written as

$$A_{\tilde{\mathcal{S}}_j} = (y_{\mathsf{c}} - l_i) x_{\mathrm{d}} + \frac{r_d^2}{2} \left(\sin^{-1}\left(\frac{x_{\mathrm{d}} - x_{\mathsf{c}}}{r_{\mathrm{d}}} \right) + \frac{x_{\mathrm{d}} - x_{\mathsf{c}}}{r_{\mathrm{d}}} \sqrt{1 - \frac{(x_{\mathrm{d}} - x_{\mathsf{c}})^2}{r_{\mathrm{d}}^2}} \right) \Bigg|_{x_{\mathrm{d}_1}}^{x_{\mathrm{d}_2}}, \tag{A.21}$$

where the arguments of the area function have been dropped for concision. Moving on to $j = 3, 4$, of which y_{d} takes on negative values in the C-coordinate frame, the area of the sector established by the disk arc is given by

$$\begin{aligned}
A_{\tilde{\mathcal{S}}_j} &= \int_{x_{\mathrm{d}_1}}^{x_{\mathrm{d}_2}} \int_{y_{\mathsf{c}} - \sqrt{r_{\mathrm{d}}^2 - (x_{\mathrm{d}} - x_{\mathsf{c}})^2}}^{-l_i} dy_{\mathrm{d}}\, dx_{\mathrm{d}} \\
&= \int_{x_{\mathrm{d}_1}}^{x_{\mathrm{d}_2}} \left[-(y_{\mathsf{c}} + l_i) + \sqrt{r_{\mathrm{d}}^2 - (x_{\mathrm{d}} - x_{\mathsf{c}})^2} \right] dx_{\mathrm{d}} \\
&= -(y_{\mathsf{c}} + l_i) x_{\mathrm{d}} + \frac{r_{\mathrm{d}}^2}{2} \left(\sin^{-1}\left(\frac{x_{\mathrm{d}} - x_{\mathsf{c}}}{r_{\mathrm{d}}} \right) + \frac{x_{\mathrm{d}} - x_{\mathsf{c}}}{r_{\mathrm{d}}} \sqrt{1 - \frac{(x_{\mathrm{d}} - x_{\mathsf{c}})^2}{r_{\mathrm{d}}^2}} \right) \Bigg|_{x_{\mathrm{d}_1}}^{x_{\mathrm{d}_2}}.
\end{aligned} \tag{A.22}$$

In summary,

$$A_{\tilde{\mathcal{S}}_j} = \begin{cases} (y_{\mathsf{c}} - l_i)x_{\mathrm{d}} + \frac{r_{\mathrm{d}}^2}{2}\left(\sin^{-1}\left(\frac{x_{\mathrm{d}}-x_{\mathsf{c}}}{r_{\mathrm{d}}}\right) + \frac{x_{\mathrm{d}}-x_{\mathsf{c}}}{r_{\mathrm{d}}}\sqrt{1-\frac{(x_{\mathrm{d}}-x_{\mathsf{c}})^2}{r_{\mathrm{d}}^2}}\right)\Big|_{x_{\mathrm{d}_1}}^{x_{\mathrm{d}_2}} & j = 1,2 \\ -(y_{\mathsf{c}} + l_i)x_{\mathrm{d}} + \frac{r_{\mathrm{d}}^2}{2}\left(\sin^{-1}\left(\frac{x_{\mathrm{d}}-x_{\mathsf{c}}}{r_{\mathrm{d}}}\right) + \frac{x_{\mathrm{d}}-x_{\mathsf{c}}}{r_{\mathrm{d}}}\sqrt{1-\frac{(x_{\mathrm{d}}-x_{\mathsf{c}})^2}{r_{\mathrm{d}}^2}}\right)\Big|_{x_{\mathrm{d}_1}}^{x_{\mathrm{d}_2}} & j = 3,4. \end{cases} \tag{A.23}$$

The inner sector that is to be subtracted from $A_{\tilde{\mathcal{S}}_j}$ when solving for the electrode-disk overlap area is defined by the lateral electrode geometry, which is fixed with an arc center at the origin and area given by (A.5). The area of this sector is thus independent of electrode number so the lateral electrode-disk overlap areas are given by

$$A_{\mathcal{E}_{ij}} = A_{\tilde{\mathcal{S}}_j}(r_{\mathrm{d}}, l_i, x_{\mathsf{c}}, y_{\mathsf{c}}) - A_{\mathcal{S}}(r_{i,\mathrm{i}}, l_i). \tag{A.24}$$

Note that when the disk is centered at the origin, $A_{\tilde{\mathcal{S}}_j}(r_{\mathrm{d}}, l_i, 0, 0) = A_{\mathcal{S}}(r_{\mathrm{d}}, l_i)$.

The lateral electrode-disk overlap centroids are now calculated. The first moment of area of $\tilde{S}_j$ in the C_1-direction, $\tilde{Q}_{x_j}(r_{\mathrm{d}}, l_i, x_{\mathsf{c}}, y_{\mathsf{c}})$, is computed, beginning with quadrants 1 and 2 of the C-frame:

$$\begin{aligned} \tilde{Q}_{x_j} &= \int_{x_{\mathrm{d}_1}}^{x_{\mathrm{d}_2}} \int_{l_i}^{y_{\mathsf{c}}+\sqrt{r_{\mathrm{d}}^2-(x_{\mathrm{d}}-x_{\mathsf{c}})^2}} y_{\mathrm{d}}\, dy_{\mathrm{d}}\, dx_{\mathrm{d}} \\ &= \frac{1}{2}\int_{x_{\mathrm{d}_1}}^{x_{\mathrm{d}_2}} \left[y_{\mathsf{c}}^2 + 2y_{\mathsf{c}}\sqrt{r_{\mathrm{d}}^2-(x_{\mathrm{d}}-x_{\mathsf{c}})^2} + r_{\mathrm{d}}^2 - (x_{\mathrm{d}}-x_{\mathsf{c}})^2 - l_i^2\right] dx_{\mathrm{d}} \\ &= -\frac{x_{\mathrm{d}}^3}{6} + \frac{x_{\mathsf{c}}x_{\mathrm{d}}^2}{2} + \frac{(y_{\mathsf{c}}^2 + r_{\mathrm{d}}^2 - x_{\mathsf{c}}^2 - l_i^2)\, x_{\mathrm{d}}}{2}\Big|_{x_{\mathrm{d}_1}}^{x_{\mathrm{d}_2}} + y_{\mathsf{c}}\int_{x_{\mathrm{d}_1}}^{x_{\mathrm{d}_2}} \sqrt{r_{\mathrm{d}}^2-(x_{\mathrm{d}}-x_{\mathsf{c}})^2}\, dx_{\mathrm{d}}, \end{aligned} \tag{A.25}$$

where the four arguments of $\tilde{Q}_{x_j}$ have been dropped for brevity. The remaining integral on the right-hand side of (A.25) is solved using integration by substitution. Substituting $u = x_{\mathrm{d}} - x_{\mathsf{c}}$ so that $du = dx_{\mathrm{d}}$,

$$\int_{x_{\mathrm{d}_1}}^{x_{\mathrm{d}_2}} \sqrt{r_{\mathrm{d}}^2-(x_{\mathrm{d}}-x_{\mathsf{c}})^2}\, dx_{\mathrm{d}} = \int_{u_1}^{u_2} \sqrt{r_{\mathrm{d}}^2-u^2}\, du. \tag{A.26}$$

Now let $u = r_{\mathrm{d}} \sin(v)$ so that $du = r_{\mathrm{d}} \cos(v)\, dv$:

$$\begin{aligned}
\int_{u_1}^{u_2} \sqrt{r_{\mathrm{d}}^2 - u^2}\, du &= \int_{v_1}^{v_2} r_{\mathrm{d}} \cos(v) \sqrt{r_{\mathrm{d}}^2 - r_{\mathrm{d}}^2 \sin^2(v)}\, dv \\
&= \frac{r_{\mathrm{d}}^2}{2} \int_{v_1}^{v_2} \left(1 + \cos(2v)\right)\, dv \\
&= \frac{r_{\mathrm{d}}^2}{2} \left(v + \frac{1}{2} \sin(2v) \right) \Bigg|_{v_1}^{v_2} \\
&= \frac{r_{\mathrm{d}}^2}{2} \left(v + \sin(v) \cos(v) \right) \Bigg|_{v_1}^{v_2}. \qquad \text{(A.27)}
\end{aligned}$$

Substituting $v = \sin^{-1}\left(\frac{x_{\mathrm{d}} - x_{\mathsf{c}}}{r_{\mathrm{d}}}\right)$ into the equation and returning to (A.25), the first moment of area of $\tilde{\mathcal{S}}_j$, $j = 1, 2$, in the C_1-direction is

$$\begin{aligned}
\tilde{Q}_{x_j} = &- \frac{x_{\mathrm{d}}^3}{6} + \frac{x_{\mathsf{c}} x_{\mathrm{d}}^2}{2} + \frac{(y_{\mathsf{c}}^2 + r_{\mathrm{d}}^2 - x_{\mathsf{c}}^2 - l_i) x_{\mathrm{d}}}{2} \Bigg|_{x_{\mathrm{d}_1}}^{x_{\mathrm{d}_2}} \\
&+ \frac{y_{\mathsf{c}} r_{\mathrm{d}}^2}{2} \left(\sin^{-1}\left(\frac{x_{\mathrm{d}} - x_{\mathsf{c}}}{r_{\mathrm{d}}} \right) + \frac{x_{\mathrm{d}} - x_{\mathsf{c}}}{r_{\mathrm{d}}} \sqrt{1 - \frac{(x_{\mathrm{d}} - x_{\mathsf{c}})^2}{r_{\mathrm{d}}^2}} \right) \Bigg|_{x_{\mathrm{d}_1}}^{x_{\mathrm{d}_2}}. \qquad \text{(A.28)}
\end{aligned}$$

Continuing on to the first moment of area in the C_2-direction for $j = 1, 2$,

$$\begin{aligned}
\tilde{Q}_{y_j} &= \int_{x_{\mathrm{d}_1}}^{x_{\mathrm{d}_2}} \int_{l_i}^{y_{\mathsf{c}} + \sqrt{r_{\mathrm{d}}^2 - (x_{\mathrm{d}} - x_{\mathsf{c}})^2}} x_{\mathrm{d}}\, dy_{\mathrm{d}}\, dx_{\mathrm{d}} \\
&= \int_{x_{\mathrm{d}_1}}^{x_{\mathrm{d}_2}} \left[(y_{\mathsf{c}} - l_i)\, x_{\mathrm{d}} + x_{\mathrm{d}} \sqrt{r_{\mathrm{d}}^2 - (x_{\mathrm{d}} - x_{\mathsf{c}})^2} \right] dx_{\mathrm{d}} \\
&= \frac{(y_{\mathsf{c}} - l_i)\, x_{\mathrm{d}}^2}{2} \Bigg|_{x_{\mathrm{d}_1}}^{x_{\mathrm{d}_2}} + \int_{x_{\mathrm{d}_1}}^{x_{\mathrm{d}_2}} x_{\mathrm{d}} \sqrt{r_{\mathrm{d}}^2 - (x_{\mathrm{d}} - x_{\mathsf{c}})^2}\, dx_{\mathrm{d}}. \qquad \text{(A.29)}
\end{aligned}$$

To solve the remaining integral, let $u = x_{\mathrm{d}} - x_{\mathsf{c}}$ so that $du = dx_{\mathrm{d}}$.

$$\begin{aligned}
\int_{x_{\mathrm{d}_1}}^{x_{\mathrm{d}_2}} x_{\mathrm{d}} \sqrt{r_{\mathrm{d}}^2 - (x_{\mathrm{d}} - x_{\mathsf{c}})^2}\, dx_{\mathrm{d}} &= \int_{u_1}^{u_2} (u + x_{\mathsf{c}}) \sqrt{r_{\mathrm{d}}^2 - u^2}\, du \\
&= \int_{u_1}^{u_2} u \sqrt{r_{\mathrm{d}}^2 - u^2}\, du + x_{\mathsf{c}} \int_{u_1}^{u_2} \sqrt{r_{\mathrm{d}}^2 - u^2}\, du \qquad \text{(A.30)}
\end{aligned}$$

Focusing on the first integral on the right-hand-side of (A.30), let $v = r_{\mathrm{d}}^2 - u^2$ so that

$dv = -2u\,du$.

$$\begin{aligned}\int_{u_1}^{u_2} u\sqrt{r_{\mathrm{d}}^2 - u^2}\,du &= \int_{v_1}^{v_2} -\frac{1}{2}v^{1/2}\,dv \\ &= -\frac{1}{3}v^{3/2}\Big|_{v_1}^{v_2} \\ &= -\frac{1}{3}\left(r_{\mathrm{d}}^2 - u^2\right)^{3/2}\Big|_{u_1}^{u_2}\end{aligned} \tag{A.31}$$

Turning to the second integral on the right-hand-side of (A.30), let $u = r_{\mathrm{d}}\sin(v)$ so that $du = r_{\mathrm{d}}\cos(v)\,dv$.

$$\begin{aligned}\int_{u_1}^{u_2} \sqrt{r_{\mathrm{d}}^2 - u^2}\,du &= \int_{v_1}^{v_2} r_{\mathrm{d}}\cos(v)\sqrt{r_{\mathrm{d}}^2 - \mathrm{d}^2\sin^2(v)}\,dv \\ &= \frac{r_{\mathrm{d}}^2}{2}\int_{v_1}^{v_2}\left(1 + \cos(2v)\right)\,dv \\ &= \frac{r_{\mathrm{d}}^2}{2}\left(v + \frac{\sin(2v)}{2}\right)\Big|_{v_1}^{v_2} \\ &= \frac{r_{\mathrm{d}}^2}{2}\left(v + \sin(v)\cos(v)\right)\Big|_{v_1}^{v_2} \\ &= \frac{r_{\mathrm{d}}^2}{2}\left(\sin^{-1}\left(\frac{u}{r_{\mathrm{d}}}\right) + \frac{u}{\mathrm{d}}\sqrt{1 - \frac{u^2}{r_{\mathrm{d}}^2}}\right)\Big|_{u_1}^{u_2}\end{aligned} \tag{A.32}$$

Multiplying the solutions in (A.31) and (A.32) by the appropriate coefficients from (A.30) and summing the result,

$$\begin{aligned}\int_{x_{\mathrm{d}_1}}^{x_{\mathrm{d}_2}} x_{\mathrm{d}}\sqrt{r_{\mathrm{d}}^2 - (x_{\mathrm{d}} - x_{\mathsf{c}})^2}\,dx_{\mathrm{d}} = &-\frac{\left(r_{\mathrm{d}}^2 - u^2\right)^{3/2}}{3}\Big|_{u_1}^{u_2} \\ &+ \frac{x_{\mathsf{c}}r_{\mathrm{d}}^2}{2}\left(\sin^{-1}\left(\frac{u}{r_{\mathrm{d}}}\right) + \frac{u}{r_{\mathrm{d}}}\sqrt{1 - \frac{u^2}{r_{\mathrm{d}}^2}}\right)\Big|_{u_1}^{u_2}.\end{aligned} \tag{A.33}$$

Substituting $u = x_{\mathrm{d}} - x_{\mathsf{c}}$ into the solution and returning to (A.29), the first moment of area of $\tilde{\mathcal{S}}_j$, $j = 1, 2$, in the C_2-direction is given as

$$\begin{aligned}\tilde{Q}_{y_j} = &\frac{\left(y_{\mathsf{c}} - l_i\right)x_{\mathrm{d}}^2}{2} - \frac{\left(r_{\mathrm{d}}^2 - (x_{\mathrm{d}} - x_{\mathsf{c}})^2\right)^{3/2}}{3}\Big|_{x_{\mathrm{d}_1}}^{x_{\mathrm{d}_2}} \\ &+ \frac{x_{\mathsf{c}}r_{\mathrm{d}}^2}{2}\left(\sin^{-1}\left(\frac{x_{\mathrm{d}} - x_{\mathsf{c}}}{r_{\mathrm{d}}}\right) + \frac{x_{\mathrm{d}} - x_{\mathsf{c}}}{r_{\mathrm{d}}}\sqrt{1 - \frac{(x_{\mathrm{d}} - x_{\mathsf{c}})^2}{r_{\mathrm{d}}^2}}\right)\Big|_{x_{\mathrm{d}_1}}^{x_{\mathrm{d}_2}}.\end{aligned} \tag{A.34}$$

For the third and fourth quadrants of the C-frame, the first moment of area of $\tilde{\mathcal{S}}_j$ in the C_1-direction is given by

$$\begin{aligned}
\tilde{Q}_{x_j} &= \int_{x_{\mathrm{d}_1}}^{x_{\mathrm{d}_2}} \int_{y_\mathsf{c}-\sqrt{r_\mathrm{d}^2-(x_\mathrm{d}-x_\mathsf{c})^2}}^{-l_i} y_\mathrm{d}\, dy_\mathrm{d}\, dx_\mathrm{d} \\
&= -\frac{1}{2}\int_{x_{\mathrm{d}_1}}^{x_{\mathrm{d}_2}} \left[-l_i^2 + y_\mathsf{c}^2 - 2y_\mathsf{c}\sqrt{r_\mathrm{d}^2-(x_\mathrm{d}-x_\mathsf{c})^2} + r_\mathrm{d}^2 - (x_\mathrm{d}-x_\mathsf{c})^2\right] dx_\mathrm{d} \\
&= \frac{x_\mathrm{d}^3}{6} - \frac{x_\mathsf{c}x_\mathrm{d}^2}{2} - \frac{\left(y_\mathsf{c}^2 + r_\mathrm{d}^2 - x_\mathsf{c}^2 - l_i^2\right) x_\mathrm{d}}{2}\bigg|_{x_{\mathrm{d}_1}}^{x_{\mathrm{d}_2}} + y_\mathsf{c}\int_{x_{\mathrm{d}_1}}^{x_{\mathrm{d}_2}} \sqrt{r_\mathrm{d}^2-(x_\mathrm{d}-x_\mathsf{c})^2}\, dx_\mathrm{d}.
\end{aligned} \tag{A.35}$$

The remaining integral was solved above, so for $j = 3, 4$:

$$\begin{aligned}
\tilde{Q}_{x_j} = \frac{x_\mathrm{d}^3}{6} - \frac{x_\mathsf{c}x_\mathrm{d}^2}{2} - \frac{(y_\mathsf{c}^2 + r_\mathrm{d}^2 - x_\mathsf{c}^2 - l_i^2)x_\mathrm{d}}{2}\bigg|_{x_{\mathrm{d}_1}}^{x_{\mathrm{d}_2}} \\
+ \frac{y_\mathsf{c}r_\mathrm{d}^2}{2}\left(\sin^{-1}\left(\frac{x_\mathrm{d}-x_\mathsf{c}}{r_\mathrm{d}}\right) + \frac{x_\mathrm{d}-x_\mathsf{c}}{r_\mathrm{d}}\sqrt{1-\frac{(x_\mathrm{d}-x_\mathsf{c})^2}{r_\mathrm{d}^2}}\right)\bigg|_{x_{\mathrm{d}_1}}^{x_{\mathrm{d}_2}}.
\end{aligned} \tag{A.36}$$

The first moment of area of $\tilde{\mathcal{S}}_j$, $j = 3, 4$, in the C_2-direction is

$$\begin{aligned}
\tilde{Q}_{y_j} &= \int_{x_{\mathrm{d}_1}}^{x_{\mathrm{d}_2}} \int_{y_\mathsf{c}-\sqrt{r_\mathrm{d}^2-(x_\mathrm{d}-x_\mathsf{c})^2}}^{-l_i} x_\mathrm{d}\, dy_\mathrm{d}\, dx_\mathrm{d} \\
&= \int_{x_{\mathrm{d}_1}}^{x_{\mathrm{d}_2}} \left[-(y_\mathsf{c}+l_i)x_\mathrm{d} + x_\mathrm{d}\sqrt{r_\mathrm{d}^2-(x_\mathrm{d}-x_\mathsf{c})^2}\right] dx_\mathrm{d} \\
&= -\frac{(y_\mathsf{c}+l_i)\, x_\mathrm{d}^2}{2}\bigg|_{x_{\mathrm{d}_1}}^{x_{\mathrm{d}_2}} + \int_{x_{\mathrm{d}_1}}^{x_{\mathrm{d}_2}} x_\mathrm{d}\sqrt{r_\mathrm{d}^2-(x_\mathrm{d}-x_\mathsf{c})^2}\, dx_\mathrm{d}
\end{aligned} \tag{A.37}$$

Only the coefficient in the first term changes between the $j = 1, 2$ case and the $j = 3, 4$ case, so

$$\begin{aligned}
Q_{y_j} = -\frac{(y_\mathsf{c}+l_i)\, x_\mathrm{d}^2}{2} - \frac{\left(r_\mathrm{d}^2-(x_\mathrm{d}-x_\mathsf{c})^2\right)^{3/2}}{3}\bigg|_{x_{\mathrm{d}_1}}^{x_{\mathrm{d}_2}} \\
+ \frac{x_\mathsf{c}r_\mathrm{d}^2}{2}\left(\sin^{-1}\left(\frac{x_\mathrm{d}-x_\mathsf{c}}{r_\mathrm{d}}\right) + \frac{x_\mathrm{d}-x_\mathsf{c}}{r_\mathrm{d}}\sqrt{1-\frac{(x_\mathrm{d}-x_\mathsf{c})^2}{r_\mathrm{d}^2}}\right)\bigg|_{x_{\mathrm{d}_1}}^{x_{\mathrm{d}_2}}.
\end{aligned} \tag{A.38}$$

In summary,

$$\tilde{Q}_{x_j}(r_{\mathrm{d}}, l_i, x_{\mathsf{c}}, y_{\mathsf{c}}) = \begin{cases} -\frac{x_{\mathrm{d}}^3}{6} + \frac{x_{\mathsf{c}} x_{\mathrm{d}}^2}{2} + \frac{(y_{\mathsf{c}}^2 + r_{\mathrm{d}}^2 - x_{\mathsf{c}}^2 - l_i^2) x_{\mathrm{d}}}{2} + \frac{y_{\mathsf{c}} r_{\mathrm{d}}^2}{2}\, a(x_{\mathrm{d}})\Big|_{x_{\mathrm{d}_1}}^{x_{\mathrm{d}_2}} & j = 1, 2 \\ \frac{x_{\mathrm{d}}^3}{6} - \frac{x_{\mathsf{c}} x_{\mathrm{d}}^2}{2} - \frac{(y_{\mathsf{c}}^2 + r_{\mathrm{d}}^2 - x_{\mathsf{c}}^2 - l_i^2) x_{\mathrm{d}}}{2} + \frac{y_{\mathsf{c}} r_{\mathrm{d}}^2}{2}\, a(x_{\mathrm{d}})\Big|_{x_{\mathrm{d}_1}}^{x_{\mathrm{d}_2}} & j = 3, 4 \end{cases} \tag{A.39}$$

$$\tilde{Q}_{y_j}(r_{\mathrm{d}}, l_i, x_{\mathsf{c}}, y_{\mathsf{c}}) = \begin{cases} \frac{(y_{\mathsf{c}} - l_i) x_{\mathrm{d}}^2}{2} - \frac{\left(r_{\mathrm{d}}^2 - (x_{\mathrm{d}} - x_{\mathsf{c}})^2\right)^{3/2}}{3} + \frac{x_{\mathsf{c}} r_{\mathrm{d}}^2}{2}\, a(x_{\mathrm{d}})\Big|_{x_{\mathrm{d}_1}}^{x_{\mathrm{d}_2}} & j = 1, 2 \\ -\frac{(y_{\mathsf{c}} + l_i) x_{\mathrm{d}}^2}{2} - \frac{\left(r_{\mathrm{d}}^2 - (x_{\mathrm{d}} - x_{\mathsf{c}})^2\right)^{3/2}}{3} + \frac{x_{\mathsf{c}} r_{\mathrm{d}}^2}{2}\, a(x_{\mathrm{d}})\Big|_{x_{\mathrm{d}_1}}^{x_{\mathrm{d}_2}} & j = 3, 4, \end{cases} \tag{A.40}$$

where

$$a(x_{\mathrm{d}}) = \sin^{-1}\left(\frac{x_{\mathrm{d}} - x_{\mathsf{c}}}{r_{\mathrm{d}}}\right) + \frac{x_{\mathrm{d}} - x_{\mathsf{c}}}{r_{\mathrm{d}}}\sqrt{1 - \frac{(x_{\mathrm{d}} - x_{\mathsf{c}})^2}{r_{\mathrm{d}}^2}}. \tag{A.41}$$

The centroids of the electrode-disk overlap areas in the C-frame are computed according to

$$\bar{x}_{ij,\mathsf{c}} = \begin{cases} \frac{\tilde{Q}_{y_1}(r_{\mathrm{d}}, l_i, x_{\mathsf{c}}, y_{\mathsf{c}}) - Q_y(r_{i,\mathrm{i}}, l_i)}{A_{\mathcal{E}_{i1}}} & j = 1 \\ \frac{\tilde{Q}_{y_2}(r_{\mathrm{d}}, l_i, x_{\mathsf{c}}, y_{\mathsf{c}}) + Q_y(r_{i,\mathrm{i}}, l_i)}{A_{\mathcal{E}_{i2}}} & j = 2 \\ \frac{\tilde{Q}_{y_3}(r_{\mathrm{d}}, l_i, x_{\mathsf{c}}, y_{\mathsf{c}}) + Q_y(r_{i,\mathrm{i}}, l_i)}{A_{\mathcal{E}_{i3}}} & j = 3 \\ \frac{\tilde{Q}_{y_4}(r_{\mathrm{d}}, l_i, x_{\mathsf{c}}, y_{\mathsf{c}}) - Q_y(r_{i,\mathrm{i}}, l_i)}{A_{\mathcal{E}_{i4}}} & j = 4 \end{cases} \tag{A.42}$$

$$\bar{y}_{ij,\mathsf{c}} = \begin{cases} \frac{\tilde{Q}_{x_1}(r_{\mathrm{d}}, l_i, x_{\mathsf{c}}, y_{\mathsf{c}}) - Q_x(r_{i,\mathrm{i}}, l_i)}{A_{\mathcal{E}_{i1}}} & j = 1 \\ \frac{\tilde{Q}_{x_2}(r_{\mathrm{d}}, l_i, x_{\mathsf{c}}, y_{\mathsf{c}}) - Q_x(r_{i,\mathrm{i}}, l_i)}{A_{\mathcal{E}_{i1}}} & j = 2 \\ \frac{\tilde{Q}_{x_3}(r_{\mathrm{d}}, l_i, x_{\mathsf{c}}, y_{\mathsf{c}}) + Q_x(r_{i,\mathrm{i}}, l_i)}{A_{\mathcal{E}_{i1}}} & j = 3 \\ \frac{\tilde{Q}_{x_4}(r_{\mathrm{d}}, l_i, x_{\mathsf{c}}, y_{\mathsf{c}}) + Q_x(r_{i,\mathrm{i}}, l_i)}{A_{\mathcal{E}_{i1}}} & j = 4. \end{cases} \tag{A.43}$$

Conversion to the N-frame is accomplished using the $\mathcal{R}_{\mathsf{NC}}$ transformation matrix,

$$\begin{bmatrix} \bar{x}_{ij} \\ \bar{y}_{ij} \end{bmatrix} = \mathcal{R}_{\mathsf{NC}} \begin{bmatrix} \bar{x}_{ij,\mathsf{c}} \\ \bar{x}_{ij,\mathsf{c}} \end{bmatrix}. \tag{A.44}$$

When the nominal position of the disk is selected such that the disk's center of mass lies at the origin of the N-frame, these centroids can be written in the form

$$(\bar{x}_{ij}, \bar{y}_{ij}) = \begin{cases} (\bar{r}_i, 0) & j = 1 \\ (0, \bar{r}_i) & j = 2 \\ (-\bar{r}_i, 0) & j = 3 \\ (0, -\bar{r}_i) & j = 4. \end{cases} \tag{A.45}$$

Table A.2: Geometric Parameters for Electrode Configuration I

Symbol	Description	Value
$r_{1,\mathrm{i}}$	inner radius of primary electrodes	1.5 mm
$r_{1,\mathrm{o}}$	outer radius of primary electrodes	37 mm
$r_{2,\mathrm{i}}$	inner radius of lateral electrodes	38 mm
$r_{2,\mathrm{o}}$	outer radius of lateral electrodes	44 mm
l_1	half gap between primary electrodes	0.5 mm
l_2	half gap between lateral electrodes	3.5 mm
$A_{\mathcal{E}_{1j}}$	primary electrode area	10.3 cm^2
$A_{\mathcal{E}_{2j}}$	lateral electrode-disk overlap area	1.65 cm^2
$\bar{r}_1$	radial distance to primary electrode centroids	22.5 mm
$\bar{r}_2$	radial distance to lateral electrode-disk overlap centroids	36.4 mm

Table A.3: Geometric Parameters for Electrode Configuration II

Symbol	Description	Value
$r_{1,\mathrm{i}}$	inner radius of control electrodes	1.5 mm
$r_{1,\mathrm{o}}$	outer radius of control electrodes	26 mm
$r_{2,\mathrm{i}}$	inner radius of primary sense electrodes	27 mm
$r_{2,\mathrm{o}}$	outer radius of primary sense electrodes	37 mm
$r_{3,\mathrm{i}}$	inner radius of lateral electrodes	38 mm
$r_{3,\mathrm{o}}$	outer radius of lateral electrodes	44 mm
l_1	half gap between control electrodes	0.5 mm
l_2	half gap between primary sense electrodes	1.0 mm
l_3	half gap between lateral electrodes	3.5 mm
$A_{\mathcal{E}_{1j}}$	control electrode area	5.05 cm^2
$A_{\mathcal{E}_{2j}}$	primary sense electrode area	4.83 cm^2
$A_{\mathcal{E}_{3j}}$	lateral electrode-disk overlap area	1.65 cm^2
$\bar{r}_1$	radial distance to control electrode centroids	15.9 mm
$\bar{r}_2$	radial distance to primary sense electrode centroids	29.3 mm
$\bar{r}_3$	radial distance to lateral electrode-disk overlap centroids	36.4 mm

Computed values of the lateral electrode areas and centroids for the initial and updated electrode configurations are provided in Tables A.2 and A.3, respectively.

APPENDIX B

Fringing Field Capacitance

The parallel-plate capacitance estimates in (2.43) neglect the effect of electrical field fringing near the edges of the disk and electrodes, thus underestimating the true electrode-disk capacitances. The effect of the fringing capacitance is difficult to quantify due to the irregular shape of the electrodes. An expression for estimating the fringing capacitance for circular plates was proposed in [SBS86], however, due to the relatively large perimeter-to-surface-area ratio of the electrodes, especially as annular index increases, a rectangular plate model is assumed for analyzing the fringe field effects. The total capacitance, including fringing, of parallel rectangular plates given by

$$C = \frac{\epsilon w l}{d}\left(1+\frac{d}{\pi w}\left(1+\ln\left(\frac{2\pi w}{d}\right)\right)\right)\left(1+\frac{d}{\pi l}\left(1+\ln\left(\frac{2\pi l}{d}\right)\right)\right), \tag{B.1}$$

where w and l are the plate width and length, respectively, and d is the plate separation, has been shown to match simulations using finite element methods with high fidelity for a wide range of plate gaps [Pal37, HZP07]. Applying the expression in (B.1) to the electrode-disk subsystem, the fringing capacitances between the disk and the top electrodes can be written as

$$\begin{aligned} C_{\mathrm{f,t}_{ij}} \approx & \frac{\epsilon w_{ij} l_{ij}}{z_0 - z_{ij}}\left(1+\frac{z_0 - z_{ij}}{\pi w_{ij}}\left(1+\ln\left(\frac{2\pi w_{ij}}{z_0 - z_{ij}}\right)\right)\right) \\ & \times\left(1+\frac{z_0 - z_{ij}}{\pi l_{ij}}\left(1+\ln\left(\frac{2\pi l_{ij}}{z_0 - z_{ij}}\right)\right)\right) - C_{\mathrm{t}_{ij}}. \end{aligned} \tag{B.2}$$

Similarly, the fringing capacitances between the bottom electrodes and the disk are

$$\begin{aligned} C_{\mathrm{f,b}_{ij}} \approx & \frac{\epsilon w_{ij} l_{ij}}{z_0 + z_{ij}}\left(1+\frac{z_0 + z_{ij}}{\pi w_{ij}}\left(1+\ln\left(\frac{2\pi w_{ij}}{z_0 + z_{ij}}\right)\right)\right) \\ & \times\left(1+\frac{z_0 + z_{ij}}{\pi l_{ij}}\left(1+\ln\left(\frac{2\pi l_{ij}}{z_0 + z_{ij}}\right)\right)\right) - C_{\mathrm{b}_{ij}}. \end{aligned} \tag{B.3}$$

Table B.1: Nominal Fringing Capacitances

Electrode Configuration I			Electrode Configuration II		
Electrode	Capacitance, Fringing Ignored	Fringing Capacitance	Electrode	Capacitance, Fringing Ignored	Fringing Capacitance
$\mathcal{E}_{1j}$	77.1 pF	1.54 pF	$\mathcal{E}_{1j}$	37.6 pF	1.03 pF
$\mathcal{E}_{2j}$	12.3 pF	1.02 pF	$\mathcal{E}_{2j}$	36.0 pF	1.25 pF
			$\mathcal{E}_{3j}$	12.3 pF	1.02 pF

Since the electrode-disk capacitors are not rectangular, however, geometric approximations are used for the lengths and widths. For the innermost electrode set, i.e., $i = 1$, the electrodes are approximated as squares. For the lateral electrodes, the widths will be taken as the difference between the disk radius and the inner radius of the lateral electrodes, with a correction factor that takes into account the lateral position of the disk. In the case of the second electrode configuration, the width of the middle annulus of electrodes is taken as the difference between the outer electrode radius and the inner electrode radius. These widths are summarized as

$$w_{ij} = \begin{cases} \sqrt{A_{\mathcal{E}_{ij}}} & i = 1 \\ r_{\mathrm{d}} - r_{2,\mathrm{i}} + c_j & i = 2 \end{cases} \tag{B.4}$$

for the initial electrode configuration and

$$w_{ij} = \begin{cases} \sqrt{A_{\mathcal{E}_{ij}}} & i = 1 \\ r_{2,\mathrm{o}} - r_{2,\mathrm{i}} & i = 2 \\ r_{\mathrm{d}} - r_{3,\mathrm{i}} + c_j & i = 3 \end{cases} \tag{B.5}$$

for the segregated electrode configuration where the correction factor, c_j, is

$$c_j = \begin{cases} (-1)^{\frac{j-1}{2}} x & j = 1, 3 \\ (-1)^{\frac{j}{2}-1} y & j = 2, 4. \end{cases} \tag{B.6}$$

The corresponding lengths are then given by

$$l_{ij} = \frac{A_{\mathcal{E}_{ij}}}{w_{ij}}. \tag{B.7}$$

The results with the disk suspended at its nominal position are summarized in Table B.1 and compared to the capacitances computed in (2.43). Note that the top and bottom

Table B.2: Fringing Neglection Error

Electrode Configuration I		Electrode Configuration II	
Electrode	Capacitance Underestimate	Electrode	Capacitance Underestimate
$\mathcal{E}_{1j}$	2.00%	$\mathcal{E}_{1j}$	2.74%
$\mathcal{E}_{2j}$	8.32%	$\mathcal{E}_{2j}$	3.46%
		$\mathcal{E}_{3j}$	8.32%

electrode-disk (fringing) capacitances are identical (hence the "t" and "b" subscripts on the electrodes have been omitted in the table) and the specific electrode, j, for a given annular ring is inconsequential with the disk in this position. The percent error of each electrode-disk capacitance due to neglected fringing effects are computed relative to the approximated values from (2.43) and are provided in Table B.2. The relative error increases with the ratio between perimeter and area, however, even for the lateral electrodes where this ratio is largest, fringe field effects do not appreciably change the total electrode-disk capacitances and can be ignored.

APPENDIX C

Viscous Damping

The fluid (air) permeating the micro-scale gaps between the disk and electrodes provides noticeable damping to disk motion in the translational, roll, and pitch degrees of freedom. Advanced modeling techniques for such damping terms are beyond the scope of this dissertation, however, simple mathematical approximations have been previously developed that are applied to the disk system. The squeeze film damping of a fluid is governed by viscous and inertial effects, however, for the small gaps associated with MEMS devices, inertial effects are negligible and the squeeze film behavior is approximated by the Reynolds equation. In [BY07], the Reynolds equation is applied to parallel plates moving vertically relative to one another, i.e., the gap between the plates expands or retracts, and a linearization is performed about the nominal plate gap. Isothermal conditions and slow squeeze action, i.e., the gas is considered incompressible, are assumed and the Reynolds equation for squeeze film damping is given in polar coordinates by

$$\frac{1}{r}\frac{\partial}{\partial r}\left(r\frac{\partial}{\partial r}p(r)\right) = \frac{12\mu}{h^3}\dot{h}, \tag{C.1}$$

where p is the damping pressure, μ is the dynamic viscosity of the fluid, h is the height of the nominal plate gap, and $\dot{h}$ is the velocity of the movable plate. The damping force can be computed by integrating the damping pressure over the plate area, and the vertical damping coefficient, c_{v}, is given by

$$c_{\mathrm{v}} = \frac{3\pi\mu r^4}{2h^3}, \tag{C.2}$$

where r is the plate radius. With the disk suspended, two air gaps are established that both provide damping and must be accounted for. The vertical damping coefficients for the top

and bottom air gaps, c_{z_t} and c_{z_t}, respectively, are given by

$$\begin{aligned} c_{z_t} &= \frac{3\pi\mu r_d^4}{2\left(\frac{z_{sh}}{2} - z\right)^3} \\ c_{z_b} &= \frac{3\pi\mu r_d^4}{2\left(\frac{z_{sh}}{2} + z\right)^3} \end{aligned} \tag{C.3}$$

and the net vertical damping coefficient is the sum of the top and bottom vertical damping coefficients,

$$c_z = c_{z_t} + c_{z_b}. \tag{C.4}$$

The torsional damping coefficients are estimated from approximated damping moments of rectangular torsion mirrors. A linearization of the Reynolds equation was performed in [PKP98] by assuming small angular displacements and a harmonic response of the mirror. The damping moment associated with angular rotation α is approximated as

$$M_\alpha = -\frac{48}{\pi^6\left(\left(\frac{w}{l}\right)^2 + 4\right)}\frac{\mu l w^5}{h^3}\dot{\alpha}, \tag{C.5}$$

where w and l are the plate width and length, respectively. This solution is extended to circular plates using area as follows. The disk can be thought of as an ellipse, with major and minor axes that are equivalent in length. Applying (C.5) to a plate where the length and width are identical,

$$M_\alpha = -\frac{48\mu l^6}{5\pi^6 h^3}\dot{\alpha}. \tag{C.6}$$

Since the area of such a plate (a square) is given by l^2, the area cubed appears in the numerator. Thus, l^6 is approximated by the area of the disk raised to the power of three,

$$M_\alpha \approx -\frac{48\mu r_d^6}{5\pi^3 h^3}\dot{\alpha}. \tag{C.7}$$

Applying this approximation to the disk-electrode subsystem and taking into account the squeeze films above and below the disk, the top and bottom torsional damping coefficients are given as

$$\begin{aligned} c_{\theta_t} &= \frac{48\mu r_d^6}{5\pi^3\left(\frac{z_{sh}}{2} - z\right)^3} \\ c_{\theta_b} &= \frac{48\mu r_d^6}{5\pi^3\left(\frac{z_{sh}}{2} + z\right)^3}. \end{aligned} \tag{C.8}$$

The net torsional damping coefficient is the sum of the top and bottom torsional damping coefficients:

$$c_\theta = c_{\theta_\mathrm{t}} + c_{\theta_\mathrm{b}}. \tag{C.9}$$

Due to the symmetry of the system, the torsional damping coefficients about both the N_1- and N_2-axes are identical, i.e.,

$$c_\varphi = c_\theta. \tag{C.10}$$

Because of the small-scale air gap between the disk and each plate relative to the disk diameter, viscous damping in the lateral directions is approximated by Couette flow, which describes planar shear-driven fluid motion between two infinite plates, one of which moves at constant velocity while the other remains stationary [Wil07]. Ignoring pressure gradients (out-of-plane motion of the disk is neglected) and modeling fluid flow as fully developed, the Navier-Stokes equations applied to the Couette flow problem simplify to

$$\frac{d^2v}{d\eta^2} = 0, \tag{C.11}$$

where η is the vertical spatial coordinate normal to the plates and $v(\eta)$ represents the velocity field of the fluid. Assuming for now that the bottom plate is stationary and represents the bottom glass plate and the top plate represents the moving disk, the boundary conditions are given by $v(0) = 0$ and $v(h) = V$, where h is the gap between the plates and V is the velocity of the disk. Integrating (C.11) twice and applying the boundary conditions yields the velocity field

$$v(\eta) = \frac{V}{h}\eta. \tag{C.12}$$

According to Newton's law of viscosity, the shear force acting on the moving plate is given by

$$F_\mathrm{shear} = \mu A \frac{dv}{d\eta} = \frac{\mu A}{h} V, \tag{C.13}$$

where A is the plate area. The damping coefficient is the term preceeding the plate velocity,

$$c_\mathrm{shear} = \frac{\mu A}{h}. \tag{C.14}$$

For the disk system, shear forces resist in-plane motion due to the fluid both above and below the disk, so the top and bottom damping coefficients for disk motion in the N_1-direction are given by

$$\begin{aligned} c_{x_{\mathrm{t}}} &= \frac{\mu \pi r_{\mathrm{d}}^2}{\frac{z_{\mathrm{sh}}}{2} - z} \\ c_{x_{\mathrm{b}}} &= \frac{\mu \pi r_{\mathrm{d}}^2}{\frac{z_{\mathrm{sh}}}{2} + z}, \end{aligned} \tag{C.15}$$

respectively. The net damping in this direction is the sum of the two damping terms and a single damping coefficient,

$$c_x = c_{x_{\mathrm{t}}} + c_{x_{\mathrm{b}}}, \tag{C.16}$$

is quantified. Performing the computations in the N_2-direction yield an identical viscous damping coefficient:

$$c_y = c_x. \tag{C.17}$$

APPENDIX D

Gradients of the Generalized Forces and Torques

The gradients used in developing the time-invariant discrete-time model from linear variational equations are computed in this appendix. The calculations are presented in the order they are implemented in the script that generates the model and any long-form final results are omitted since the gradients of the generalized forces and torques with respect to q, $\dot{q}$, and w_{tf} can be written in terms of the computations from prior steps. Partial derivatives are simply presented and intermediate computations are left to the reader.

Beginning with the system geometry, the electrode-disk overlap areas and centroids for the inner (non-lateral) electrodes are independent of the disk position and velocity, thus these gradients are all equal to zero. The lateral electrode-disk overlap areas and centroids, however, are dependent on the lateral position of the disk. The expressions for these values are fairly complex and computing the gradient with respect to q is tedious, nevertheless, the midpoint method is used to numerically approximate the partial derivatives of the overlap areas and centroids with respect to x and y according to

$$\begin{aligned}\frac{\partial A_{\mathcal{E}_{ij}}(x,y)}{\partial x} &\approx \lim_{\delta_x \to 0^+} \frac{A_{\mathcal{E}_{ij}}(x+\delta_x,y) - A_{\mathcal{E}_{ij}}(x-\delta_x,y)}{2\delta_x} \\ \frac{\partial A_{\mathcal{E}_{ij}}(x,y)}{\partial y} &\approx \lim_{\delta_y \to 0^+} \frac{A_{\mathcal{E}_{ij}}(x,y+\delta_y) - A_{\mathcal{E}_{ij}}(x,y-\delta_y)}{2\delta_y}\end{aligned} \tag{D.1}$$

$$\begin{aligned}\frac{\partial \bar{x}_{ij}}{\partial x} &\approx \lim_{\delta_x \to 0^+} \frac{\bar{x}_{ij}(x+\delta_x,y) - \bar{x}_{ij}(x-\delta_x,y)}{2\delta_x} \\ \frac{\partial \bar{x}_{ij}}{\partial y} &\approx \lim_{\delta_y \to 0^+} \frac{\bar{x}_{ij}(x,y+\delta_y) - \bar{x}_{ij}(x,y-\delta_y)}{2\delta_y}\end{aligned} \tag{D.2}$$

$$\begin{aligned}\frac{\partial \bar{y}_{ij}}{\partial x} &\approx \lim_{\delta_x \to 0^+} \frac{\bar{y}_{ij}(x+\delta_x, y) - \bar{y}_{ij}(x-\delta_x, y)}{2\delta_x} \\ \frac{\partial \bar{y}_{ij}}{\partial y} &\approx \lim_{\delta_y \to 0^+} \frac{\bar{y}_{ij}(x, y+\delta_y) - \bar{y}_{ij}(x, y-\delta_y)}{2\delta_y},\end{aligned} \tag{D.3}$$

where $\delta_x = \delta_y = 1\,\text{nm}$ is implemented. Since the areas and centroids are assumed to be independent of angular rotations and vertical translations,

$$\begin{aligned}\frac{\partial A_{\mathcal{E}_{ij}}}{\partial z} &= \frac{\partial A_{\mathcal{E}_{ij}}}{\partial \theta} = \frac{\partial A_{\mathcal{E}_{ij}}}{\partial \varphi} = 0 \\ \frac{\partial \bar{x}_{ij}}{\partial z} &= \frac{\partial \bar{x}_{ij}}{\partial \theta} = \frac{\partial \bar{x}_{ij}}{\partial \varphi} = 0 \\ \frac{\partial \bar{y}_{ij}}{\partial z} &= \frac{\partial \bar{y}_{ij}}{\partial \theta} = \frac{\partial \bar{y}_{ij}}{\partial \varphi} = 0.\end{aligned} \tag{D.4}$$

The vertical deflections of the disk that define the capacitive gaps, z_{ij}, are dependent only on q and the corresponding partial derivatives are given by

$$\begin{aligned}\frac{\partial z_{ij}}{\partial x} &= \varphi\left(1 - \frac{\partial \bar{x}_{ij}}{\partial x}\right) + \theta \frac{\partial \bar{y}_{ij}}{\partial x} \\ \frac{\partial z_{ij}}{\partial y} &= -\varphi \frac{\partial \bar{x}_{ij}}{\partial y} + \theta\left(\frac{\partial \bar{y}_{ij}}{\partial y} - 1\right) \\ \frac{\partial z_{ij}}{\partial z} &= 1 \\ \frac{\partial z_{ij}}{\partial \theta} &= \bar{y}_{ij} - y \\ \frac{\partial z_{ij}}{\partial \varphi} &= x - \bar{x}_{ij}.\end{aligned} \tag{D.5}$$

The capacitances are a function of the electrode areas and capacitive gaps, so the partial derivatives of the capacitances with respect to q can be expressed succinctly as a function of the partial derivatives computed above,

$$\begin{aligned}\frac{\partial C_{\mathrm{t}_{ij}}}{\partial q_k} &= \frac{\varepsilon}{z_0 - z_{ij}} \frac{\partial A_{\mathcal{E}_{ij}}}{\partial q_k} + \frac{\varepsilon A_{\mathcal{E}_{ij}}}{(z_0 - z_{ij})^2} \frac{\partial z_{ij}}{\partial q_k} \\ \frac{\partial C_{\mathrm{b}_{ij}}}{\partial q_k} &= \frac{\varepsilon}{z_0 + z_{ij}} \frac{\partial A_{\mathcal{E}_{ij}}}{\partial q_k} - \frac{\varepsilon A_{\mathcal{E}_{ij}}}{(z_0 + z_{ij})^2} \frac{\partial z_{ij}}{\partial q_k}.\end{aligned} \tag{D.6}$$

Note that the notation q_k, $k = 1, 2, 3, 4, 5$, where $q = [q_1\ q_2\ q_3\ q_4\ q_5]^T = [x\ y\ z\ \theta\ \varphi]^T$, is used to formulate general expressions rather than write out the partial derivatives with respect to x, y, etc., independently.

The viscous damping coefficients are modeled with dependency only on the disk's vertical position such that

$$\begin{aligned}
\frac{\partial c_x}{\partial x} &= \frac{\partial c_x}{\partial y} = \frac{\partial c_x}{\partial \theta} = \frac{\partial c_x}{\partial \varphi} = 0 \\
\frac{\partial c_z}{\partial x} &= \frac{\partial c_z}{\partial y} = \frac{\partial c_z}{\partial \theta} = \frac{\partial c_z}{\partial \varphi} = 0 \\
\frac{\partial c_\theta}{\partial x} &= \frac{\partial c_\theta}{\partial y} = \frac{\partial c_\theta}{\partial \theta} = \frac{\partial c_\theta}{\partial \varphi} = 0
\end{aligned} \tag{D.7}$$

and

$$\begin{aligned}
\frac{\partial c_x}{\partial z} &= \mu\pi r_{\mathrm{d}}^2 \left(\frac{1}{\left(\frac{z_{\mathrm{sh}}}{2} - z\right)^2} - \frac{1}{\left(\frac{z_{\mathrm{sh}}}{2} + z\right)^2} \right) \\
\frac{\partial c_z}{\partial z} &= \frac{9\pi\mu r_{\mathrm{d}}^4}{2} \left(\frac{1}{\left(\frac{z_{\mathrm{sh}}}{2} - z\right)^4} - \frac{1}{\left(\frac{z_{\mathrm{sh}}}{2} + z\right)^4} \right) \\
\frac{\partial c_\theta}{\partial z} &= \frac{144\mu r_{\mathrm{d}}^6}{5\pi^3} \left(\frac{1}{\left(\frac{z_{\mathrm{sh}}}{2} - z\right)^4} - \frac{1}{\left(\frac{z_{\mathrm{sh}}}{2} + z\right)^4} \right).
\end{aligned} \tag{D.8}$$

Due to the symmetry of the system,

$$\begin{aligned}
\frac{\partial c_y}{\partial q_k} &= \frac{\partial c_x}{\partial q_k} \\
\frac{\partial c_\varphi}{\partial q_k} &= \frac{\partial c_\theta}{\partial q_k}.
\end{aligned} \tag{D.9}$$

The electrostatic forces are functions of the disk position as well as the electrode voltages. The partial derivatives of the top and bottom electrostatic forces with respect to q_k are given by

$$\begin{aligned}
\frac{\partial F_{\mathrm{t}_{ij}}}{\partial q_k} &= \left(\frac{\varepsilon}{2\left(z_0 - z_{ij}\right)^2} \frac{\partial A_{\mathcal{E}_{ij}}}{\partial q_k} + \frac{\varepsilon A_{\mathcal{E}_{ij}}}{\left(z_0 - z_{ij}\right)^3} \frac{\partial z_{ij}}{\partial q_k} \right) v_{\mathrm{t}_{ij}}^2 \\
\frac{\partial F_{\mathrm{b}_{ij}}}{\partial q_k} &= \left(\frac{\varepsilon}{2\left(z_0 + z_{ij}\right)^2} \frac{\partial A_{\mathcal{E}_{ij}}}{\partial q_k} - \frac{\varepsilon A_{\mathcal{E}_{ij}}}{\left(z_0 + z_{ij}\right)^3} \frac{\partial z_{ij}}{\partial q_k} \right) v_{\mathrm{b}_{ij}}^2,
\end{aligned} \tag{D.10}$$

respectively. Since the electrostatic forces from the top and bottom electrodes are exerted at a coincident point for any given $\{\mathcal{E}_{\mathrm{t}_{ij}}, \mathcal{E}_{\mathrm{b}_{ij}}\}$ pair, defining

$$\frac{\partial F_{\mathrm{n}_{ij}}}{\partial q_k} = \frac{\partial F_{\mathrm{t}_{ij}}}{\partial q_k} - \frac{\partial F_{\mathrm{b}_{ij}}}{\partial q_k} \tag{D.11}$$

simplifies the expressions in the computations that follow. The partial derivatives of the electrostatic forces with respect to the top and bottom electrode voltages, respectively, are

$$\begin{aligned}\frac{\partial F_{\mathrm{t}_{ij}}}{\partial v_{\mathrm{t}_{ij}}} &= \frac{\epsilon A_{\mathcal{E}_{ij}}}{(z_0 - z_{ij})^2} v_{\mathrm{t}_{ij}} \\ \frac{\partial F_{\mathrm{b}_{ij}}}{\partial v_{\mathrm{b}_{ij}}} &= \frac{\epsilon A_{\mathcal{E}_{ij}}}{(z_0 + z_{ij})^2} v_{\mathrm{t}_{ij}}.\end{aligned} \tag{D.12}$$

To write the gradient of each electrostatic force with respect to w_{tf}, define the vectors $e_{\mathrm{t}_{ij}}$ and $e_{\mathrm{b}_{ij}}$ to pick off the states in w_{tf} corresponding to the top and bottom electrode voltages, i.e.,

$$\begin{aligned}v_{\mathrm{t}_{ij}} &= e_{\mathrm{t}_{ij}}^T w_{\mathrm{tf}} \\ v_{\mathrm{b}_{ij}} &= e_{\mathrm{b}_{ij}}^T w_{\mathrm{tf}},\end{aligned} \tag{D.13}$$

so that

$$\frac{\partial F_{\mathrm{n}_{ij}}}{\partial w_{\mathrm{tf}}} = \frac{\partial F_{\mathrm{t}_{ij}}}{\partial v_{\mathrm{t}_{ij}}} e_{\mathrm{t}_{ij}}^T - \frac{\partial F_{\mathrm{b}_{ij}}}{\partial v_{\mathrm{b}_{ij}}} e_{\mathrm{b}_{ij}}^T. \tag{D.14}$$

The partial derivatives of the generalized forces and torques, normalized by the disk mass and transverse-axis moment of inertia, respectively, with respect to q are

$$\begin{aligned}\frac{\partial \ddot{x}}{\partial x} &= -\frac{k_x}{m} + \frac{\varphi}{m} \sum_{i,j} \frac{\partial F_{\mathrm{n}_{ij}}}{\partial x} \\ \frac{\partial \ddot{x}}{\partial y} &= \frac{\varphi}{m} \sum_{i,j} \frac{\partial F_{\mathrm{n}_{ij}}}{\partial y} \\ \frac{\partial \ddot{x}}{\partial z} &= -\frac{\dot{x}}{m} \frac{\partial c_x}{\partial z} + \frac{\varphi}{m} \sum_{i,j} \frac{\partial F_{\mathrm{n}_{ij}}}{\partial z} \\ \frac{\partial \ddot{x}}{\partial \theta} &= \frac{\varphi}{m} \sum_{i,j} \frac{\partial F_{\mathrm{n}_{ij}}}{\partial \theta} \\ \frac{\partial \ddot{x}}{\partial \varphi} &= \frac{1}{m} \sum_{i,j} \left(F_{\mathrm{n}_{ij}} + \varphi \frac{\partial F_{\mathrm{n}_{ij}}}{\partial \varphi} \right)\end{aligned} \tag{D.15}$$

$$
\begin{aligned}
\frac{\partial \ddot{y}}{\partial x} &= -\frac{\theta}{m}\sum_{i,j}\frac{\partial F_{\mathrm{n}_{ij}}}{\partial x} \\
\frac{\partial \ddot{y}}{\partial y} &= -\frac{k_y}{m} - \frac{\theta}{m}\sum_{i,j}\frac{\partial F_{\mathrm{n}_{ij}}}{\partial y} \\
\frac{\partial \ddot{y}}{\partial z} &= -\frac{\dot{y}}{m}\frac{\partial c_y}{\partial z} - \frac{\theta}{m}\sum_{i,j}\frac{\partial F_{\mathrm{n}_{ij}}}{\partial z} \\
\frac{\partial \ddot{y}}{\partial \theta} &= -\frac{1}{m}\sum_{i,j}\left(F_{\mathrm{n}_{ij}} + \theta\frac{\partial F_{\mathrm{n}_{ij}}}{\partial \theta}\right) \\
\frac{\partial \ddot{y}}{\partial \varphi} &= -\frac{\theta}{m}\sum_{i,j}\frac{\partial F_{\mathrm{n}_{ij}}}{\partial \varphi}
\end{aligned}
\tag{D.16}
$$

$$
\begin{aligned}
\frac{\partial \ddot{z}}{\partial x} &= \frac{1}{m}\sum_{i,j}\frac{\partial F_{\mathrm{n}_{ij}}}{\partial x} \\
\frac{\partial \ddot{z}}{\partial y} &= \frac{1}{m}\sum_{i,j}\frac{\partial F_{\mathrm{n}_{ij}}}{\partial y} \\
\frac{\partial \ddot{z}}{\partial z} &= -\frac{\dot{z}}{m}\frac{\partial c_z}{\partial z} + \frac{1}{m}\sum_{i,j}\frac{\partial F_{\mathrm{n}_{ij}}}{\partial z} \\
\frac{\partial \ddot{z}}{\partial \theta} &= \frac{1}{m}\sum_{i,j}\frac{\partial F_{\mathrm{n}_{ij}}}{\partial \theta} \\
\frac{\partial \ddot{z}}{\partial \varphi} &= \frac{1}{m}\sum_{i,j}\frac{\partial F_{\mathrm{n}_{ij}}}{\partial \varphi}
\end{aligned}
\tag{D.17}
$$

$$
\begin{aligned}
\frac{\partial \ddot{\theta}}{\partial x} &= \frac{1}{J_\mathrm{t}}\sum_{i,j}\left((\bar{y}_{ij} - y)\frac{\partial F_{\mathrm{n}_{ij}}}{\partial x} + F_{\mathrm{n}_{ij}}\frac{\partial \bar{y}_{ij}}{\partial x}\right) \\
\frac{\partial \ddot{\theta}}{\partial y} &= \frac{1}{J_\mathrm{t}}\sum_{i,j}\left((\bar{y}_{ij} - y)\frac{\partial F_{\mathrm{n}_{ij}}}{\partial y} + F_{\mathrm{n}_{ij}}\left(\frac{\partial \bar{y}_{ij}}{\partial y} - 1\right)\right) \\
\frac{\partial \ddot{\theta}}{\partial z} &= -\frac{\dot{\theta}}{J_\mathrm{t}}\frac{\partial c_\theta}{\partial z} + \frac{1}{J_\mathrm{t}}\sum_{i,j}\left((\bar{y}_{ij} - y)\frac{\partial F_{\mathrm{n}_{ij}}}{\partial z}\right) \\
\frac{\partial \ddot{\theta}}{\partial \theta} &= \frac{1}{J_\mathrm{t}}\sum_{i,j}\left((\bar{y}_{ij} - y)\frac{\partial F_{\mathrm{n}_{ij}}}{\partial \theta}\right) \\
\frac{\partial \ddot{\theta}}{\partial \varphi} &= \frac{2}{J_\mathrm{t}}\left(J_\mathrm{t} - J_\mathrm{s}\right)\dot{\theta}\dot{\varphi} + \frac{1}{J_\mathrm{t}}\sum_{i,j}\left((\bar{y}_{ij} - y)\frac{\partial F_{\mathrm{n}_{ij}}}{\partial \varphi}\right)
\end{aligned}
\tag{D.18}
$$

$$
\begin{aligned}
\frac{\partial \ddot{\varphi}}{\partial x} &= \frac{1}{J_\mathrm{t}} \sum_{i,j} \left((x - \bar{x}_{ij}) \frac{\partial F_{\mathrm{n}_{ij}}}{\partial x} + F_{\mathrm{n}_{ij}} \left(1 - \frac{\partial \bar{x}_{ij}}{\partial x} \right) \right) \\
\frac{\partial \ddot{\varphi}}{\partial y} &= \frac{1}{J_\mathrm{t}} \sum_{i,j} \left((x - \bar{x}_{ij}) \frac{\partial F_{\mathrm{n}_{ij}}}{\partial y} - F_{\mathrm{n}_{ij}} \frac{\partial \bar{x}_{ij}}{\partial y} \right) \\
\frac{\partial \ddot{\varphi}}{\partial z} &= -\frac{\dot{\varphi}}{J_\mathrm{t}} \frac{\partial c_\varphi}{\partial z} + \frac{1}{J_\mathrm{t}} \sum_{i,j} \left((x - \bar{x}_{ij}) \frac{\partial F_{\mathrm{n}_{ij}}}{\partial z} \right) \\
\frac{\partial \ddot{\varphi}}{\partial \theta} &= \frac{1}{J_\mathrm{t}} \sum_{i,j} \left((x - \bar{x}_{ij}) \frac{\partial F_{\mathrm{n}_{ij}}}{\partial \theta} \right) \\
\frac{\partial \ddot{\varphi}}{\partial \varphi} &= \frac{1}{J_\mathrm{t}} \left(J_\mathrm{s} - J_\mathrm{t} \right) \dot{\theta}^2 + \frac{1}{J_\mathrm{t}} \sum_{i,j} \left((x - \bar{x}_{ij}) \frac{\partial F_{\mathrm{n}_{ij}}}{\partial \varphi} \right).
\end{aligned}
\tag{D.19}
$$

Note that $k_x = k_y = 0$ for the larger, 41 mm radius disk. The gradient of the normalized forces and torques with respect to q is thus

$$
\nabla_q f = \begin{bmatrix}
\frac{\partial \ddot{x}}{\partial x} & \frac{\partial \ddot{x}}{\partial y} & \frac{\partial \ddot{x}}{\partial z} & \frac{\partial \ddot{x}}{\partial \theta} & \frac{\partial \ddot{x}}{\partial \varphi} \\
\frac{\partial \ddot{y}}{\partial x} & \frac{\partial \ddot{y}}{\partial y} & \frac{\partial \ddot{y}}{\partial z} & \frac{\partial \ddot{y}}{\partial \theta} & \frac{\partial \ddot{y}}{\partial \varphi} \\
\frac{\partial \ddot{z}}{\partial x} & \frac{\partial \ddot{z}}{\partial y} & \frac{\partial \ddot{z}}{\partial z} & \frac{\partial \ddot{z}}{\partial \theta} & \frac{\partial \ddot{z}}{\partial \varphi} \\
\frac{\partial \ddot{\theta}}{\partial x} & \frac{\partial \ddot{\theta}}{\partial y} & \frac{\partial \ddot{\theta}}{\partial z} & \frac{\partial \ddot{\theta}}{\partial \theta} & \frac{\partial \ddot{\theta}}{\partial \varphi} \\
\frac{\partial \ddot{\varphi}}{\partial x} & \frac{\partial \ddot{\varphi}}{\partial y} & \frac{\partial \ddot{\varphi}}{\partial z} & \frac{\partial \ddot{\varphi}}{\partial \theta} & \frac{\partial \ddot{\varphi}}{\partial \varphi}
\end{bmatrix}.
\tag{D.20}
$$

Similarly, the partial derivatives of the normalized generalized forces and torques with respect to w_tf are

$$
\begin{aligned}
\frac{\partial \ddot{x}}{\partial w_\mathrm{tf}} &= \frac{\varphi}{m} \sum_{i,j} \frac{\partial F_{\mathrm{n}_{ij}}}{\partial w_\mathrm{tf}} \\
\frac{\partial \ddot{y}}{\partial w_\mathrm{tf}} &= -\frac{\theta}{m} \sum_{i,j} \frac{\partial F_{\mathrm{n}_{ij}}}{\partial w_\mathrm{tf}} \\
\frac{\partial \ddot{z}}{\partial w_\mathrm{tf}} &= \frac{1}{m} \sum_{i,j} \frac{\partial F_{\mathrm{n}_{ij}}}{\partial w_\mathrm{tf}} \\
\frac{\partial \ddot{\theta}}{\partial w_\mathrm{tf}} &= \frac{1}{J_\mathrm{t}} \sum_{i,j} \left((\bar{y}_{ij} - y) \frac{\partial F_{\mathrm{n}_{ij}}}{\partial w_\mathrm{tf}} \right) \\
\frac{\partial \ddot{\varphi}}{\partial w_\mathrm{tf}} &= \frac{1}{J_\mathrm{t}} \sum_{i,j} \left((x - \bar{x}_{ij}) \frac{\partial F_{\mathrm{n}_{ij}}}{\partial w_\mathrm{tf}} \right),
\end{aligned}
\tag{D.21}
$$

and the corresponding gradient of f is

$$\nabla_{w_{\mathrm{tf}}} f = \begin{bmatrix} \frac{\partial \ddot{x}}{\partial w_{\mathrm{tf}}} \\ \frac{\partial \ddot{y}}{\partial w_{\mathrm{tf}}} \\ \frac{\partial \ddot{z}}{\partial w_{\mathrm{tf}}} \\ \frac{\partial \ddot{\theta}}{\partial w_{\mathrm{tf}}} \\ \frac{\partial \ddot{\varphi}}{\partial w_{\mathrm{tf}}} \end{bmatrix}. \tag{D.22}$$

The gradient of the normalized forces and torques with respect to $\dot{q}$ is given by

$$\nabla_{\dot{q}} f = - \begin{bmatrix} \frac{c_x}{m} & 0 & 0 & 0 & 0 \\ 0 & \frac{c_y}{m} & 0 & 0 & 0 \\ 0 & 0 & \frac{c_z}{m} & 0 & 0 \\ 0 & 0 & 0 & \frac{2\varphi(J_{\mathrm{s}}-J_{\mathrm{t}})\dot{\varphi}+c_\theta}{J_{\mathrm{t}}} & \frac{2\varphi(J_{\mathrm{s}}-J_{\mathrm{t}})\dot{\theta}}{J_{\mathrm{t}}} \\ 0 & 0 & 0 & \frac{2\varphi(J_{\mathrm{t}}-J_{\mathrm{s}})\dot{\theta}}{J_{\mathrm{t}}} & \frac{c_\varphi}{J_{\mathrm{t}}} \end{bmatrix}. \tag{D.23}$$

REFERENCES

[AB17] Khaled F Aljanaideh and Dennis S Bernstein. "Closed-loop identification of unstable systems using noncausal FIR models." *International Journal of Control*, **90**(2):168–185, 2017.

[AM18] Michael Andonian and Robert T. M'Closkey. "Sensing and control interface for precise gap control." *Mechatronics*, **56**:277–286, 2018.

[AM21] Michael Andonian and Robert T M'Closkey. "An electrostatically suspended contactless platform." *Mechatronics*, **80**:102685, 2021.

[Atk67] James L. Atkinson. "Electrostatic bearing.", 1967.

[Atk75] James L. Atkinson. "Electrostatic BEaring Sensing and Control Circuitry.", 1975.

[BY07] Minhang Bao and Heng Yang. "Squeeze film air damping in MEMS." *Sensors and Actuators A: Physical*, **136**(1):3–27, 2007.

[CWY14] Jae Yoong Cho, Jong-Kwan Woo, Jialiang Yan, Rebecca L Peterson, and Khalil Najafi. "Fused-Silica Micro Birdbath Resonator Gyroscope (μ-BRG)." *Journal of Microelectromechanical Systems*, **23**(1):66–77, 2014.

[DSC17] Ali Darvishian, Behrouz Shiari, Jae Yoong Cho, Tal Nagourney, and Khalil Najafi. "Anchor loss in hemispherical shell resonators." *Journal of Microelectromechanical Systems*, **26**(1):51–66, 2017.

[Enn84] Dale F Enns. "Model reduction with balanced realizations: an error bound and a frequency weighted generalization." In *The 23rd IEEE conference on decision and control*, pp. 127–132. IEEE, 1984.

[Fra87] Bruce A Francis. *A Course in $\mathcal{H}_\infty$ Control Theory*, volume 88. Springer-Verlag, 1987.

[Glo84] Keith Glover. "All optimal Hankel-norm approximations of linear multivariable systems and their $\mathcal{L}_\infty$-error bounds." *International journal of control*, **39**(6):1115–1193, 1984.

[GM89] Keith Glover and Duncan McFarlane. "Robust stabilization of normalized coprime factor plant descriptions with $\mathcal{H}_\infty$ bounded uncertainty." *IEEE Transactions on Automatic Control*, **34**(8):821–830, 1989.

[HGL05] Fengtian Han, Zhongyu Gao, Dongmei Li, and Yongliang Wang. "Nonlinear compensation of active electrostatic bearings supporting a spherical rotor." *Sensors and Actuators A: Physical*, **119**(1):177–186, 2005.

[Hig89] Nicholas J. Higham. "Matrix Nearness Problems and Applications." In M. J. C. Gover and S. Barnett, editors, *Applications of Matrix Theory*, pp. 1–27. Oxford University Press, 1989.

[HK66] BL Ho and Rudolf E Kalman. "Effective Construction of Linear State-Variable Models from Input/Output Functions." *Regelungstechnik*, **14**(12):545–548, 1966.

[HN82] Ekram Husain and RS Nema. "Analysis of Paschen Curves for Air, N_2 and SF_6 Using the Townsend Breakdown Equation." *IEEE Transactions on Electrical Insulation*, (4):350–353, 1982.

[HZP07] Mehran Hosseini, Guchuan Zhu, and Yves-Alain Peter. "A new formulation of fringing capacitance and its application to the control of parallel-plate electrostatic micro actuators." *Analog Integrated Circuits and Signal Processing*, **53**:119–128, 2007.

[JH98] Jong Up Jeon and Toshiro Higuchi. "Electrostatic suspension of dielectrics." *IEEE Transactions on industrial electronics*, **45**(6):938–946, 1998.

[JHK95] Ju Jin, Toshiro Higuchi, and Manabu Kanemoto. "Electrostatic Levitator for Hard Disk Media." *IEEE Transactions on Industrial Electronics*, **42**(5):467–473, 1995.

[JYH98] Ju Jin, Tachung C Yih, Toshiro Higuchi, and Jong Up Jeon. "Direct electrostatic levitation and propulsion of silicon wafer." *IEEE transactions on industry applications*, **34**(5):975–984, 1998.

[MEF03] Takao Murakoshi, Yasuo Endo, Keisuke Fukatsu, Sigeru Nakamura, and Masayoshi Esashi. "Electrostatically Levitated Ring-Shaped Rotational-Gyro/Accelerometer." *Japanese Journal of Applied Physics*, **42**(Part 1, No. 4B):2468–2472, 2003.

[MG90] Duncan C McFarlane and Keith Glover. *Robust Controller Design Using Normalized Coprime Factor Plant Descriptions*, volume 138, Lecture Notes in Control and Information Sciences. Springer-Verlag,Berlin, 1990.

[Pal37] Harlan B Palmer. "The Capacitance of a Parallel-Plate Capacitor by the Schwartz-Christoffel Transformation." *Electrical Engineering*, **56**(3):363–366, 1937.

[PKP98] Feixia Pan, Joel Kubby, Eric Peeters, Alex T Tran, and Subrata Mukherjee. "Squeeze film damping effect on the dynamic response of a MEMS torsion mirror." *Journal of Micromechanics and Microengineering*, **8**(3):200–208, 1998.

[SAA15] Doruk Senkal, Mohammed J Ahamed, Mohammad H Asadian Ardakani, Sina Askari, and Andrei M Shkel. "Demonstration of 1 million q-factor on microglass-blown wineglass resonators with out-of-plane electrostatic transduction." *Journal of Microelectromechanical Systems*, **24**(1):29–37, 2015.

[SBS86] GJ Sloggett, NG Barton, and SJ Spencer. "Fringing fields in disc capacitors." *Journal of Physics A: Mathematical and General*, **19**(14):2725–2736, 1986.

[SP05] Sigurd Skogestad and Ian Postlethwaite. *Multivariable Feedback Control: Analysis and Design*. John Wiley & Sons, 2 edition, 2005.

[TTM02] R. Toda, N. Takeda, T. Murakoshi, S. Nakamura, and M. Esashi. "Electrostatically levitated spherical 3-axis accelerometer." In *Technical Digest. MEMS 2002 IEEE International Conference. Fifteenth IEEE International Conference on Micro Electro Mechanical Systems (Cat. No.02CH37266)*, pp. 710–713, Jan 2002.

[Vid85] Mathukumalli Vidyasagar. *Control Systems Synthesis: A Factorization Approach*. MIT Press, 1985.

[Vid88] M Vidyasagar. "Normalised Coprime Factorizations for Nonstrictly Proper Systems." *IEEE transactions on Automatic Control*, **33**(3):300–301, 1988.

[Wil07] David C Wilcox. *Basic Fluid Mechanics*. DCW Industries, 3 edition, 2007.

[WLG21] Yusheng Wang, Yu-Wei Lin, Janna Glaze, Gabrielle Davis Vukasin, Dongsuk D Shin, Hyun-Keun Kwon, David B Heinz, Yunhan Chen, Dustin D Gerrard, Thomas W Kenny, et al. "Quantification of energy dissipation mechanisms in toroidal ring gyroscope." *Journal of Microelectromechanical Systems*, **30**(2):193–202, 2021.

[WYT10] Ewoud van West, Akio Yamamoto, and Higuchi Toshiro. "Manipulation of Thin Objects Using Levitation Techniques, Tilt Control, and Haptics." *IEEE Transactions on Automation Science and Engineering*, **7**(3):451–462, 2010.

[YBL74] DC Youla, JJ Bongiorno Jr, and CN Lu. "Single-Loop Feedback-Stabilization of Linear Multivariable Dynamical Plants." *Automatica*, **10**(2):159–173, 1974.

[ZDG96] Kemin Zhou, John Comstock Doyle, and Keith Glover. *Robust and Optimal Control*. Prentice Hall, 1996.